Departamento de Física de la Materia Condensada

Modelling spin correlations in graphene and chiral molecules

Tesis doctoral presentada por

Luis A. González Árraga

Directores:
Prof. Francisco Guinea López
Prof. Pablo San José

Tutor:
Prof. Guillermo Gómez Santos

Madrid, marzo de 2018

Agradecimientos

Quiero agradecer en primer lugar a mis directores Paco Guinea y Pablo San-José. A Paco por sentar el tono general de la tesis. A Pablo por la orientación que me dio a lo largo de todo este proceso, no lo hubiera podido lograr sin su ayuda, enumerar los detalles sería imposible en el limitado espacio de estos Agradecimientos.

Tengo que expresar mi gratitud también a Joaquín Fernández-Rossier, coordinador de la ITN-SPINOGRAPH, con la que fui finanaciado durante la mayor parte de la realización de esta tesis, por una serie de motivos: su hospitalidad durante mi estancia en su grupo en la Universidad de Alicante, y especialmente por haber sugerido el magnetismo en el *twisted bilayer graphene* como un problema interesante para investigar. El último capítulo de esta tesis es fruto de esa sugerencia. Joaquín además puso a mi disposición la ayuda de sus estudiantes, Jose Lado y Noel García, a quienes tengo que agradecer separadamente: Jose me dio una enorme ayuda técnica, con él aprendí los esencial de la teoría del modelo de Hubbard mean-field, y me señaló el método de Raffaele Resta para calcular la curvatura de Berry. A Noel le estaré eternamente agradecido por la paciencia con la que me enseñó lo fundamental sobre programación en Python, esencial para la mayor parte de esta tesis. Quiero agradecer también a antiguos miembros del grupo, Mohammed Sherafati y Bruno Amorim, por la ayuda que me dieron cuando estaba empezando.

A un nivel un poco más personal, quiero agradecer a los amigos que hice durante este periodo, Ángel Gutiérrez (el Brother), a Francesca Finocchiaro (conocida en los bajos fondos como la Franchi) y a Jose Silva (no tenemos un apodo para ti Jose!!), Luca Chirolli, Laura Fanfarillo, y a todos los chicos de SPINOGRAPH por los muchos momentos amenos en un medio que frecuentemente se volvía un tanto desquiciante. Tengo un recuerdo muy grato de la gente que conocí durante mi estancia en la Universidad de Alicante: Miguel, Bernat, María Jose, Taner.

Finalmente, a los viejos amigos: Michael, Evelyn, Fernando, Hans, a mi hermana Marisol, mi tía Marité; han hecho de mi vida en Madrid estos años una experiencia muy grata, me han hecho sentir como en casa.

Abstract

We first develop an analytical model to explain the spin-selectivity in experiments that measure conductance through DNA molecules attached to a Ni substrate and a gold electrode. Our model involves an electron confined to a helix potential; the spin-orbit due to the carbon atomic cores is modeled by a Rashba term. We calculate the eigenstates of the electron in the SO-active helix and by calculating the expectation value of the currents for eigenstates of different spins, we find that electrons of different spins propagate with different velocities, thus generating the spin-filtering seen in the experiments.

Moving on to graphene, we begin by studying superlattices of periodically hydrogenated graphene in a dilute regime. We include in our model the adatom-induced magnetism and spin-orbit couplings, and we investigate the topological properties of the band structure via a Berry curvature analysis. A direct visualization of the edge states is also carried out by calculating the spatial distribution of midgap states in the hydrogenated nanoribbon structure, and by looking at the DOS at the edge of semi-infinite structure. We also investigate the magnetic anisotropy induced by the spin-orbit coupling within a Hubbard model at the mean-field approximation.

Next, we consider pairwise interactions between adatoms in graphene. For distances in which their orbitals do not overlap, the adatoms may yet have indirect interactions mediated by the electrons of graphene. We calculate the total interaction energy via a two-impurity Anderson model. In unstrained graphene the interactions oscillate according to $\cos^2(\frac{\Delta \mathbf{K}}{2}.\mathbf{r})$ a type of periodicity that is referred to in the literature as Hidden Kekulé ordering. We investigate how elastic strains in graphene modulate the pair-wise interactions between adatoms. We include in our description the effects of adatom magnetization and consider also the interactions between adatoms in the hollow position and benzene-like adsorbates.

Lastly, the effect of electron-electron interactions in twisted bilayer graphene are investigated. The Fermi velocity is reduced for small twisting angles, leading to nearly flat bands (strongly localized in the regions of AA-stacking) around the Fermi level for some twisting angles. We calculate the magnetic

order within one unit cell using a collinear mean-field approximation for the Hubbard term and we obtain that the semimetal-Mott insulator transition is facilitated by the reduction of the Fermi velocity. Unlike the antiferromagnetic phase in the monolayer honeycomb, this antiferromagnetism is strongly localized in the AA regions. We also take into account the effect of an applied interlayer bias, which in the non-interacting limit enhances the electron-confinement. This enhanced confinement turns the moiré pattern of TBLG into a triangular superlattice of electrons confined in AA-regions, and we find that under interlayer bias the ground state becomes a 120° Néel state.

Resumen

Primero desarrollamos un modelo analítico para explicar la selectividad de espín observada en experimentos que miden la conductancia a través de moléculas de ADN adheridas a un sustrato de Ni y un electrodo de oro. Nuestro modelo es el de un electrón confinado en un potencial helicoidal; la interacción espín-órbita debida a los núcleos atómicos de carbono se modela como un término de Rashba. Calculamos los autoestados del electrón en la hélice con espn-rbita, y mediante un cálculo de los valores esperados de las corrientes para autoestados de diferentes orientaciones de espín, encontramos que los electrones de diferentes espines se progagan con diferentes velocidades, generando así el filtrado de espín observado en los experimentos.

Continuando en grafeno, empezamos estudiando superredes de grafeno hidrogenado de manera periódica en un régimen diluido. Incluimos en nuestro modelo el magnetismo y la interacción espín-órbita (EO) inducidas por el adátomo, e investigamos las propiedades topológicas mediante un análisis de la curvatura de Berry de las bandas del sistema. Se lleva a cabo una visualización directa de los estados de borde, calculando la distribución espacial de los estados dentro del gap de la estructura de nano-cintas hidrogenadas, y viendo la densidad de estados en el borde de una estructura semi-infinita. También investigamos la anisotropía magnética inducida por el acople EO mediante una aproximación de campo medio al modelo de Hubbard.

A continuación, consideramos las interacciones a pares entre adátomos en grafeno. Para distancias en las cuales sus orbitales no pueden solapar, los adátomos pueden tener interacciones indirectas mediadas por los electrones del grafeno. Calculamos la energía de interacción mediante un modelo de Anderson de dos impurezas. En grafeno sin tensiones elásticas, las interacciones oscilan de acuerdo a $\cos^2(\frac{\Delta \mathbf{K}}{2}.\mathbf{r})$, una periodicidad que da lugar a un ordenamiento conocido en la literatura como Orden de Kekulé oculto. Investigamos cómo las tensiones elásticas en el grafeno modulan la interacción entre pares de adátomos en grafeno. Incluimos en nuestra descripción, los efectos de la magnetización de los adátomos y consideramos también las interacciones entre adátomos adsorbidos en el centro del hexágono y adsorbatos con estructura de benzeno.

Por último, se investiga el efecto de las interacciones electrón-electrón en bicapas de grafeno rotado (TBLG, siglas en inglés). La velocidad de Fermi es reducida para pequeños ángulos de rotación, dando origen a bandas casi planas, fuertemente localizadas en las zona AA, cerca del nivel de Fermi para algunos ángulos de rotación. Calculamos el orden magnético dentro de una celda unidad usando una aproximación de campo medio colineal al modelo de Hubbard, y obtenemos que la transición de semimetal a aislante de Mott es facilitada por la reducción de la velocidad de Fermi. A diferencia de la fase antiferromagnética en la monocapa hexagonal, este antiferromagnetismo está fuertemente localizado en las zonas AA. También tomamos en cuenta el efecto de una diferencia de potencial entre las capas, que en el límite no-interactuante optimiza el confinamiento de electrones. Este confinamiento reforzado convierte al patrón de moiré del TBLG en una superred triangular de electrones confinados en las zonas AA, y encontramos que bajo la diferencia de potencial entre las capas el estado fundamental es un estado de Néel de 120°.

List of publications by author

1. Modulation of Kekulé adatom ordering due to strain in graphene. **L. A. González-Árraga**, F. Guinea and P. San-José. arXiv preprint arXiv:1711.07902 (2017) (accepted for publication in Physical Review B)

2. Electrically controllable magnetism in twisted bilayer graphene.**L. A. González-Árraga**, J.L. Lado, F. Guinea and P. San-José. Physical Review Letters 119 (10), 107201 (2017)

3. Topological features of engineered arrays of adsorbates in honeycomb lattices. **L. A. González-Árraga**, J.L. Lado and F. Guinea. Physica B: Condensed Matter 496, 1-8 (2016)

4. Continuum model for chiral induced spin selectivity in helical molecules. E. Medina,**L. A. González-Árraga**, D. Finkelstein-Shapiro, B.Berche and V. Mujica. Journal of Chemical Physics 142 (19), 194308 (2015)

Unrelated to this thesis

1. Spin polarization of entangled and mixed electron states in a beam splitter geometry coupled to an electron reservoir . **L. A. González-Árraga**, B. Berche and E. Medina. Physical Review B 86 (15), 155312 (2012)

2. Tunneling and transmission resonances of a Dirac particle by a double barrier. V.M. Villalba, **L. A. González-Árraga**. Physica Scripta 81 (2), 025010 (2010)

Contents

Introduction **1**

1 Continuum model for chiral-induced spin-selectivity in helical molecules **7**
1.1 Introduction 7
1.1.1 Yeganeh et al. [32]: Spin-selectivity in a scattering setup 15
1.2 Derivation of the Hamiltonian in the helix 17
1.3 Spin filtering and supressed backscattering 21
1.4 Charge and spin currents 23
1.5 Room temperature spin-selectivity 25
1.6 Summary and discussion 26

2 Topological features of engineered arrays of adsorbates in honeycomb lattices **29**
2.1 Introduction 29
2.1.1 Spin-orbit coupling in graphene 30
2.1.2 Models for Quantum Anomalous Hall effect in graphene 31
2.1.3 Magnetism due to single-H adatom and H-dimers in graphene 34
2.1.4 Magnetism due to periodic arrays of hydrogen-like adatoms 40
2.2 The Hamiltonian for superlattices of hydrogenated graphene . 43
2.3 Hydrogenated graphene: Local spin-orbit couplings 49
2.4 Honeycomb lattice with adsorbates and uniform SOC 51
2.5 Hydrogenated graphene away from half filling 53
2.6 Hubbard mean-field 54
2.7 Magnetic anisotropy. Angle-dependent mean-field 54
2.8 Summary and discussion 57

3 Modulation of Kekulé adatom ordering due to strain in graphene **59**
3.1 Gutierrez et al. experiment. Hidden Kekulé order in graphene 61

3.2 Adsorbate-adsorbate interactions in graphene 64
3.2.1 Single-impurity Anderson model 64
3.2.2 Two-impurity Anderson model 67
3.2.3 Top adatoms 70
3.3 Kekulé ordering in strained graphene 73
3.3.1 Strained graphene 73
3.4 Strong-coupling regime 77
3.5 Adatom magnetization 77
3.6 Asymptotic radial dependence 81
3.7 Hollow adatoms and benzene-like adsorbates 82

4 Electrically controllable magnetism in twisted bilayer graphene 85
4.1 Introduction 85
4.2 Tight-binding model for twisted graphene bilayers. Re-escaling 89
4.3 Mean-field Hubbard analysis 94
4.4 Non-collinear approach: Interaction between neighboring AA regions. 97
4.5 Summary and discussion 101

Concluding remarks 103

Conclusiones 105

A Hall conductivity and Berry curvature 107

B Intervalley scattering and Friedel oscillations in graphene 111

Bibliography 115

Introduction

A molecule (or any object for that matter) is chiral if it can be distinguished from its mirror image. For decades, spin-polarized electrons have been known to have the capability of distinguishing between left- and right-handed chiral molecules. In analogy with optical dichroism (the polarization-dependent absorption of light by molecules), this effect has been referred to in the literature as electron dichroism. An early experiment [1] found that electron scattering through a vapour of $Yb(hfc)_3$ (chiral molecules containing heavy atoms) was dependent on the spin of the incoming electron. The asymmetry factor in scattering was approximately 1.5×10^{-4}. More recently, experiments by Naaman and collaborators, generated spin-polarized free electrons by shining circularly polarized light on a gold substrate, and measured the scattering of these electrons through thin-films of chiral molecules attached to the gold [17]. In these experiments, they obtained asymmetries of up 10^{-1}, much larger than the ones measured in experiments in vapour phase, attributing the larger asymmetry (despite the chiral molecules having a low atomic number and weak spin-orbit coupling) to SOC-enhancing effects of the monolayer. Theoretical studies explain spin-selectivity in the scattering regime in terms of an interplay between the SOC of the molecule and its chiral geometry [32].

A more recent experiment observed the spin-selectivity effect in another setup where a chiral molecule (double strand DNA) is "sandwiched" between a nickel substrate and a gold nanoparticle [16]. In this experimental setup, the conductance is measured between two electrodes, hence the effect observed here involves bound electrons unlike in Ref. [17]. The conductance measurements were dependent on the spin-polarization of the electrons (which was controlled with a magnet below the nickel substrate). As a control, the authors substituted the DNA molecules with non-chiral molecules (dialkylthiols) sandwiched between the nickel and gold and no spin-selectivity in the conductance was observed. Given that the effect occurs within one molecule, this experiment shows that the cooperative effect of the self-assembled monolayer is not essential for the spin-selectivity to occur. In the first part of this thesis, we will propose a continuum theoret-

ical model to address the issue of spin-selectivity observed in conductance measurements through chiral molecules.

While electron dichroism in chiral molecules is a prominent example of spin-dependent dynamics in one-dimensional systems, this thesis devotes considerably more space to related spin-dependent effects in two-dimensional systems, which exhibit a far richer playing ground. In the second chapter we will consider spin-orbit effects in graphene. Graphene (first isolated in 2004 [2]) is a two-dimensional hexagonal lattice of carbon atoms forming sp^2 hybridized bonds. The hexagonal lattice has two triangular sublattices, the unit cell consisting of one atom of each sublattice. The conduction and valence bands of graphene touch at the vertices of the Brillouin zone, hence it is semimetal i.e. no gap between conduction and valence electrons but also no density of states at the Fermi level. Low-energy electrons can be described by a massless Dirac equation, though instead of c in the Dirac theory, they have a Fermi velocity $v_F \approx 10^6$ m/s, and the role of the spin in Dirac theory is here played by an internal degree of freedom, "pseudo-spin", which describes the distribution of the electrons in sublattices A and B. The study of graphene has been intertwined from the beginning with that of topological insulators (insulators in their interior that have conducting states in their edges), given that some of the earliest theoretical proposals for a Quantum Anomalous Hall and Quantum Spin Hall phase were based on graphene [63, 66] (even before its experimental fabrication).

Electron spin in graphene manifests most strongly in zigzag nanoribbon edges, atomic defects and adatoms. A hydrogen adatom on graphene, for example forms a covalent bond with a host carbon atom, locally changing the orbital hybridization from $sp^2 \rightarrow sp^3$, thus it is similar to a graphene vacancy in that it effectively removes the p_z orbital of the host carbon from the lattice. One of the most important consequences of H-adsorption in graphene is that, in the presence of electron-electron interactions, the sharp peak it generates in the DOS near the Fermi energy E_F, can easily become a spin-polarized quasi-bound state. Uchoa et al. [3] first studied this problem by applying Anderson's impurity model to a top-adatom in graphene, determining the conditions for the formation of a magnetic moment, predicting that its formation can be tuned via electric fields. The single sharp peak near E_F was first measured, for the case of a carbon vacancy, by Scanning Tunneling Spectroscopy in 2010 [5], but concrete evidence of spin-polarized double peak remained elusive until the publication of several experiments in 2016. González-Herrero et al. [91] measured a 20 meV spin-split peak in the LDOS of hydogenated graphene near the Fermi level via STM. This experiment, which yielded the first compelling evidence of H-induced magnetism in graphene will be extensively discussed in Chapter 2. A very similar ex-

periment by Zhang et al. [6] measured the spin-split peak in the DOS for the case of a carbon vacancy in graphene. Another experimental study by Nair et al. [111] confirmed that the magnetic moments induced by vacancies (created by irradiation) and sp^3 adsorbates in graphene can be switched on and off by electric manipulation of the Fermi level, thus opening the door for electrically controllable magnetism in graphene.

Besides inducing localized magnetic moments, another interesting effect of hydrogen adsorption in graphene is that the $sp^2 \rightarrow sp^3$ distortion locally enhances the spin-orbit interactions [61, 62], otherwise quite weak in pristine graphene. This SO-enhancing property of adatom adsorption inspired Qiao et al. [65] to propose superlattices of graphene with adsorbed Fe atoms (which adsorb in the hollow position at the center of a graphene hexagon), as a possible mechanism to engineer a Quantum Anomalous Hall effect in graphene. A similar idea was proposed by Weeks et al. [4], using Indium and Thalllium adatoms, in order to engineer a Quantum Spin Hall effect in graphene. Chapter 2 of this thesis explores the feasibility of achieving topologically non-trivial phases in engineered periodical superlattices of hydrogenated graphene.

Another interesting feature of adsorption in a substrate is that of interactions between adatoms. Two adsorbates attached to a substrate may interact directly if they are close enough that their atomic orbitals overlap, or via electrostatic interaction. For larger distances however, when their orbital-overlap becomes insignifican or in situations in which the electrostatic interaction is screened, interactions can arise due to the sharing of conduction electrons from the host; these interactions mediated by the scattering of conduction electrons of the substrate are called indirect interactions and they were first predicted in metals by Koutecky [7] and Grimley [8, 9]. The studies by Grimley found that the long-range interaction energy has an oscilatory behavior with the distance between the adatoms. The case of pair-wise interactions between adatoms in graphene has been a subject of intense investigation in recent years. The first study by Shytov et al. [140] shows that the sign of the interaction potential can change from attractive to repulsive, depending on whether the adatoms are in different (AB) or same sublattices (AA,BB), and found an oscillatory regime of the interaction that decays as $1/r$. A later, more complete study by Solenov et al. [144] combines density-functional theory, a tight-binding approach (a two-impurity Anderson model), and an analytical model, and they include electron-electron repulsions (neglected in ref. [140]) in their calculations. The authors found that there are two regimes of interaction: for short-ranges the electrostatic interaction between the adatoms predominates, the potential decays as $1/r$ and adatoms prefer to sit in AB configuration, whereas

for long-range, the indirect interaction mediated by π-electron scattering predominates, the potential decays as $1/r^3$ and the adatoms prefer AA configuration. They also studied how the interaction depends on the strength of the adsorbate-graphene coupling. Finally, LeBohec et al. [142] investigated how the interaction can be switched from repulsive to attractive via manipulation of the chemical potential.

Other studies have been centered on the RKKY interaction between magnetic impurities in graphene [148, 149], these studies all coincide in finding a $1/r^3$ long-distance decay for the RKKY interaction in graphene, and they show, for adatoms in top-positions, an oscillatory behavior with distance on atomic scales that is identical to the un-magnetized case (whereas hollow-adatoms show a similar long-range decay, but no oscillatory behavior). The coupling between spins in AA (AB)-configuration is ferromagnetic (antiferromagnetic). Building upon these previous works, Chapter 3 of this thesis will study how the indirect interactions between top-adatoms in graphene are modulated by the effect of elastic strains in graphene and how the above picture is affected by adsorption energy and dissipation effects.

Magnetism in 2D materials is of great technological interest, particularly for applications in data storage industries. However, they present challenges due to the fact that thermal fluctuations are far more relevant in 2D than in 3D systems. A theorem by Mermin and Wagner shows that long-range magnetic order is greatly hampered in 2D materials lacking magnetic anisotropy [167]. Until recently, zigzag edges, adatoms and vacancies were seen as the only practical approach to magnetism in two-dimensional cristals. Due to the fundamental appeal of 2D magnetism, and in particular of the possibility of controlling it electrically in two-dimensional crystals, such problems have become an active field of research. The discovery of the first truly intrinsic 2D ferromagnetic materials took place in 2017 in several related experiments. Firstly $Cr_2Ge_2Te_6$, with off-plane easy-axis, was found to be ferromagnetic up to its bilayer form [186]. In another experiment B. Huang *et al* [185] found that monolayer chromium triiodide CrI_3, a material with off-plane magnetic anisotropy, behaves like a ferromagnet with a relatively high Curie temperature of $T_C = 45$ K, this is the first material that has been proved to be ferromagnetic down to its monolayer form. More recently Huang et al. [10], studied the electric control of magnetism in bilayer CrI_3, which unlike the monolayer, is a layered antiferromagnet (that is, the magnetic moments in each monolayer are ferromagnetically coupled to one another, but opposite to those in the other monolayer). The application of an off-plane magnetic field can align the layers in the same direction, thus turning it into a ferromagnet for a critical value of magnetic field. The authors show that the application of an electric bias reduces the magnitude

of the critical magnetic field by up to 30 %. 2D-materials are also interesting from the point of view of frustrated magnetism. For instance geometric frustration of anti-ferromagnetism in triangular lattices can lead to quantum spin liquid phases [174, 175]. Single-side fluorinated graphene (C_2F), which shows a nearly-flat band at E_F for the non-interacting case, is predicted to have a 120° Néel ground state [11].

As was shown by Dos Santos et al. [157], a moiré pattern in the interlayer coupling of twisted bilayer graphene (TBLG) leads to a strong supression of the Fermi velocity. At low-angles this gives rise to nearly-flat bands at the Fermi level, that correspond to a localized electron state in the regions of AA-stacking. An electric bias between the two monolayers enhances the confinement of low-energy electrons in the AA-region [195]. The presence of a large DOS near the Fermi level, and the electrically tuneable confinement in a triangular superlattice of AA-stacking regions (which can lead to geometric frustration of antiferromagnetism), makes pristine TBLG, unlike the pristine monolayer, a very interesting material from the point of view of magnetism. In Chapter 4 of this thesis, we will examine the flat-band magnetism in TBLG, and we will investigate the effect of the electric bias (and geometric frustration) in its magnetic properties.

To summarize, the thesis is laid out as follows. In Chapter 1 we present an analytical model to explain spin-selectivity by chiral molecules in a tunneling regime. Moving on to graphene, Chapter 2 deals with a model for superlattices of dilutely hydrogenated graphene, in which we investigate the possible topologically non-trivial phases that may arise from the interplay of the lattice's spin-orbit coupling and the adatom-induced magnetization. We also investigate the magnetic anisotropy in this system. In Chapter 3, we consider the interactions between pairs of adatoms in graphene, and investigate how the influence of elastic strains modifies the interaction. We also address the interaction between magnetized adatoms, and the interaction between hollow-adatoms and benzene-like adsorbates. In Chapter 4 we study the effect of electron-electron interactions in twisted bilayer graphene in the small-angle limit. Finally, Appendix A gives detailed information about the method we used in Chapter 2 for the computation of the Berry curvature, and Appendix B explains the origin of the Friedel oscillations due to intervalley scattering caused by a top-impurity, the physical mechanism behind the Kekulé adatom-ordering discussed in Chapter 3.

Chapter 1

Continuum model for chiral-induced spin-selectivity in helical molecules

1.1 Introduction

The use of the word chirality has been attributed to Lord Kelvin [12] , who used it in order to describe the lack of parity symmetry in a material or molecule (that is: a mirror-symmetry operation transforms an enantiomer in another). Given that lots of bio-molecules are chiral and that a great amount of chemical reactions involve chiral molecules, a lot of effort has been invested in understanding enantio-selectivity in chemical transformations and in the study of the chemical properties of these structures [13, 14].

Within these studies, surprising experimental results have revealed a strong spin-selectivity in processes of electron scattering through self-assembled monolayers of chiral molecules (SAM's) [15–17, 42] and chiral oligopeptides [18], despite seeming unlikely under first intuitions [19]. The spin-selectivity or longitudinal spin-polarization is defined as:

$$S = \frac{I_+ - I_-}{I_+ + I_-} \tag{1.1}$$

where I_+ and I_- are the intensities corresponding to spins parallel and antiparallel to the electron velocity, respectively. The chiral-induced spin-selectivity effect opens the possibility of using chiral molecules in spintronic applications, where most devices are currently made of magnetic materials [20–22]. Understanding the origin of this effect would also help to get a deeper insight into spin-selective processes in biology [23–26].

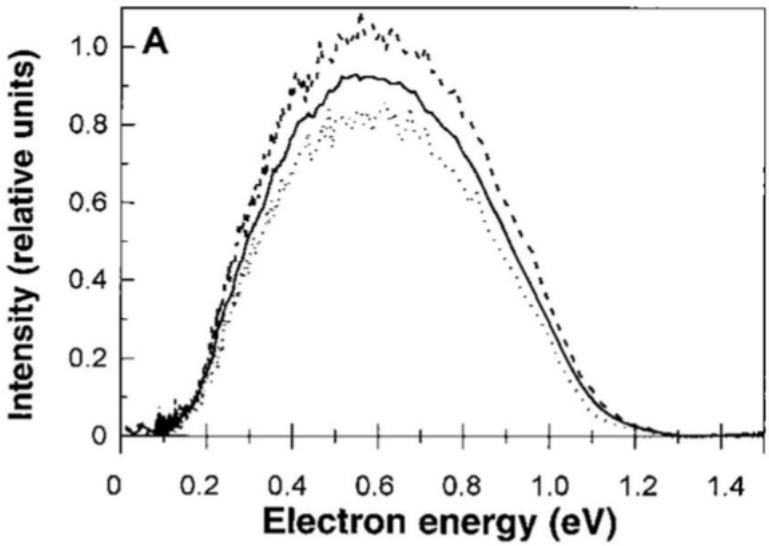

Figure 1.1: Distribution of electron energies for five films of L-Lysine. The photo-electrons were emitted with linearly polarized light (solid line), circularly ccw polarized light (discontinuous lines) and cw circularly polarized light (dotted line). Adapted with permission from [17]

The first experimental evidence of the existence of the chiral-induced spin-selectivity effect were obtained by Naaman et al. [17] in experiments of photo-emission of electrons scattered through Langmuir-Blodgett monolayers [27, 28] composed of films of left- (L) and right-handed (R) Lysine molecules deposited over a gold substrate. In the experiments, circularly polarized UV-light was used in order to emit photo-electrons from the gold substrate and the transmission was measured for different configurations. In their results they found that electron transmission depended on the polarization of the incoming light and the chirality of the molecules in the monolayer. For a specific polarization of the incoming light, they found that transmission of photoelectrons through a monolayer of L-Lysine was greater than through D-Lysine. Also, for monolayers of L-Lysine, transmission was more efficient when the light was circularly polarized counter-clockwise (ccw) than for linearly polarized light, and that this efficiency is even lower for light polarized clockwise (cw), as shown in Fig. (1.1), for positive polarization (spin oriented parallel to electron velocity). These results show a spin-selectivity with efficiency of up to 50 % , a result that is 103 times greater than the one reported in gas phase [29, 30]. Furthermore, they found that the preferred longitudinal spin-component changed sign under a change of the chirality of the molecule.

In more recent experiments by Gohler et al. [42] it has been convincingly proved that chiral molecule arrays act as efficient spin-filters for photoelectrons. They performed transmission experiments for electrons through SAM's of DNA molecules, oriented vertically over a gold substrate. The preparation of the SAM's was similar to the ones described in [27]. The photoelectrons were emitted using a laser pulse whose photons have enough energy to emit electrons from the substrate without ionizing the molecules. The energies of the photoectrons varied from 0 to 1.2 eV. By direct measurement of the spin of the emitted electrons, they found that no matter the polarization of the incoming light, the electrons were polarized with their spins antiparallel to their velocity. Panel a) in Fig. (1.2) shows that spin-polarization of the photolectrons emitted by the gold depended on the polarization of the incoming light, going from -22% for cw circularly polarized light, 0% for linearly polarized light, and 22 % for ccw circularly polarized light. When the DNA SAM was placed over the substrate, the preferred spin-polarization, however, did not change with the light polarization, going from -35 % to -22 % (panels b,c,d in Fig. 1.2).Therefore, the DNA molecules act as a spin-filter. Among their results, they find an increase of spin-polarization with the length of the molecule, reaching up to 60 % spin-polarization at room temperature for SAM's composed of DNA molecules of 78 pair bases, they reported an additional dependence on the organization of the molecules in the monolayer. These experiments involve energies within the range of tens of eV beyond Born's first approximation, through monolayers that can be up to 30 nm thick.

The chiral-induced spin-selectivity effect was also studied in the regime of tunnel effect energies [16], through conductance measurements of double strand DNA molecules, for polarized electrons, injected with their spins either parallel or antiparallel to the axis of the helix. In this study, the DNA molecules were deposited over a Nickel substrate and united in the other extreme to a gold nanoparticle, forming a Ni-DNA-Au structure. I-V curves were measured for different Ni magnetizations Fig. (1.3). The curves show a clear dependence of the conductance of the molecule with the direction of the applied magnetic field and the molecule‘s length. These curves are symmetric, that is, no matter if the applied voltage is positive or negative, the favored spin-component is always the negative one (spin antiparallel to electron velocity). When the electrons are expelled from Ni, they mostly majority spins. If their spin-orientation is consistent with the spin-orientation favored by the chiral molecule, then the current for this magnetic field direction will be greater than when Ni is magnetized in the opposite direction, since this spin-component would be unfavored by the DNA molecule for transmission. When the electrons are transmitted

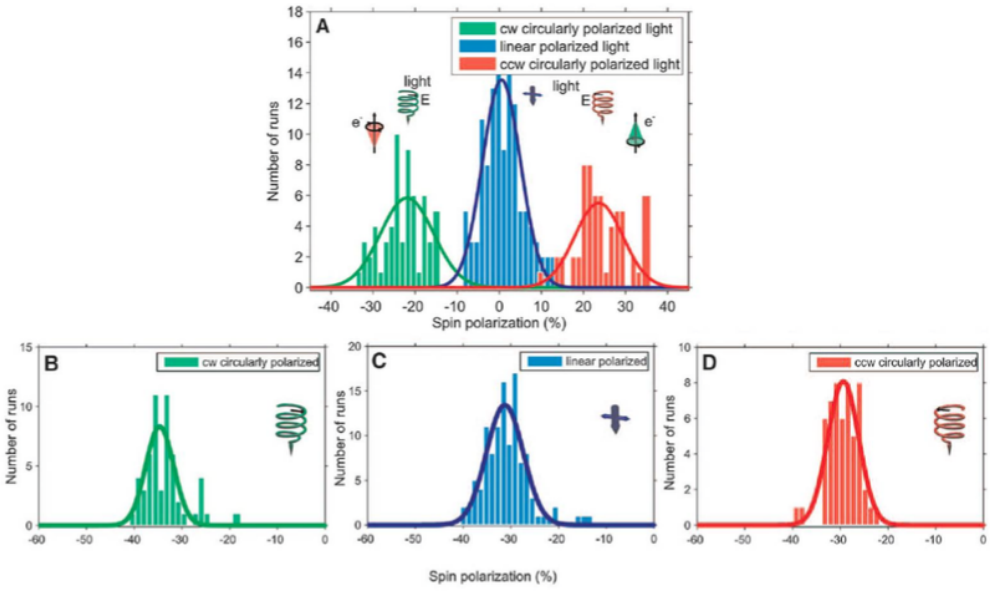

Figure 1.2: (a) Spin-polarization distribution for photo-electrons emitted from the gold substrate with cw circularly polarized light (green), ccw polarized light (red) and linearly-polarized light (blue) (b) Longitudinal spin-polarization distribution for electrons transmitted through a double-strand DNA monolayer over a gold substrate. In this case, the spin-polarization does not depend on the polarization of the incoming light, always being favored the negative spin-component (antiparallel to electron velocity). Adapted with permission from [42] .

in the opposite direction (from Au to Ni), the spin-direction favored by the molecule is opposite to the previous case. If the spin favored by the molecule coincides with the sub-band of electrons that are minority in Ni (which has a high density of states above the Fermi level), electron injection towards Ni is favored. Thus, the results are consistent with spin-selectivity through the DNA chain.

These results have been known for over a decade. However, the presence of light nuclei in these systems, such as C, H, O and N atoms, and the absence of sufficiently strong magnetic fields seem unable to explain the high spin-asymmetry that is observed, which suggests the development of a theoretical explanation that sheds light on the origin of the effect. Recent theoretical approaches, both analytic and numerical, have proposed models to capture the nature of this spin-selectivity with some success. All the models consist, at their core, of calculating the spin-orbit interaction of an electron that moves through a helix potential, considering explicitly a Rashba-type SO term. In this sense, two different regimes for electron transport have been considered:

(i) Single-scattering of free electrons [31,32]. Medina et al. [31] analyzed the process of multiple elastic scattering through a molecule composed of six C atoms, organized in a helix completing one full turn, acting as a scattering center for electrons. From this analysis, three main results emerged: (a) despite the fact that transverse polarization can originate under inelastic effects, a longitudinal polarization requires the existence of chirality (b) the SO interaction is enhanced by the fact that the density of the molecules in the SAM's is comparable to a solid structure, thus increasing the overlap of orbital wave functions (c) multiple scattering is necessary for producing a longitudinal polarization, in such a way there is an energy range . They also show that there is a linear increment of the polarization with the number of turns of the helix, the slope depending on the chirality of the molecule.

(ii) The movement of electrons bound among the atomic orbitals [33–35, 46]. Gutierrez et al [33] constructed a simplified model involving point charges along a helix path. Within a tight-binding model for the electronic structure, they determined the transmission coefficients for different electron spin states. Via the estimation of the effects of atomic proximity and the SO coupling patameter, they defined a reasonable range of parameters that result in substantial spin-polarizations. Their results show that a large SO coupling enhances spin polarization. However it is strongly diminished if electronic coupling is strong, a result they explain is due to the fact that the time in which the electron and the chiral structure interact is diminished with the increase in overlaps. In this same regime, Guo and Sung [46] propose a tight-binding model to emulate a double-strand DNA helix, and

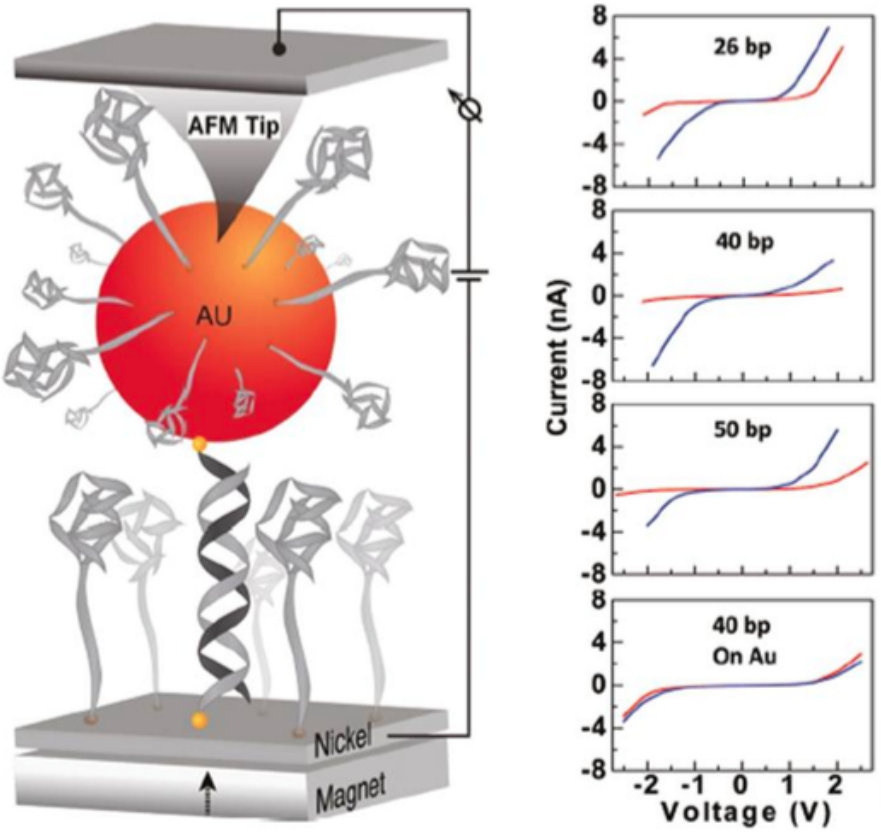

Figure 1.3: Experimental setup for the conductance measurement of a Au-DNA-Ni system. The graphs show the current vs applied voltage, when the magnetic field is in the up (red) or down (blue) direction. The curves are symmetric, that is, no matter what the applied voltage is, the spin component that is transmitted most efficiently is always the same (in this case the one antiparallel to electron velocity. Adapted with permission from [16])

calculate the conductance through a metal-DNA-metal structure. They conclude that both the SO coupling and the chirality of the molecular structure are required to obtain spin-polarization. Furthermore they found an optimal length of the chain for which spin-polarization is maximized.

Despite the differences between all these studies, the physical phenomenology that they show is similar. In both regimes, the models so far predict a spin-polarization of the electrons, as long as SO interactions are considered (intrinsic or due to external electric fields). The magnitude of SO coupling is critical to explain spin-selectivity. It has been shown that strong electric fields can be produced, for example, by charge transfer [19]. The magnitude of these fields is greater than any other external molecular field, but it would produce an SO interaction much smaller than necessary to explain the experimental data. However the experiments reveal that the magnitude of the interaction is related to the chiral structure of the molecule, given that lack of chirality cancels any spin-selectivity in low-atomic weight systems. All the above-mentioned theoretical proposals fixed the magnitude of the SO interaction to adapt to the experimental results. They estimate the value of the SO coupling of the chiral molecule to be 1 or 2 orders of magnitude above the atomic SO coupling. Although these values have been reported for carbon nanotubes [36,37] , no measures are known for DNA or polipeptides.

There are two crucial approaches when fixing the magnitudes of the electric fields in order to adjust properly the values of the SO interaction. The first approach [31,32] is that the scattering of free electrons and/or their transport bound to the helix derives the magnitude of the SO molecular interaction from the intrinsic atomic SO or the external p orbitals of the carbon atoms. The second approach [33,46] derives the values of the electric field from the electrostatic potential . Considering the second approach, for electrons with $v = 0.2\ c$, moving through an electric field of $4.5 \times 10^1 1$ V/m , the effective magnetic field in the reference frame of the electron would be 3T. This field value is the same order as the field of an electron in the ground state of hydrogen. These fields are usually strong when the molecular structures formed by heavy atoms are considered. However in organic structures formed mainly by light atoms, in order to observe the effect of high measured polarization, one needs fields that are 10-100 times greater.

We aim here to theoretically describe the single molecule experiments in more detail: For electrons with energies below the molecular barrier, a current is driven by a potential difference, through single DNA molecules in an STM set up [16]. The experimental results consist of a spin dependent barrier to tunnelling of electrons through the chiral molecule. A preferred

spin direction results in a larger current than the opposite spin direction. There is a gap between barrier heights that is independent of the molecule length and is thus proportional to the SO coupling. A striking characteristic of the I-V curve is that it is anti-symmetric ($V \to -V$), and the preferred spin filtering direction in one bias direction is opposite to the preferred spin of the other [16]. Finally, the bias needed to produce the same spin polarised current increases with molecule length.

Here we present a model for the tunnelling of electrons through a chiral molecule which can be solved exactly explaining many experimental features. The model includes the intrinsic SOC whose source are the atomic cores of the carbon atoms sitting on the bases of the DNA structure (with a definite orientation in space). The strength of such a coupling for tunnelling electrons can be readily derived from a tight binding approach, and involves both the intrinsic atomic value and contributions from the coupling between nearest neighbour bases sites of the DNA molecule. We can anticipate the results for this model by performing a symmetry analysis: Both the SO coupling and the helix break inversion symmetry, but time reversal symmetry is preserved. This implies that the spectrum of the spin-orbit active helix should be composed of Kramers degenerate doublets, separated by the effective spin-orbit coupling gap. The quantum numbers of the helix of definite chirality comprise the kinetic energy index, the rotation sense of the electron and its spin. Each Kramers doublet preserves time reversal symmetry, so that they comprise both rotation and both spin quantum numbers. On choosing a bias direction, only the channel (one of the two states in the doublet) for that sense of propagation is selected and has an associated spin. Thus, the bias breaks time reversal symmetry by only populating one channel and spin selectivity results.

This chapter is organised as follows: in the following subsection, we will explain in detail a previous theoretical description of chiral-induced spin-selectivity (by Yeganeh et al. [32]) in scattering experiments. Moving on to the tunneling regime that concerns us here, in section 1.2 we proceed to derive the Hamiltonian for an electron in a continuous one dimensional helix of a fixed number of turns and chirality, in the presence of spin-orbit coupling, whose source is a local atomic core electric field in the z direction. Electrons are constrained to follow the helical path on the corresponding eigenchannels. Two energies are defined; that of the free electron problem and the SO energy whose ratio determines the adiabaticity of spin transport [48]. Following, we obtain the channel energies and the corresponding exact eigenfunctions as a function of two quantum numbers (current direction and spin) and a chirality index. We then show that the spectrum implies that there are always two doubly degenerate levels and each degenerate pair combines

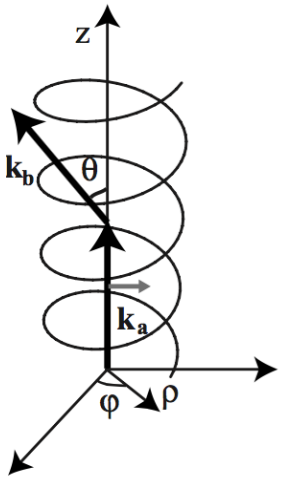

Figure 1.4: The proposed scattering geometry is diagrammed. The photoemitted electron is produced upon absorption of circularly polarized light traveling parallel to the long axis z of the helix with its spin quantized along the same direction. Adapted with permission from [32]

time reversed states. Whenever one biased direction is chosen, time reversal is broken and a preferred spin is filtered for that direction. The opposite spin state in the same direction is at a higher energy so that it requires a higher bias to be occupied, a feature that suppresses backscattering. The resulting spin selected transport is evidenced through the computation of the spin current along the helix, leading to spin accumulation observed in the experiments. We end with the conclusions.

1.1.1 Yeganeh et al. [32]: Spin-selectivity in a scattering setup

In this section we will discuss a model for spin-selectivity in a scattering setup developed by Yeganeh et al. [32]. In this setup, molecules with point or axial chirality (modeled as helices) are adsorbed on a gold substrate. The gold substrate is irradiated with circularly polarized light, thus producing spin-polarized electrons via photoelectric effect. The spin-polarized electrons are then scattered by the chiral molecules, and are assymptotically free. The repulsive scattering potential of the helical molecule is modelled as:

$$V(\mathbf{r}) = V_0\delta^3(\mathbf{r} - a(\hat{x}\cos\varphi + \mathbf{y}\sin\varphi) \pm \hat{z}b\varphi) = \frac{V_0}{2\pi\rho}\delta(\rho - a)\delta(z \pm b\varphi) \quad (1.2)$$

Additionally, the scattering potential contains a spin-orbit coupling term, so that the full scattering potential is:

$$V(\mathbf{r},\sigma) = V(\mathbf{r}) + H_{SO}(\mathbf{r},\sigma) = V(\mathbf{r}) - \alpha\sigma.(\nabla V(\mathbf{r}) \times \mathbf{p}) \tag{1.3}$$

where α is the effective strength of the SO interaction, and $\mathbf{p} = -i\hbar\nabla$ is the momentum operator. The incoming electron wave function is given by:

$$\Phi_a = e^{i\mathbf{k}_a.\mathbf{r}}\chi_{m_s} \tag{1.4}$$

where χ_{m_s} is the spinor wave-function with $m_s = \pm 1/2$. The spin-quantization axis is along the $\hat{z}$ direction. The scattered wave-function at an asymptotic distance is written:

$$\Psi = \Phi_a + F_{m_s}\frac{e^{ik_b r}}{r} \tag{1.5}$$

where F_{m_s} is the amplitude of the scattered wave-function, and the differential scattering cross section is $\frac{d\sigma}{d\Omega} = |F_{m_s}|^2$. F_{m_s} is calculated within the first Born approximation:

$$F_{m_s} = -\frac{\mu}{2\pi\hbar^2}\int e^{-i\mathbf{k_b}.\mathbf{r}'}V(\mathbf{r}',\sigma)e^{i\mathbf{k_a}.\mathbf{r}'}d^3\mathbf{r}'\chi_{m_s} = -\frac{\mu}{2\pi\hbar^2}(A+B)\chi_{m_s} \tag{1.6}$$

where the integrals A and B correspond to the electrostatic potential and the spin-orbit interaction respectively:

$$A = \int e^{-i\mathbf{k_b}.\mathbf{r}'}V(\mathbf{r}')e^{i\mathbf{k_a}.\mathbf{r}'}d^3\mathbf{r}' \tag{1.7}$$

$$B = \alpha\int e^{-i\mathbf{k_b}.\mathbf{r}'}\left[\nabla V(\mathbf{r}')\times\mathbf{p}\right]e^{i\mathbf{k_a}.\mathbf{r}'}d^3\mathbf{r}' \tag{1.8}$$

the direction of propagation of the incoming wave-function is the $\hat{z}$ so that $\mathbf{k_a} = k\hat{z}$. The analytical expressions of the integrals are unilluminating, hence, we omit them here, but can be found in Ref. [32]. The scattered amplitude, in terms of the integrals, can be rewritten as:

$$F_{m_s} = -\frac{\mu}{2\pi\hbar^2}(A\mathbb{1} + \sigma.(B_x\hat{x} + B_y\hat{y}))\chi_{m_s} \tag{1.9}$$

where B_x and B_y are the terms proportional to $\hat{x}$ and $\hat{y}$, see Ref. [32]. Using this, the differential cross sections can be written:

$$\frac{d\sigma}{d\Omega_\uparrow} = \left(\frac{\mu}{2\pi\hbar^2}\right)^2(|A|^2 + |B_x + iB_y|^2) \tag{1.10}$$

$$\frac{d\sigma}{d\Omega_\downarrow} = \left(\frac{\mu}{2\pi\hbar^2}\right)^2(|A|^2 + |B_x - iB_y|^2) \tag{1.11}$$

$$\frac{d\sigma}{d\Omega}_{unpolarized} = \left(\frac{\mu}{2\pi\hbar^2}\right)^2 (2|A|^2 + |B_x + iB_y|^2 + |B_x - iB_y|^2)/2 \quad (1.12)$$

The spin-polarization factor is defined as:

$$P = \frac{\frac{d\sigma}{d\Omega\uparrow} - \frac{d\sigma}{d\Omega\downarrow}}{\frac{d\sigma}{d\Omega}_{unpolarized}} = \frac{|B_x + iB_y|^2 - |B_x - iB_y|^2}{(2|A|^2 + |B_x + iB_y|^2 + |B_x - iB_y|^2)/2} \quad (1.13)$$

At this point, we should consider the limit $b \to 0$, in this limit the helix becomes a circular ring and chirality is lost. It can be easily checked that in this case, though $F_\uparrow$ and $F_\downarrow$ are still different, their modulus squared would be identical, thus yielding $P = 0$. It is the pitch magnitude and sign that yield different differential cross sections. This shows that spin-orbit interaction, is a necessary condition for spin-flipping in this context, but not sufficient. Fig. (1.5) shows the effect of altering helix pitch on P and confirms the importance of helicity for the chiral effect. As the pitch b of the helix becomes small compared to the radius a, the potential becomes a circular ring, and the chiral effect disappears as expected. At very large values of b the potential becomes a straight line, and the effect disappears as well.

1.2 Derivation of the Hamiltonian in the helix

After reviewing the model for spin-selective scattering from ref. [32] we now consider the case of spin-selectivity for conductance experiments, that is for bound electrons that propagate through the molecule.The model Hamiltonian we propose consists of an electron confined on a helix of N turns of radius a and pitch b as seen in Fig. (1.4). An internal electric field, of atomic origin, is assumed to exist as the source of the electron spin-orbit coupling. In an atomic model for the helix, the SO interaction offers a p_z to $p_{x,y}$ hopping route, first order in the atomic intrinsic SO coupling and thus, at least in the meV energy range. Assuming a motion strictly on the helix through a sequence of nearest neighbour states, we have the following Hamiltonian (see also ref. [49])

$$H = H_{kin} + H_{SO} = \frac{1}{2m*}(p_x^2 + p_y^2 + p_z^2) + (\alpha/\hbar)(p_x\sigma_y - p_y\sigma_x) \quad (1.14)$$

where the first term is pure kinetic energy, while the second term is the SO coupling for an intrinsic electric field in the z direction. The strength of the electric field is embedded in the parameter $\alpha = e\hbar^2 E/(4m^2c^2)$ which has dimensions of energy times a length. Nevertheless, this electric field is a nontrivial quantity to assess, since it not only contains a measure of the field felt by the electrons in their excursion to their nuclei, but also a quasi-resonant coupling contribution to the neighbouring states [50, 51]. We will

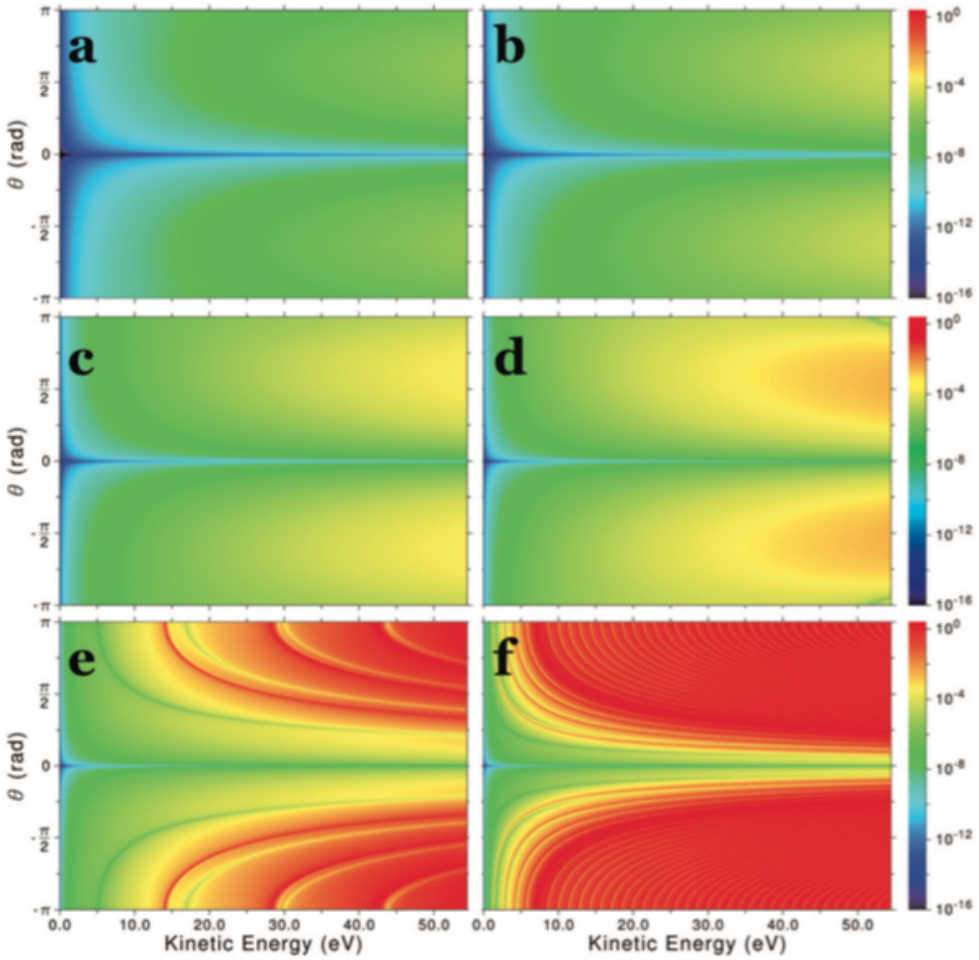

Figure 1.5: P is plotted for a number of different values for the helix pitch b. In all plots, $V_0 = 1$ eV, $a = 1$ A, and $K = 5.1$. The spin-quantization axis is along the helix axis, and the effective SO coupling is taken to be $\alpha = -2\times10^4\hbar/(2m_ec)^2$. Panels (a-f) show the polarization factor for $b = 10^-5$ A to $b = 10^0$ A in incremental order. As the b/a ratio increases, the potential changes from a ring to a helix, and the magnitud of the asymmetry factor increases. Adapted with permission from [32]

discuss these contributions later. Due to the symmetry of the problem it is preferable to work in cylindrical coordinates, eq. (1.14) becomes:

$$H = \frac{p_\varphi^2}{2m^*(a^2+b^2)} - \frac{\alpha a}{\hbar(a^2+b^2)}\sigma_\rho p_\varphi \tag{1.15}$$

However the SO Hamiltonian in eq. (1.15) does not satisfy the hermitian condition $\langle F|H_{S0}|G\rangle = \langle G|H_{S0}|F\rangle^*$, where $|F\rangle = F_\uparrow(\varphi)|\uparrow\rangle + F_\downarrow(\varphi)|\downarrow\rangle$ (and similarly for $|G\rangle$). Indeed, one finds that:

$$\langle F|\sigma_\rho p_\varphi|G\rangle^* = \langle G|\sigma_\rho p_\varphi|F\rangle - \langle F|i\sigma_\varphi|G\rangle \tag{1.16}$$

We can construct an hermitian SO Hamiltonian

$$W = -\frac{\alpha a}{\hbar(a^2+b^2)}\sigma_\rho p_\varphi + \frac{iA\alpha a}{(a^2+b^2)}\sigma_\varphi \tag{1.17}$$

and we check that W satisfies the hermitian condition If we set the constant $A = A^* = 1/2$, finally, after taking care of all the issues with hermiticity [52, 53], the helix Hamiltonian is written:

$$H = \frac{p_\varphi^2}{2m^*(a^2+b^2)} - \frac{\alpha a}{\hbar(a^2+b^2)}\sigma_\rho p_\varphi + \frac{i\alpha a}{2(a^2+b^2)}\sigma_\varphi \tag{1.18}$$

where $p_\varphi = m^*(a^2+b^2)\partial_t\varphi = -i\hbar\partial_\varphi$, a is the helix radius, b is the helix pitch, and $\sigma_\rho = \sigma_x\cos\varphi + \sigma_y\sin\varphi$ and $\sigma_\varphi = -\sigma_x\sin\varphi + \sigma_y\cos\varphi$. The helix curvature is given by the ratio $\kappa = \frac{a}{a^2+b^2}$ and the torsion is $\tau = \frac{b}{a^2+b^2}$. The momentum in the z direction will then be $p_z = \tau p_\varphi m*$ is the electron effective mass, which assumes the carbon states form a narrow band of states. It is physically convenient to identify two distinct frequencies $\omega_0 = \hbar/m(a^2+b^2)$ related to the free electron kinetic energy and $\omega_{SO} = 2\alpha a/\hbar(a^2+b^2)$ proportional to the helix curvature and the SO coupling. One can then simplify the the Hamiltonian in Eq. (1.18) into the simple quadratic form:

$$H = \frac{\hbar\omega_0}{2}\left(i\partial_\varphi + \frac{\omega_{S0}}{2\omega_0}\sigma_\rho\right)^2 \tag{1.19}$$

The ansatz for the wave function for spinfull electrons is on a helix of N turns with hard wall boundary conditions at the helix ends

$$\Psi_{n,s}^{\lambda,\zeta} = e^{i\lambda(n/2N)\varphi}\begin{pmatrix} A_s^{\lambda,\zeta}e^{-i\varphi/2} \\ B_s^{\lambda,\zeta}e^{i\varphi/2}\end{pmatrix} \tag{1.20}$$

where $\lambda = +1(-1)$ labels for the counter clockwise, (clockwise) electrons, $s = \pm 1$ labels the spin and $\zeta = \pm 1$ labels the chirality of the helix. Although the chiral index does not appear in the Hamiltonian, it chooses the

z direction of propagation for a particular λ index. Using the wave function ansatz one can derive the exact energy of the model as

$$E_{n,s}^{\lambda,\zeta} = \frac{\hbar\omega_0}{2}\left[\frac{n}{2N} - \frac{\zeta\lambda s}{2}\sqrt{1+(\frac{\omega_{SO}}{\omega_0})^2}\right]^2 \tag{1.21}$$

where n is a positive integer valued index. The basis functions chosen in Eq. (1.20) are convenient when addressing biased conditions for the system. Note that left and right propagating electrons with the same s-index are not degenerate, but time reversal symmetry is satisfied i.e. $E_{n,s}^{\lambda,\zeta} = E_{n,-s}^{-\lambda,\zeta}$ (simultaneous change of λ and s). This symmetry reflects the fact that the SO interaction is not symmetric under space inversion but preserves time reversal symmetry (simultaneous change of λ and s) so we retain Kramers degeneracy. The chirality label ζ also reflects inversion asymmetry as changes in the chiral sign, at fixed λ and s, change the energy.

When the spin-orbit interaction is absent ($\alpha = 0$), space and spin inversion symmetries are recovered (four fold degeneracy) once one combines $\tilde{n} = n/2N$ and $\tilde{n}+1$ labelled eigenvalues

Figure (1.6) shows a sequence of levels starting from the ground state (Kramers doublets) at two successive values of n along with their degenerate, at $\alpha = 0$ partners with index +1, as a function of the SO strength. The ordering of the levels are indicated according to the spin orientation and sense of the current of the chirality $\zeta = +1$.

To obtain a physical intuition on the nature of the wave functions [48,53], we derive explicitly some of the coefficients in the ansatz put forward. We explicitly do the $\lambda = +$, $\zeta = +$ case. Using equations (1.19) and (1.20) we find from the secular equation

$$B_{+,s}^{+} = \frac{\omega_0}{\omega_{S0}}\left(\frac{s}{\cos\theta} - 1\right)A_{+,s}^{+} \tag{1.22}$$

where $\cos\theta = 1/\sqrt{(1+(\omega_{SO}/\omega_0)^2)}$. In order to conform to a normalised spinor we choose $A_{+,+}^{+} = \cos(\theta/2)$, and thus $B_{+,+}^{+} = \sin(\theta/2)$, so we have

$$\tan\theta = \frac{\omega_{SO}}{\omega_0} \tag{1.23}$$

This angle results from the existence of a SO magnetic field $\mathbf{B_{SO}} = -\alpha(\mathbf{k}\times\hat{z})(2c/e) = (2c\alpha/a\hbar e)\lambda|\mathbf{L}|\hat{\rho}$, where $|\mathbf{L}|$ is the angular momentum of the electron on the helix, and λ gives the direction of the effective field depending on the rotation sense of the electron. The choice for the second eigenfunction is $A_{+,-}^{+} = -\sin(\theta/2)$, leading to the two eigenspinors

$$\Psi_{n,+}^{+,+} = e^{i\tilde{n}\varphi}\begin{pmatrix}\cos(\theta/2)e^{-i\varphi/2}\\ \sin(\theta/2)e^{i\varphi/2}\end{pmatrix} \tag{1.24}$$

$$\Psi^{+,+}_{n,-} = e^{i\tilde{n}\varphi}\begin{pmatrix} -\sin(\theta/2)e^{-i\varphi/2} \\ \cos(\theta/2)e^{i\varphi/2} \end{pmatrix} \tag{1.25}$$

The corresponding eigenfunctions for $\lambda = -1$ are

$$\Psi^{-,+}_{n,+} = e^{-i\tilde{n}\varphi}\begin{pmatrix} \cos(\theta/2)e^{-i\varphi/2} \\ \sin(\theta/2)e^{i\varphi/2} \end{pmatrix} \tag{1.26}$$

$$\Psi^{-,+}_{n,-} = e^{-i\tilde{n}\varphi}\begin{pmatrix} -\sin(\theta/2)e^{-i\varphi/2} \\ \cos(\theta/2)e^{i\varphi/2} \end{pmatrix} \tag{1.27}$$

The angle θ here tells about the inclination of the spinor with respect to the vertical z axis (see Fig. 1.6) and $\tilde{n} = n/2N$ with n an integer. When the SO coupling is very strong, $\theta \to \pi/2$, and the spin is in the plane, while for very small SO coupling, the spin is aligned with the z axis.

1.3 Spin filtering and supressed backscattering

The rotation and spin eigenvalue corresponding to the wave functions is depicted in Fig. (1.7) for both chiral labels. We have also evaluated the energies corresponding to the split doublets separated by the gap Δ. For fixed chirality, say $\zeta = +1$, there is a doubly degenerate (changing s and λ simultaneously) low energy configuration and a high energy configuration for each n:

$$E_{>} = \frac{\hbar\omega_0}{2}\left[\tilde{n} + \frac{1}{2}\sqrt{1 + \left(\frac{\omega_{SO}}{\omega_0}\right)^2}\right]^2 \tag{1.28}$$

$$E_{<} = \frac{\hbar\omega_0}{2}\left[\tilde{n} + 1 - \frac{1}{2}\sqrt{1 + \left(\frac{\omega_{SO}}{\omega_0}\right)^2}\right]^2 \tag{1.29}$$

As shown in Fig. (1.7), electrons propagating in the positive z direction will have a lower energy if their spin is $s = +1$. The same energy corresponds to their Kramers partner which propagates in the opposite direction. In order to propagate a $s = -1$ state in the positive direction, we need to pay an energy price Δ:

$$\Delta = \left(\tilde{n} + \frac{1}{2}\right)\frac{E^2_{SO}}{2\hbar\omega_0} \tag{1.30}$$

for $\omega_{SO}/\omega_0 < 1$ and $E_{SO} = \hbar\omega_{SO}$. On the other hand, if the energy $\hbar\omega_0 < \hbar\omega_{SO}$ due to poor mobility of the electron on the helix (small ω_0 due to large effective mass) then the energy gap is directly related to the SO energy

$$\Delta = \left(\tilde{n} + \frac{1}{2}\right)E_{SO} \tag{1.31}$$

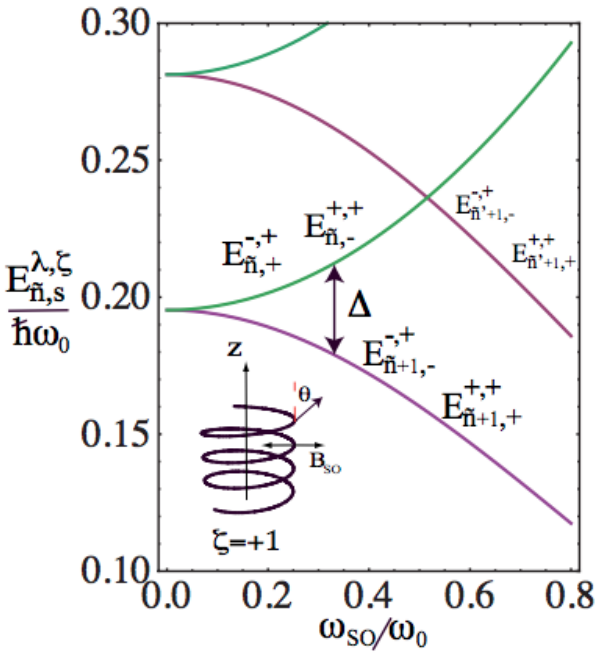

Figure 1.6: Energies of electrons on a counter-clockwise helix ($\zeta = +1$) as a function of the SO interaction strength ω_{SO}. The energy is in units of $\hbar\omega_0$. Each level is doubly degenerate with the index labels indicated. When $\omega_{SO} = 0$ each energy is fourfold degenerate as expected since the time inversion symmetry turns into independent space and spin inversion symmetries. Δ indicates the energy gap between Kramers degenerate states. The inset shows the SO magnetic field and the orientation of the spin for an eigenstate of the spin-orbit coupled system.

Thus, establishing a sense of electron propagation or bias will select a preferred spin direction (lowest energy). The selection of a propagation direction by applying a bias (as in $I-V$ experiments) or by local population imbalance, effectively breaks time reversal symmetry by selecting one of the time reversed partners and generating a net spin collected on the other end of the chiral molecule. Note also that scattering in the helix is suppressed by this gap if the spin is not concurrently flipped by the scattering event [43]. This is exactly the same mechanism for protected transport in chiral edge state in graphene [63].

To further connect with the experimental results, we note that if we change the bias direction for the same chirality label, the preferred spin is the opposite spin direction by choosing the other partner of the Kramers doublet of lowest energy. This change of selected spin is proven in the experiments by the fact that spin injected back into the Ni magnet has to go where the DOS is higher, which is the opposite spin state [43]. The symmetry of the $I-V$ curve in experiments is directly related to the fact that the same degenerate energy corresponds to the forward and backward bias, the change only being which of the two partners in the doublet is selected. The barrier for electrons to be injected into the molecule depend on the work function of the metal, and this is also very similar between Ni and Au (≈ 5 eV), so this is also a source of symmetry.

1.4 Charge and spin currents

Another way to pose spin selectivity is by evaluating the spin currents through the helix. In a coherent regime one can assess spin transport in the helical molecule by computing the expectation value of the velocity operator $\mathbf{J}_{charge} = \Psi^{\dagger} e \mathbf{v} \Psi$, where e is the electron charge and $\mathbf{v}$ is the velocity operator. In the presence of the spin-orbit interaction, the velocity operator is not simply $\mathbf{p}(\mathbb{1}/m)$ (a diagonal matrix) as there arises an additional anomalous velocity term. We start from the quantum mechanical definition of the velocity $\mathbf{v} = (i/\hbar)\,[H, \mathbf{r}]$. The azimuthal velocity component $\partial_t \varphi$, is then

$$v_{\varphi} = \frac{-i\hbar\partial_{\varphi}\mathbb{1}_{2\times 2} - ma\alpha\sigma_{\rho}}{m^{*}\sqrt{a^2+b^2}} \tag{1.32}$$

The Hamiltonian takes a simple form when expressed in terms of the velocity: $H = \frac{1}{2} m^{*} v_{\varphi}^2$. This result is a manifestation of the possibility to write the SOC as a gauge field [55] and thus a gauge invariant velocity as defined in Eq. (1.32). Note that all the manifestations of spin filtering have been observed in biased setups. In the free electron case, photoelectrons are emitted from the metallic surface in contact with one end of the molecules, and travel in a preferred direction. Also, in the localized regime, molecules

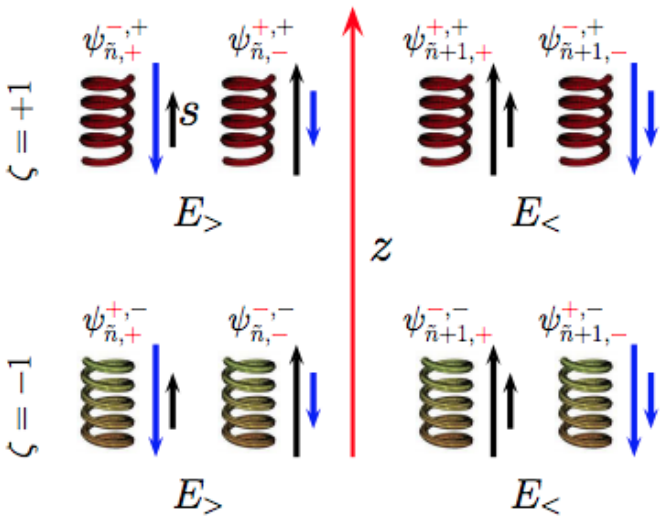

Figure 1.7: Electron propagation direction coupled to spin orientation and the corresponding energies for the two possible chiralities of the helix. Each energy is doubly degenerate (Kramers doublet). If the electron propagates on a $\zeta = +1$ helix in the positive z direction (as indicated), the lower energy state corresponds to the spin up state, while the spin down state has to pay the energy gap Δ.

are biased in a particular direction selecting the preferred sense of transport of the electrons. This bias, as argued before, breaks time reversal symmetry and chooses between the states depicted in Fig. (1.7). We compute the charge currents for the biased system in the positive z direction

$$J^{+,+}_{\tilde{n}+1,+} = -\frac{\hbar b\left[\tilde{n}+1-\frac{1}{2}\sqrt{1+\left(\frac{\omega_{S0}}{\omega_0}\right)^2}\right]}{m^*\sqrt{a^2+b^2}} \tag{1.33}$$

$$J^{+,+}_{\tilde{n},-} = -\frac{\hbar b\left[\tilde{n}+\frac{1}{2}\sqrt{1+\left(\frac{\omega_{S0}}{\omega_0}\right)^2}\right]}{m^*\sqrt{a^2+b^2}} \tag{1.34}$$

Thus, different spin states propagate at different velocities generating a net spin filtering effect. The net spin current vanishes for either SO zero or zero chirality ($b = 0$). The difference is a net spin up current in the positive z direction

$$\mathcal{J} = J^{+,+}_{\tilde{n}+1,+} - J^{+,+}_{\tilde{n},-} = \frac{\hbar b}{m^*\sqrt{a^2+b^2}}\left[\sqrt{1+\left(\frac{\omega_{SO}}{\omega_0}\right)^2}-1\right] \tag{1.35}$$

The longitudinal spin transport current is well defined and can be calculated as

$$\mathcal{J}^{+,+}_{\tilde{n},z} = (\Psi^{+,+}_{\tilde{n}+1,+})^\dagger \frac{1}{2}\{v_\varphi, s^z\}\Psi^{+,+}_{\tilde{n}+1,+} + (\Psi^{+,+}_{\tilde{n},-})^\dagger \frac{1}{2}\{v_\varphi, s^z\}\Psi^{+,+}_{\tilde{n},-} \tag{1.36}$$

The longitudinal spin current depends on the spin-orbit coupling through θ. The spin filtered in the z direction disappears when the SO coupling is zero ($\theta = 0$). Again, the pitch dictates the strength of the vertical spin current and both the pitch and the SOC must be present. Note that the factor $(1 - \cos\theta) = \varphi_{AA}/\pi$ is the nonadiabatic Aharonov-Anandan phase found by Frustaglia and Richter in a detailed analyses of conductance through SO coupled rings [48]. This phase offers a new insight into spin filtering of chiral molecules since in the strong SO limit it is related to the Berry phase of the spin and for the general case it is controlled by non adiabatic spin precession.

1.5 Room temperature spin-selectivity

The spin selectivity demonstrated by experiments is a room temperature phenomenon. Thus any coherent mechanism must be limited by decoherence lengths [31, 46]. The gap for degradation of spin selectivity found in experiments is very high, 0.5 eV (ref. [16]), compared to thermal effects at room temperature 25 meV. This gap prevents elastic backscattering and

exponentially reduces inelastic scattering with the same spin. A spin coupled scattering mechanism, nonetheless, could degrade the spin selectivity rapidly because of the existence of the Kramers doublets as a backscattering channel (see Fig. 1.7).

If one proposes a decoherence length operating at room temperature, one can also suggest a mechanism which preserves spin selectivity analogous to that proposed in ref. [46] and [31], where relaxation of phase coherence occurs within a few nanometers while spin selectivity is preserved. This mechanism entails an exponential decay of the transmission with a decay rate [57] of $\beta = -(1/d_{coh})ln\left[t_{eff}/(E_\alpha - (E_F - eV/2))\right]$ where E_α is the energy of the spin preffered channel, t_{eff} is the hopping integral between sites separated by a coherence length d_{coh}, E_F is the Fermi energy and V the applied bias. Then increasing the number of d_{coh} by having longer molecules will make the input current decrease exponentially, so an increased bias is needed to achieve the same output current. This mechanism might be the source of the increased barrier for spin selectivity as the molecule is elongated. Again, there is no mechanism for the coupling to backscattering channels with the same spin (See Fig. 1.7) so that there will be degradation of spin current but not of spin polarization.

1.6 Summary and discussion

We have examined a model for chiral spin selectivity on a spin orbit active helix with N turns. The origin of the SO electric field comes from the atomic cores of the carbon atoms which provide, through the p_z orbitals, a narrow band for transport. The resulting channels of the model helix are Kramers doublets involving opposite propagating and opposite spin projections at the same energy. An applied bias or otherwise preferred transport direction will then select a spin and effectively break time reversal symmetry (choosing one in a doublet pair), and transferring a particular spin. The resulting spin current is the spin selectivity mechanism. The spectrum of the model also insures suppressed backscattering by an energy gap controlled by the SO energy and the interbase coupling of the p_z orbitals.

The model here can be made more quantitative in many directions. The derivation of the Hamiltonian directly from the tight-binding descriptions is desirable so that one can properly account for the geometry of the orbitals participating in transport. We have solved a variation of the problem more akin to the geometry of the p_z orbitals in carbon nanotubes, where they rotate on the outside of a cylinder. Although the resulting Hamiltonian is different in detail the same physics described here follows. This is expected from the symmetry arguments that result in Kramers doublets separated by

a gap. Contemplating the double helix structure of DNA, could also bring about new interference effects that might enhance or reduce spin selectivity [46] and bring the model quantitatively closer to the experiments. Finally, incorporating the metallic contacts to the chiral molecule through the thiol groups, should introduce level broadening to the spectrum of the molecule and determine the escape rate of electrons and possible charging phenomena.

Chapter 2

Topological features of engineered arrays of adsorbates in honeycomb lattices

2.1 Introduction

Adsorbates and vacancy effects in graphene have been a major field of research in recent years. An isolated vacancy gives rise to localized resonance states near the Fermi level [58, 59]. Hydrogen adatoms are expected to form a strong covalent bond with a carbon atom in the graphene lattice. The bond effectively removes one π orbital in the graphene band, leading to a sharp resonance near the Fermi energy, in a similar way to the case of the vacancy [60]. The electron-electron repulsion prevents doubly occupied states of this resonance, and leads to the formation of a magnetic moment. In addition, the carbon atom coupled to the hydrogen atom is displaced from the graphene plane, inducing a local sp^3 hybridization, which increases the spin-orbit coupling [61, 62].

The intrinsic spin-orbit coupling in a perfect graphene layer creates a gap, and turns graphene into a topological insulator [63]. The presence of magnetic moments induces an exchange coupling with the spins of itinerant electrons, and breaks time reversal symmetry. The combination of a uniform exchange coupling and the extrinsic Rashba coupling in graphene leads to a quantum anomalous Hall phase [65]. This phase is an example of systems which do not show time reversal symmetry and have topologically protected edge states without Landau levels [66].

The effect of a uniform magnetic field and the spin-orbit coupling has

been extensively studied in silicene [67–69]. The possibility of inducing non trivial topological features in the electronic structure of graphene by the addition of heavy atoms has also been considered [70–72], and non trivial features associated to the spin-orbit coupling have been found in lead intercalated CVD graphene [79].

The formation of magnetic moments near vacancies and hydrogen atoms in graphene has been extensively investigated [73], both theoretically (see, for instance [74,76–78,204]), and experimentally [80–84]. On the other hand, it is known that adsorbates on graphene form ordered arrays in a variety of situations [85, 86]. Adatoms on graphene interact among themselves, and can form a variety of ordered patterns, one of them is the Kekulé ordering, which we will treat in detail in chapter 4 of this thesis [90, 132, 140]. More importantly, as shown recently, hydrogen adsorbates can be manipulated with a scanning tunnel microscope (STM) tip [88] allowing to create artificial hydrogen arrangements.

In this work we will focus on the effect of top-adsorbates when they form a periodic arrangement, which can be achieved by selectively moving atoms with an STM. In particular, we will focus on the combined effects of the exchange coupling and modified spin-orbit coupling due to hydrogen adsorbates which form a regular array. The chapter is organized as follows: in this introductory section, we will discuss some of the background necessary to understand our proposal: hydrogen-induced magnetism and spin-orbit couplings in graphene, and previous models for the Quantum Anomalous Hall (QAH) effect in graphene. In section (2.2) we present the model Hamiltonian for supercells of hydrogenated graphene. In section (2.3) we study the topological properties of the hydrogenated graphene superlattice considering only the local adatom-induced SO couplings. In section (2.4) we proceed to study related situations, where the spin-orbit coupling throughout the entire lattice cannot be neglected. In Section (2.5) we consider the situation when the Fermi level is moved away from half filling and crosses the bottom of the conduction band. Section (2.6) compares the band structures obtained from our approach and those obtained from a self-consistent mean-field treatment of the Hubbard model. Section (2.7) discusses the issue of magnetic anisotropy caused by the spin-orbit interactions in the honeycomb crystal. In section (2.8) we discuss the most relevant results, and the open questions raised.

2.1.1 Spin-orbit coupling in graphene

The intrinsic spin-orbit coupling, also known as Kane-Mele coupling, respects all the symmetries of the graphene lattice (point group symmetry D_{6h}), and has the form of an imaginary hopping between second neigh-

bors [63]:

$$H_{KM} = i\frac{\lambda_I}{3\sqrt{3}} \sum_{<<i,j>>} \nu_{i,j} c_i^\dagger s_z c_j \tag{2.1}$$

where s_z is the z- component Pauli matrix acting on the spin subspace $\nu_{i,j}$ is +1 (-1) if the second-neighbor hopping is anti-clockwise (clockwise). Around the Dirac points the intrinsic SOC takes the form of a mass term with opposite signs at different valleys $H_{KM} = \lambda_I \sigma_z \tau_z s_z$; like the regular mass term, it opens a gap around the $\mathbf{K}$ and $\mathbf{K}'$ points of magnitude $2\lambda_I$. However, the magnitude $\lambda_I \approx 12\mu$eV of the intrinsic SOC is too weak to induce an experimentally observable gap [64]. Later, we will see that this gap is topologically non-trivial, inducing a Quantum Spin Hall effect in graphene.

The presence of a substrate or the application of an external electric field perpendicular to the graphene sample break the mirror symmetry $z \to -z$ of the system. This produces the Rashba term:

$$H_R = \frac{2i}{3}\lambda_R \sum_{\langle i,j \rangle} c_{is}^\dagger c_{js'} \left[(\mathbf{s} \times \hat{d_{i,j}})_z \right]_{ss'} \tag{2.2}$$

which splits the double-degeneracy of the bands, a manifestation of the inversion symmetry breaking. The spin-orbit interaction can be enhanced by adsorption of adatoms in the graphene lattice, the case of hydrogen adsorption was studied in ref. [62], in the dilute limit this leads to non-uniform spin-orbit terms:

$$\begin{aligned} H_{SO} \;=\; & \\ & \frac{i}{3} \sum_{\langle\langle C_H,j \rangle\rangle} c_{C_H,s}^\dagger c_{js'} \left[\frac{\Lambda_I}{\sqrt{3}} \nu_{C_H,j} s_z \right]_{ss'} + H.c. \\ + \;& \frac{2i}{3} \sum_{\langle\langle C_H,j \rangle\rangle} c_{C_H,s}^\dagger c_{nn,j,s'} \left[\lambda_R (\mathbf{s} \times \hat{d_{C_H,j}})_z \right]_{ss'} + H.c. \\ + \;& \frac{2i}{3} \sum_{\langle\langle i,j \rangle\rangle} c_{nn,i,s}^\dagger c_{nn,j,s'} \left[\Lambda_{PIA} (\mathbf{s} \times \hat{D_{i,j}})_z \right]_{ss'} \end{aligned} \tag{2.3}$$

where C_H is the hydrogenated carbon site. The third term (Λ_{PIA}) induces spin-flipping hoppings between the nearest neighbors of C_H. The SO coupling strengths are $\lambda_R = 1.14 \times 10^{-4}\ t$, $\lambda_{PIA} = -2.66 \times 10^{-4}\ t$ and $\lambda_I = -7.26 \times 10{-}5\ t$, where t is the hopping between nearest-neighbors in graphene.

2.1.2 Models for Quantum Anomalous Hall effect in graphene

The Quantum Anomalous Hall effect is a topological insulating phase, it possesses chiral edge states without back-scattering, and a breaking of time-

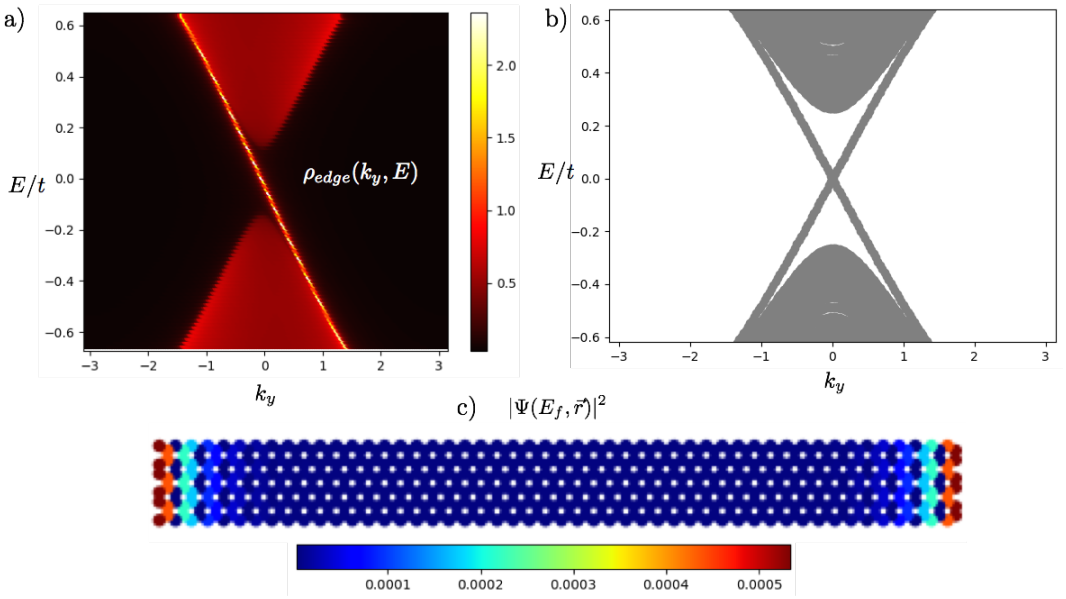

Figure 2.1: (a) Local density of states at the edge of a semi-infinite graphene in the (k_y, E) plane (b) Band structure of armchair graphene nanoribbon from the Haldane model with $t_H = 0.05$ t. (c) Distribution of the probability density at $E = E_{fermi}$, in the geometry of the armchair nanoribbon from part (b), showing that the midgap state is localized at the edges

reversal symmetry. The Hall conductance is quantized as $\sigma_{xy} = \mathcal{C}\frac{e^2}{\hbar}$, where the integer $\mathcal{C}$ is called the Chern number, and represents the number of chiral edge states (we explain how the Chern numbers are calculated in Appendix A). Unlike the Quantum Hall phase, however, the QAH phase is not caused by an external magnetic field, but by internal degrees of freedom such as spin-orbit coupling or exchange fields, thus showing the same phenomenology as the Quantum Hall phase without the flat Landau levels in its band structure. In this subsection, we will discuss previous theoretical proposals for the realization of the QAH-phase in graphene.

The first model for a QAH-effect, due to Haldane [66] consists of spinless fermions in a honeycomb lattice, moving under the influence of local magnetic fields with different signs within the hexagon, producing a zero net-flux through the hexagon. The Hamiltonian, that takes into account the Haldane fields in the honeycomb lattice is:

$$H = -t \sum_{<ij>} c_i^\dagger c_j + i t_H \sum_{<<i,j>>} \nu_{i,j} c_i^\dagger c_j \tag{2.4}$$

where t_H is the strength of the Haldane hopping; notice that the local magnetic fields in the Haldane model give rise to an imaginary hopping between second neighbors, where $\nu_{i,j} = (\hat{d}_1 \times \hat{d}_2)_z$ is the chirality of the path for second neighbor hoppings (i.e. the hopping changes signs depending on whether the closest path for hopping is clockwise or counter-clockwise). For second neighbors i, j with a common first neighbor k, the unit vectors $\hat{d}_1$ and $\hat{d}_2$ point along the directions of the ik and kj bonds. The bulk bandstructure for the Haldane model is gapped, but the bands for the armchair nanoribbon show the presence of two midgap states, see panel (b) of Fig. (2.1), panel (c) shows the localization of the midgap states in the edges of the nanoribbon. Another technique for visualizing the localization of the mid-gap states is to obtain the LDOS at the edge of semi-infinite graphene crystal:

$$G_{edge}(E, k_{||}) = \left[(E + i\eta) - H_0(k_{||}) - \Sigma(E, k_{||})\right]^{-1} \tag{2.5}$$

where $\Sigma(E, k_{||}) = t^\dagger G_{edge}(E, k_{||}) t$ is the self-energy term representing the coupling between the edge unit cell and the rest of the semi-infinite crystal. Eq. (2.5) is solved numerically via self-consistent iterations. Once converged, the surface density of states in the edge unit cell is calculated as:

$$\rho_{edge}(E, k_{||}) = -\frac{1}{\pi} Im[G_{edge}(E, k_{||})] \tag{2.6}$$

Plots of the DOS in the $E, k_{||}$ plane reveal the presence of midgap edge states. In the case of the Haldane model, we find one edge state in each edge, see panel (a) of Fig. (2.1). Although Haldane's proposal is a highly

idealized model, it remains relevant because it forms the basis of the model for Quantum Spin Hall effect in the presence of intrinsic spin-orbit coupling, which was proved by Kane-Mele to be mathematically equivalent to two copies of the Haldane, one for each spin, traveling in opposite directions at the edges, thus yielding zero net charge-current but a non-zero spin current.

Another interesting model for the realization of the QAH phase in graphene, based in the interaction between exchange field and Rasba spin-orbit interaction,was proposed by Qian Niu and coworkers [65]. The model Hamiltonian is:

$$H = -t \sum_{<ij>} c^{\dagger}_{i\alpha} c_{j\alpha} + \frac{2i}{3} \sum_{\langle i,j \rangle} c^{\dagger}_{is} c_{js'} \left[\lambda_R (\mathbf{s} \times \hat{d_{i,j}})_z \right]_{ss'} + \Delta \sum_{is} c^{\dagger}_{is} \sigma_z c_{is} \quad (2.7)$$

The first term in eq.(2.7) represents the hoppings between nearest-neighbors in graphene, the second term is the Rashba spin-orbit interaction, and the third term is the exchange field that couples to the off-plane spin-component. The combination of exchange field and Rashba interaction opens a gap in graphene. An integration of the Berry curvature of the valence bands in the Brillouin zone yields a Chern number $\mathcal{C} = 2$, see Fig. (2.3). The band structure of an armchair nanoribbon with $\lambda_R = 0.1$t and $\Delta = 0.18$ t is shown in Fig. (2.2), showing the mid-gap states. The two-edge states obtained from the surface Green function in the armchair edge of a semi-infinite plane can be seen in Panel (a) of Fig. (2.2), confirming the result obtained via the calculation of the Chern number.

2.1.3 Magnetism due to single-H adatom and H-dimers in graphene

Although speculated for several years, concrete evidence of magnetism in graphene due to the adsorption of hydrogen adatoms was only found for the first time in a recent experiment by González-Herrero et al. [91]. Given that our study of the QAH-phase in this chapter is based on the H-induced magnetism, and that H-adatoms are the prime example of the top-adatoms that we will consider in Chapter 3, we will address here the main findings of that experiment.

The focus of [91] begins by investigating the effect of a single H-adatom. The H-adatom is adsorbed on top of a carbon atom and changes the sp^2 hybridization into an sp^3, and removes the p_z orbital of the hydrogenated carbon atom. This removal creates a resonant peak at the Fermi energy (E_F). This state is expected to become spin-polarized because the Coulomb repulsion between two electrons of different spin energetically favors occupancy by one spin. The adatoms were visualized by scanning tunneling

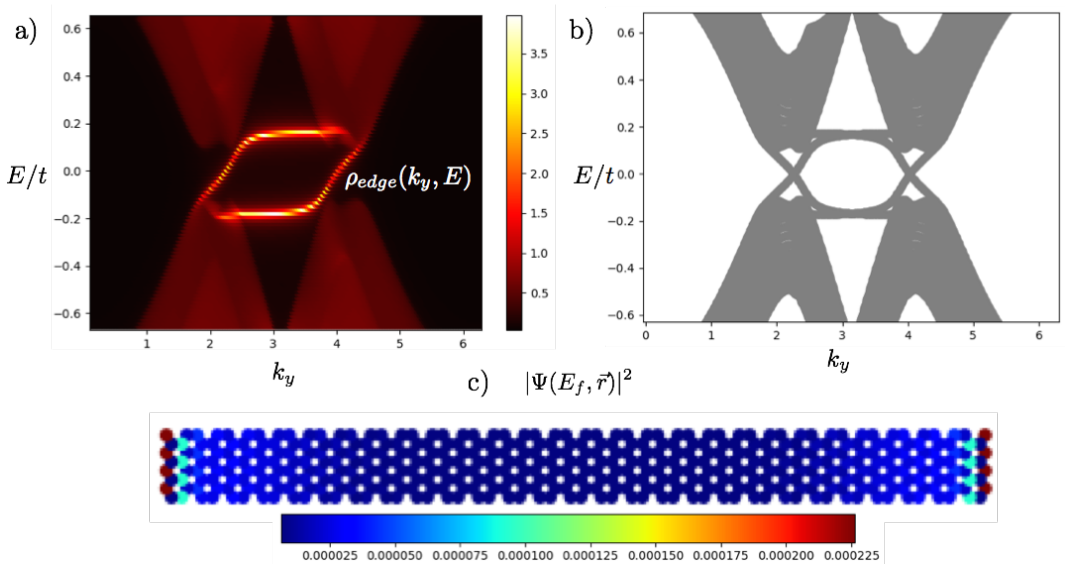

Figure 2.2: (a) Local density of states at the edge of a semi-infinite graphene in the (k_y, E) plane (b) Band structure of armchair graphene nanoribbon with $\lambda_R = 0.1$t and $\Delta = 0.18$ t. (c) Distribution of the probability density at $E = E_{fermi}$, in the geometry of the zigzag nanoribbon from part (b), showing that the midgap state is localized at the edges

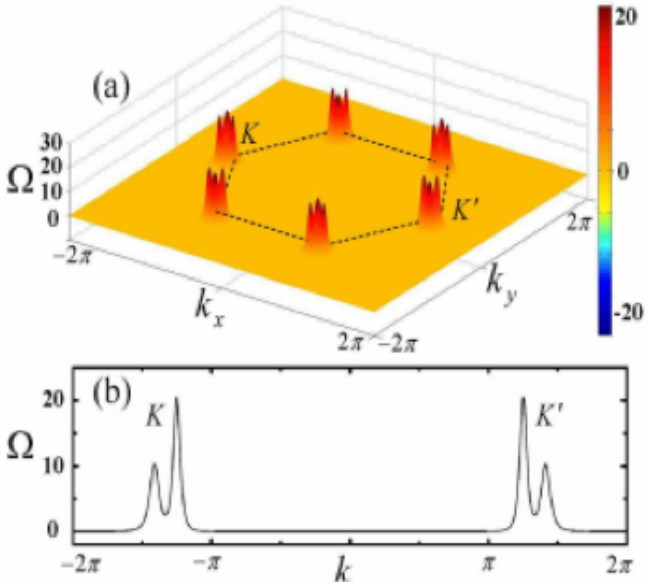

Figure 2.3: (a) Berry curvature of the valence bands of bulk graphene in reciprocal space with $\lambda_R = 0$ t and $\Delta = 0.18$t (b) Cut of the Berry curvature along $k_y = 0$. Integration of the Berry curvature within the Brillouin zone gives a Chern number $\mathcal{C} = 2$. Adapted with permission from [65]

microscopy (STM) as a bump surrounded by a pattern of three "arms" separated by 120°. The shape of the LDOS vs energy is probed via differential conductance spectra (dI/dV curve) under the tip of the STM. The dI/dV measurements on top of the H adatom yield two sharp peaks, one above and one below E_F, separated from each other by 20 meV, see panel C in Fig. (2.4).

These two peaks, are expected to be spin-polarized by the argument mentioned above, but how can we be certain that the two-peak structure near E_F is in fact due to spin-splitting? The Anderson impurity model (AIM) [110] gives a simple reasoning to figure this out, therefore although the AIM will be discussed in more detail in the next chapter, it is convenient to mention some of its relevant features here. The magnetic or non-magnetic behavior of an adsorbed impurity within the AIM is determined by three parameters: the separation between the impurity level E_d and the Fermi level E_F (which can be manipulated via electronic doping), the energy-width of the impurity state Δ (which is determined by its coupling to the host metal, i.e, it is an extremely narrow peak in the decoupled limit, acquiring a significant with as coupling is increased), and of course the magnitude of the electron-electron repulsion U. A phase diagram of the magnetic and non-magnetic behaviors of the Anderson impurity, in terms of dimension-less parameters $x = (E_F - E_d)/U$ and $\pi\Delta/U$, is shown in Fig. (2.5). Regions $E_d > E_F$ and $E_d + U < E_F$ (which are not shown in the phase-diagram) are non-magnetic for all values of Δ. It is thus clear that the most favorable electron-doping for magnetic behavior is such that $x = 0.5$, and that as E_F is shifted in any direction, the spin-splittting (and the magnetic moment) first decreases and then vanishes for some critical doping value, see panel (f) in Fig. (2.5). Thus, the AIM predicts that as the distance between the impurity peak E_d and E_F is increased, at some point a transition to a non-magnetic state with only *one* sharp peak must occur, see Fig. (2.5); on the other hand, if the two-peak structure were not caused by magnetism, only a rigid shift of the two-peaks with respect to E_F should be observed. Indeed, the idea of on- and off-switching the magnetic moments due to adatoms in graphene via doping was previously applied by Nair et al [111].When the dI/dV spectra of the doped sample of graphene were measured the two-peak structure was destroyed and only one sharp peak was observed, thus yielding a compelling argument for the magnetic nature of the two-peak splitting, see panel F in Fig.(2.4).

The spatial distribution of the magnetic state was also investigated. Fig. (2.6 A) shows a conductance map $dI/dV(x, E)$ measured at every atomic site along the line shown in Fig. (2.6 B). This esentially measures the size of the resonant impurity peak at every site; it was found that this state

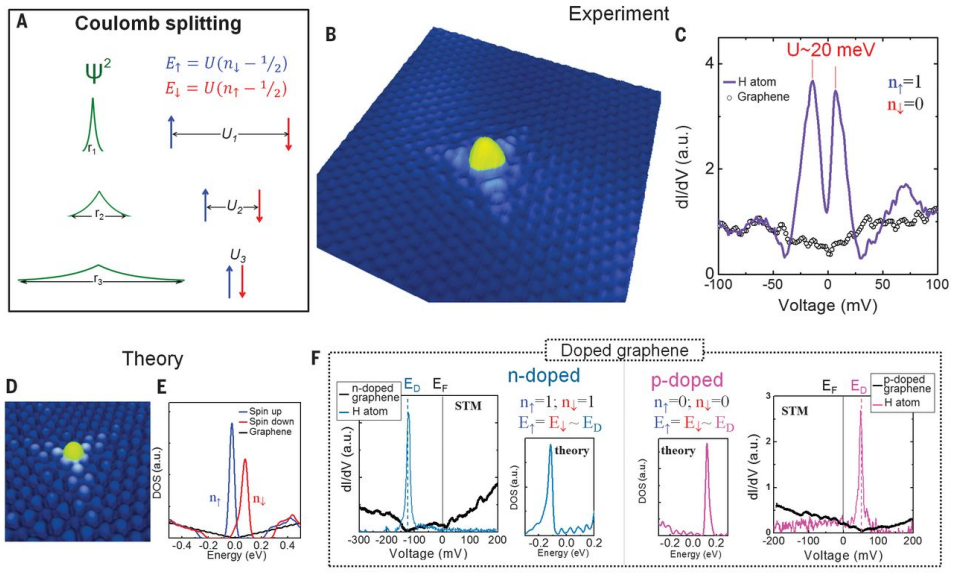

Figure 2.4: A) Illustration of the origin of the spin-split state in terms of its spatial extension given by the square of its wave-function and the Coulomb repulsion U. Arrows indicate the positions of the energies for spin-up ($n_\uparrow$) and spin-down ($n_\downarrow$) levels. For a fully polarized one-electron state, the majority level spin is filled and the minority one is empty, therefore $n_\uparrow = 1$ and $n_\downarrow = 0$ and the energy splitting $E_\uparrow - E_\downarrow$ is given by U B) STM topography of a single H atom chemisorbed on neutral graphene (0.2 V, 0.1nA,7×7 nm^2) C) dI/dV spectrum measured on the H atom, showing a fully polarized peak at E_F, and measured on bare graphene far from the H atom. The spectra were acquired at a nominal junction impedance of 2 gigaohms. D and E) DFT-simulated STM image (D) and DOS (E) of an H atom chemisorbed on neutral graphene. F) dI/dV spectra and DFT calculations of the DOS induced by a single H atom on n- (left) and p-type (right) doped graphene. The minimum of the dI/dV spectra, acquired on bare graphene (black curves) determines the position of E_D . All experimental data were acquired at 5K. Adapted with permission from [91]

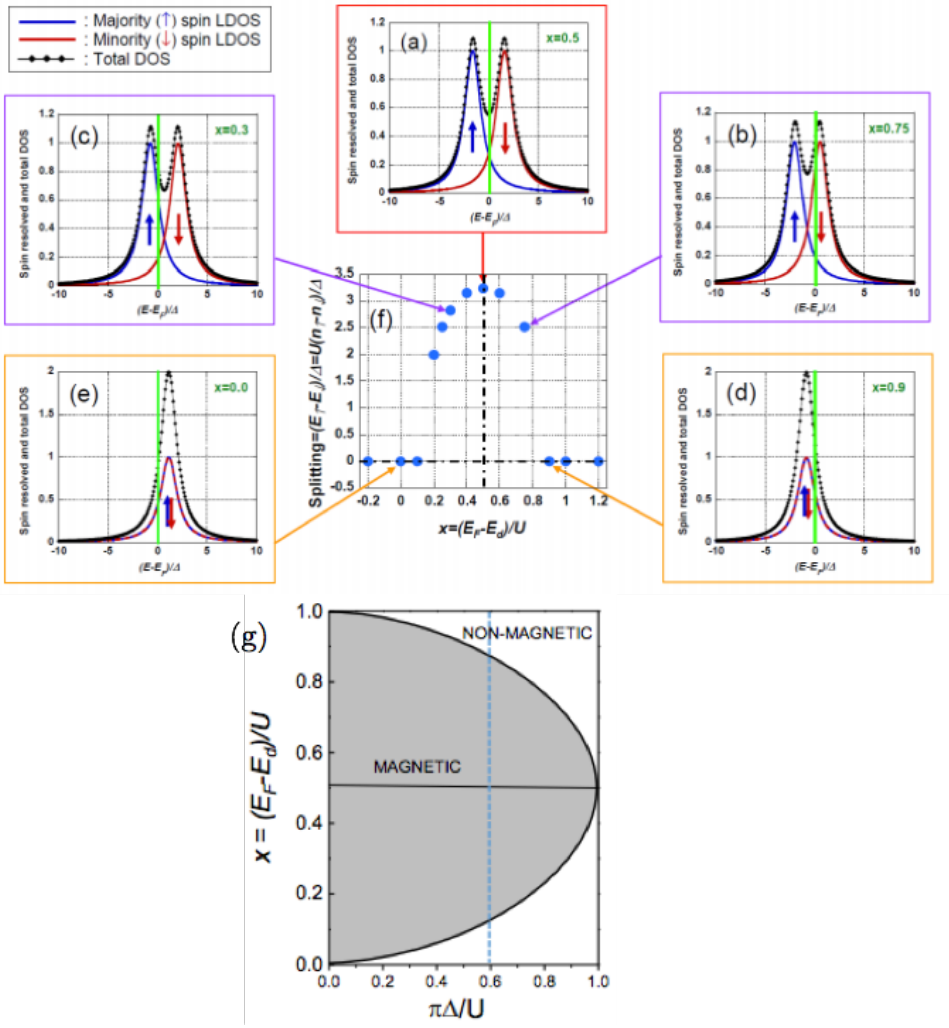

Figure 2.5: (a-e) Evolution of the spin-splitting for different values of doping within the Anderson impurity model (f) Maximum splitting is achieved at $x = 0.5$ (meaning that the E_F is half-way between the $\uparrow$ and $\downarrow$ peaks) (g) Phase-diagram showing the regions of magnetic and non-magnetic behavior for an Anderson impurity. Vertical lines in the phase diagram correspond to modifications of the distance between the impurity level E_d and the Fermi level E_F which can be accomplished via electron-doping. Adapted with permission from Supplementary Material of [91]

is concentrated in sites corresponding to the sublattice opposite to the one where the H is adsorbed (being nearly non-existent in the same sublattice). Furthermore, the size of the magnetic moment and the occupied peak at every carbon atom were highly correlated, see Fig. (2.6 C).

The interaction between H-H dimers was also addressed. When the H-adatoms lie on the same sublattice (AA-dimer) the coupling between the adatoms is ferromagnetic, whereas for the AB-dimer, the solution is non-magnetic. Interestingly, their calculations for the total interaction energy for the dimers relative to the energy of two infinitely separated H-adatoms always yield an attractive result; that is, dimer-formation is favorable at least for the distances shown in Fig. (2.7 A). In the next chapter we will address the interaction between adatoms in AA and AB configurations, we will find that our result for AA adatoms is in agreement with the González-Herrero et al experiment (i.e. the coupling is ferromagnetic), whereas for AB pairs at large distances our result yields an antiferromagnetic coupling, we will also find parameters for which dimer formation is energetically favored, depending on the strength of the adsorbate-graphene coupling. dI/dV measurements show a spin-split peak near E_F for the AA-dimer, whereas for the AB-dimer it shows featureless v-shape structure like that of pristine graphene (consistent with a non-magnetic solution) Fig. (2.7 E).

2.1.4 Magnetism due to periodic arrays of hydrogen-like adatoms

Having discussed the adsorption of single and pair H-adatoms from [91], we now move on to the case of graphene superlattices with a periodically arranged H-adatoms. As seen in the previous subsection, when a hydrogen atom is adsorbed on top of a carbon atom, the sp^2-symmetry is locally broken, and the electron from the C p_z orbital is removed from the π bands to form a σ bond with the H atom (Fig. 2.8 (a)), effectively removing the p_z orbital from the lattice. Therefore the electronic structure of hydrogenated graphene is very similar to that of graphene with a vacancy, therefore in the simplest approximation, one can use a vacancy as a model for a hydrogen adatom. Periodically hydrogenated graphene shows a flat-band near the Fermi level. In order to describe the magnetism that arises in graphene due to hydrogen adsorption, we introduce the onsite Coulomb repulsion between electrons of different spins (same-spins are already taken into account by the Pauli exclusion principle):

$$H = -t \sum_{<ij>,\sigma} c^{\dagger}_{i\sigma} c_{j\sigma} + U \sum_{i} n_{i\uparrow} n_{i\downarrow} \tag{2.8}$$

Operators $n_{i\sigma} = c^{\dagger}_{i\sigma} c_{i\sigma}$ represents the number of electron with spin σ in the i-th site, and t is the hopping between nearest neighbor carbon atoms,

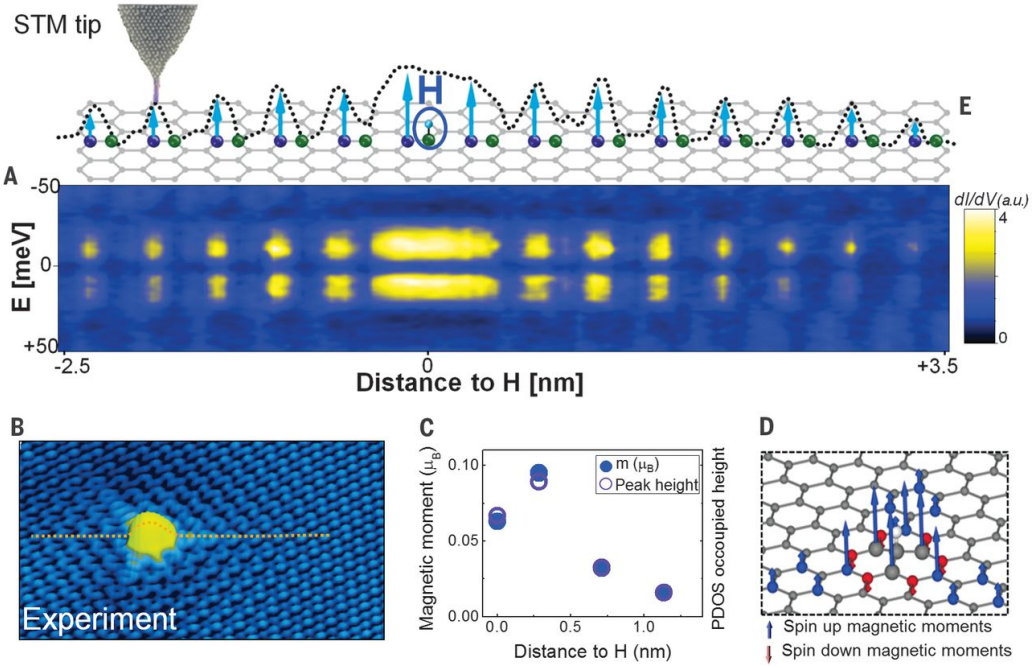

Figure 2.6: A) Conductance map $dI/dV(x, E)$ along the dashed line in B) . The spectra were acquired at a nominal junction impedance of 3 gigaohms B) STM topography of a single H atom on graphene C) Comparison between DFT calculations for the local magnetic moment and the height of the occupied projected DOS (PDOS) peak, calculated on different carbon atoms. D) Calculated magnetic moments induced by H chemisoprtion (the lengths of the arrows signify the relative magnitudes of the magnetic moments) E) Schematic of the graphene structure along the dashed line in B). Green (purple) balls indicate the positions of carbon atoms belonging to the same (opposite) sublattice with respect to the locus of H chemisorption. The dotted line shows the evolution of the height of the measured occupied peak, and the arrows show the relative magnetic moment contribution of each carbon atom. All experimental data were acquired at $T = 5$ K. Adapted with permission from [91]

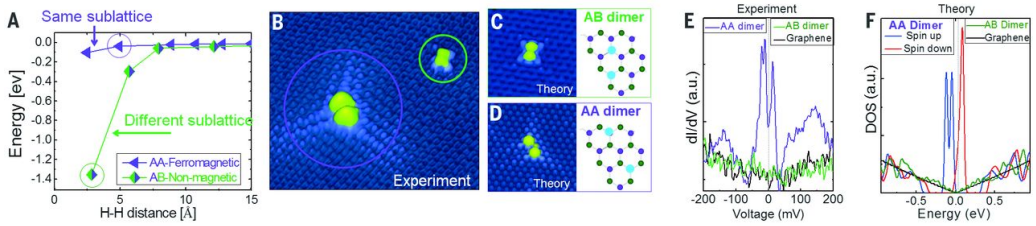

Figure 2.7: A) Calculated total energy, relative to twice the adsorption energy of a single H atom, and magnetic stateof a pair of H atoms adsorbed on the same (AA dimer) and different (AB dimer) sublattices, plotted as a function of the H-H distance. B) STM image showing two different pairs of H atoms, with one pair in an AA (purple circle) and the other pair in an AB (green circle) configuration (0.2 V 0.1 nA, 7.8×6.6 nm^2) C) Calculated STM image of the AB dimer and D) the AA dimer with the corresponding diagrams for H atoms (blue balls) on graphene (purple and green balls). E) Experimental dI/dV spectra and F) calculated DOS for the AA dimer, AB dimer and clean graphene. The spectra were acquired at a nominal junction impedance of 8 gigaohms. All experimental data were acquired at 5 K. Adapted with permission from [91]

although, importantly, this sum does not include the orbital of the carbon atom that hosts the H-adatom (thus treating it like a vacancy). The formal expression for the Hubbard repulsion is:

$$U = \frac{e^2}{4\pi\epsilon_0} \int \int d^3\mathbf{r} d^3\mathbf{r}' |\varphi_{\mathbf{r}_i,\sigma}(\mathbf{r}')|^2 \frac{1}{|\mathbf{r} - \mathbf{r}'|} |\varphi_{\mathbf{r}_i,\sigma}(\mathbf{r})|^2 \tag{2.9}$$

where $\varphi_{\mathbf{r}_i,\sigma}(\mathbf{r})$ are the Wannier wave-functions centered around site $\mathbf{r}_i$ of graphene. We will now consider the mean-field approximation of the Hubbard term; under this approximation the $n_{i\sigma}$ operators can be written as small fluctuations ($\Delta n_{i\sigma}$) around the mean value of the operator ($\langle n_{i\sigma} \rangle$), that is $n_{i\sigma} = \langle n_{i\sigma} \rangle + \Delta n_{i\sigma}$; if one substitutes this into expression 2.8, discarding terms that are quadratic in the fluctuations, the Hubbard Hamiltonian can be written as:

$$H = -t \sum_{<ij>,\sigma} c^\dagger_{i\sigma} c_{j\sigma} + U \sum_i [n_{i\uparrow} \langle n_{i\downarrow} \rangle + n_{i\downarrow} \langle n_{i\uparrow} \rangle - \langle n_{i\uparrow} \rangle \langle n_{i\downarrow} \rangle] \tag{2.10}$$

The expectation values $\langle n_{i\sigma} \rangle$ are calculated self-consistently until convergence is achieved, and once again, the summation over graphene sites excludes the site of the carbon atom subject to hydrogen adsorption. The resulting magnetic moments are distributed in the lattice according to the weight of the non-interacting vacancy wave-function $|\Psi_{vac}(E_F, \mathbf{r})|^2$, there-

fore they are primarily concentrated in the sublattice opposite to the hydrogenated carbon, more specifically in its nearest neighbors, see the geometry in Fig. (2.8) panel (c). The long-range magnetic order is ferromagnetic when the hydrogens are in the same sublattice (in agreement with the results for the H-dimers studied by González-Herrero et al. [91]), and antiferromagnetic otherwise. As the distance between the impurities is increased, the magnetic moment in the nearest neighbors m_{nn} decreases and converges for a distance of $d_{HH} = 33.74$ A , or equivalently a 14×14 supercell (0.25 % hydrogenation). This decrease is related to the overlap between the wave-functions of neighboring defects. These results are consistent with Lieb's theorem [112], which states that for bipartite lattices (such as the hexagonal lattice), the ground-state of the Hubbard model with $U > 0$ is unique and has a spin polarization given by:

$$S = \frac{1}{2}(N_B - N_A) \tag{2.11}$$

where N_B and N_A are the number of atoms in sublattices B and A respectively.

Figure (2.9 a) shows the band structure of a triangular superlattice of adsorbates with period 28 a_0 , corresponding to 0.06 % of adsorbed H, calculated using the mean-field Hubbard model . The splitting (Δ_s) of the mid-gap state formed during H adsorption is plotted in Fig. 2.9(b) for different supercell sizes at different k-points. At the K point Δ_s decays as $d_{HH}^{-1.9}$, while at the Γ and M-points Δ_s it goes as d_{HH}^{-1}.

2.2 The Hamiltonian for superlattices of hydrogenated graphene

We will study the topological properties of a periodic array composed of a adatoms on top of a carbon atom in the 5×5 graphene supercell as shown in the first two panels of Fig. (2.10). We describe the electronic structure with a tight binding model with one p_z orbital per carbon atom and a nearest neighbor hopping parameter, t. The effect of the covalent bonding between hydrogen and carbon is approximated by a large shift of the energy of the p_z orbital nearest to the hydrogen atom, ϵ_0. For $\epsilon_0 \approx |t|$ a sharp resonance appears near the vacancy [58], which decays slowly as function of the distance. In the absence of interactions, the resonance is mostly localized in the sublattice which does not include the perturbed p_z orbital.

Due to the large density of states, once electronic interaction is turned on, the localized level at zero energy becomes spin splitted, and a local magnetic moment shows up. [74, 76–78, 204] Therefore, the effect of the electron-electron interaction is to induce a exchange splitting, Δ_Z between

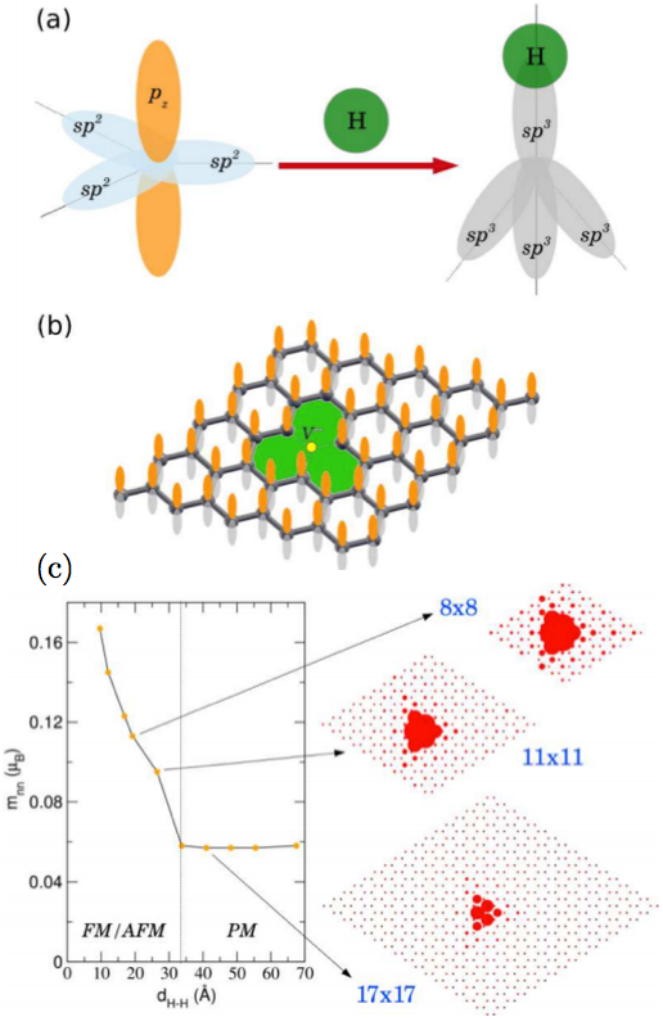

Figure 2.8: (a) Schematic representation of the sp^2 hybridization breakdown under hydrogen adsorption, equivalent to the presence of a single-vacancy (b)Single-vacancy in a 5x5 supercell used in the mean-field Hubbard calculations with periodic boundary conditions. The p_z orbital at the center of the vacancy (yellow site inside the green region) is removed by adding a large on-site potential ($V \to \infty$) to simulate hydrogen adsorption. (c) Evolution of magnetic moments on first neighbor atom for increasing distance between impurities (d_{HH}). The value converges apparently for $d_{HH} \geq 33.74$ A where long range magnetic interactions start to vanish precluding the formation of FM or AFM ordering and leading to isolated paramagnetic defects. To the right, the lattice distribution of magnetic moments for different supercell sizes. (Adapted with permission from [151])

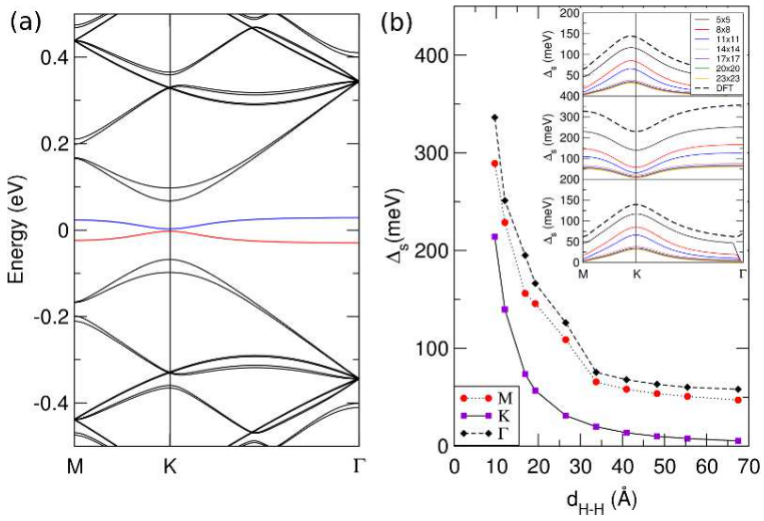

Figure 2.9: (a) Band structure corresponding to 0.06% of H adsorbed (28×28 supercell). The spin degeneracy is broken at the Fermi energy ($E = 0$) due to the formation of local magnetic fields around impurities. (b) Evolution of Δ_s at three symmetry points K, Γ and M, for increasing values of the distance between impurities (d_{HH}). The inset shows the evolution of Δ_s along the $M - K - \Gamma$ path in the hexagonal Brillouin zone of the valence (bottom), impurity (center) and conduction (top) bands. Dashed lines correspond to DFT results. (Adapted with permission from [151])

the spin up and spin down levels at the sites where the resonance is located. This is the effect which arises if the interaction is local and it is treated within a mean field approximation. The orientation of the exchange field with respect to the plane of the graphene layer is determined by the magnetic anisotropy induced by the spin-orbit coupling. In the following we will assume an off-plane direction, which can always be stabilized with an applied magnetic field. The case of in-plane configuration will be dealt with in section 2.7.

The full Hamiltonian for the adatom in the supercell is:

$$H = H_{KIN} + H_Z + H_{SO} \tag{2.12}$$

where H_{KIN} represents the kinetic terms of the Hamiltonian, H_{SO} represents the spin-orbit coupling terms, and H_Z is the exchange splitting due to the magnetism induced by the onsite potential of the adatom, which takes the form of a usual site dependent Zeeman term. In this section we will explain the kinetic and exchange contributions to the Hamiltonian. In the next two sections we will discuss two cases separately: local SO coupling induced by the adatom, and uniform SO coupling induced by a substrate.

The kinetic part of the Hamiltonian, includes an onsite energy at the hydrogen s-orbital, and hoppings between carbon orbitals, and between the adatom s-orbital and the hydrogenated carbon site C_H. However,as explained in [92, 151], via a Lowdin transformation, the H-orbitals can be eliminated, and the Hamiltonian of the adsorbate can be reduced to that of an onsite single-impurity, where the onsite energy goes as the square of the H-C hopping. After this transformation, the kinetic term in the Hamiltonian can be written as:

$$H_{KIN} = -t \sum_{\langle i,j\rangle,s} c^\dagger_{is} c_{js} + \epsilon_o \sum_s c^\dagger_{C_H,s} c_{C_H,s} \tag{2.13}$$

where t is the hopping between nearest neighbors i and j in the honeycomb lattice, ϵ_0 is a large onsite potential in the hydrogenated carbon site (in our calculation we consider it to be 100 times the hopping integral), and $c^\dagger_{C_H,s}$ ($c_{C_H,s}$) creates (annihilates) an electron in the hydrogenated carbon site (C_H). The onsite potential due to the adatom gives rise to a gap between the conduction and valence bands, as well as a vacancy state lying at the Fermi energy. The size of this gap is proportional to the impurity concentration, so that in the dilute limit of an isolated vacancy in graphene, there is a zero energy vacancy state, but no gap.

The vacancy state also produces a non-uniform internal magnetization in the sub lattice opposite to the adatom, which decreases with distance from the impurity site. The local magnetization splits the impurity bands,

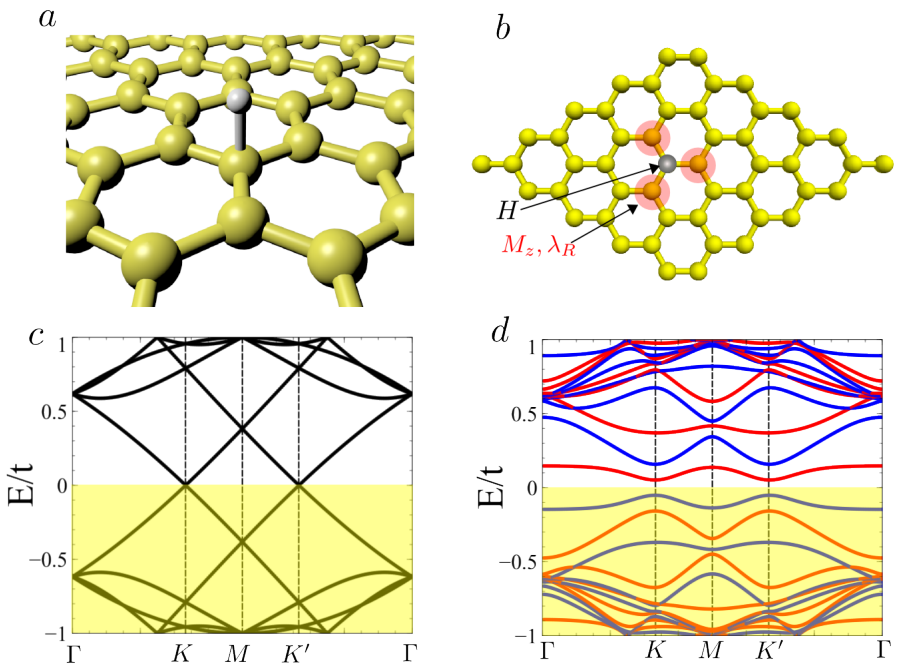

Figure 2.10: Single hydrogen adatom in graphene sheet (a), and unit cell of the simulation (b). As shown in (b), Rashba and exchange fields are located only around the adatom. Band structure of a pristine 5x5 graphene unit cell (c), and with a vacancy and local exchange field (d). The color of the bands shows the expectation value of the spin along the z axis, red represents spin-up and blue represents spin-down states.

creating a gap at the Fermi level, which can be seen in panel (d) of Fig. (2.10). We model this magnetization effect by the exchange splitting term in the Hamiltonian, which has the form:

$$H_Z = \sum_{i_B} \Delta_{i_B} c^{\dagger}_{i_B,s} s_z c_{i_B,s} \tag{2.14}$$

where the i_B label means that the summation is carried out over all sites of the B sub lattice opposite to C_H. Effectively, this term contributes a spin-dependent onsite potential in the B sites. Magnetization terms of opposite sign are induced in the A sub lattice, but these terms only begin to have a significant influence for values of the electron-electron interaction close to the semimetal-antiferromagnetic insulator transition in the honeycomb lattice ($U_c = 2.23t$). Here we restrict ourselves to the case of small U and we neglect those terms (see section 2.6). The splitting magnitude Δ_{i_B} is

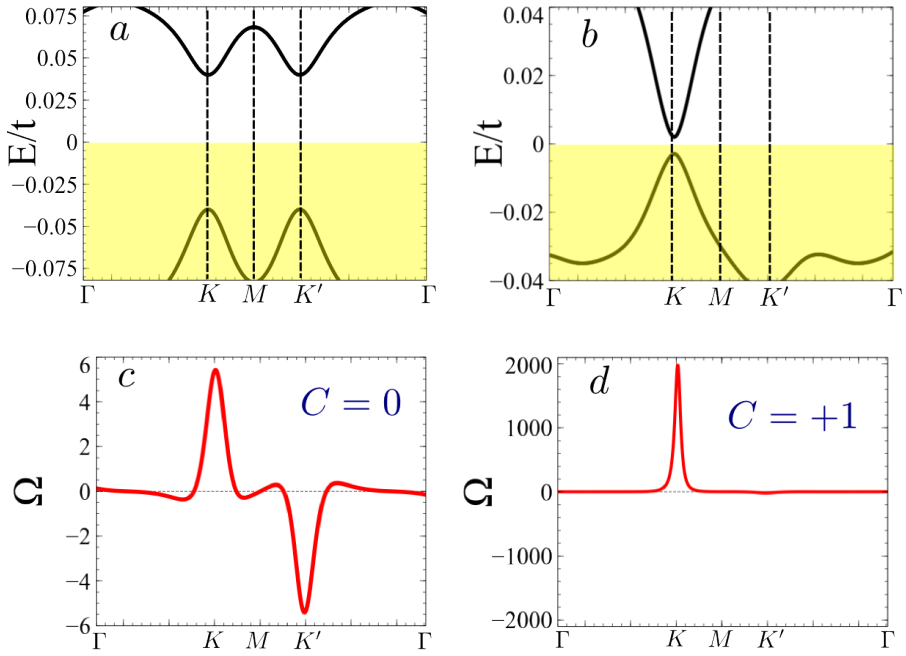

Figure 2.11: Band structures (a,b) and Berry curvatures (c,d) of a graphene supercell with one hydrogen atom, with local Rashba field and local off-plane exchange. Panels (a,c) corresponds to realistic values of λ_R, whereas panels (b,d) corresponds to a large λ_R.

proportional to the magnitude of the vacancy state at site i_B, that is:

$$\Delta_{i_B} = \Delta |\Psi_v(i_B)|^2 \tag{2.15}$$

where Ψ_v is the wavefunction created by the the adatom, which is sublattice polarized and strongly localized near the missing p_z orbital After solving for the band structure of the spin-unpolarized kinetic part of the Hamiltonian, we introduce the sub lattice magnetization via eq. (2.14). This approach is equivalent to perform one iteration of a selfconsistent Hubbard calculation, and importantly it retains the relevant features of the electronic structure even though not being self consistent. Furthermore, we have found that a simplified model that takes into account only the magnetism of the nearest neighbors of the adatom, captures all of the important topological properties of the bands. (see section 2.6).

2.3 Hydrogenated graphene: Local spin-orbit couplings

In this section we discuss the model with local, adatom-induced SO couplings. This model is appropriate for engineered arrays of hydrogen adatoms in graphene, where the uniform intrinsic spin-orbit coupling can be neglected. The Hamiltonian for the spin orbit coupling induced by the adatom is [62]:

$$\begin{aligned} H_{SO} &= \frac{i}{3}\sum_{\langle\langle C_H,j\rangle\rangle} c^{\dagger}_{C_H,s}c_{js'}\left[\frac{\Lambda_I}{\sqrt{3}}\nu_{C_H,j}s_z\right]_{ss'} + H.c. \\ &+ \frac{2i}{3}\sum_{\langle\langle C_H,j\rangle\rangle} c^{\dagger}_{C_H,s}c_{nn,j,s'}\left[\lambda_R(\mathbf{s}\times \hat{d_{C_H,j}})_z\right]_{ss'} + H.c. \\ &+ \frac{2i}{3}\sum_{\langle\langle i,j\rangle\rangle} c^{\dagger}_{nn,i,s}c_{nn,j,s'}\left[\Lambda_{PIA}(\mathbf{s}\times \hat{D_{i,j}})_z\right]_{ss'} \end{aligned} \tag{2.16}$$

Where $\mathbf{d}_{C_H,j}$ is the unit vector connecting C_H to its nearest neighbors, and $\mathbf{D}_{i,j}$ is the unit vector connecting the second neighbors of C_H. The operator $c^{\dagger}_{nn,j,s}$ ($c_{nn,j,s}$) creates (annihilates) electrons of spin s in the jth nearest neighbor of C_H, whereas $c^{\dagger}_{C_H,s}$ creates an electron at C_H.The first term describes the adatom modified intrinsic SO coupling Λ_I, which induces spin-preserving hoppings between C_H and its second neighbors. The second term (λ_R) describes the Bychkov-Rashba hoppings caused by the local breaking of space inversion symmetry around the adatom site. It induces spin-flipping hoppings between C_H and its nearest neighbors. The third term (Λ_{PIA}) induces spin-flipping hoppings between the nearest neighbors of C_H. We have neglected in this section the intrinsic SO coupling of pristine graphene, which induces hoppings between second neighbors not containing C_H.

The presence of Rashba interaction and an exchange field in the sites where the impurity bands are located, strongly suggests the possibility of reaching a Quantum Anomalous Hall (QAH) state, via a topological phase transition occurring in the corresponding gap. We inspect the topological properties of the valence bands of the bulk system, by calculating the Chern number

$$\mathcal{C} = \frac{1}{2\pi}\sum_n \int_{BZ} \Omega_n(k_x,k_y)d^2k \tag{2.17}$$

where the integral is carried out over the first Brillouin zone, and the summation is carried out over all valence bands (see Appendix A for a more detailed description of the calculation method for the Chern number). The Chern number gives the number of chiral edge states at each edge of a

nano ribbon, and is related to the quantized charge Hall conductance via $\sigma_{yx} = \mathcal{C}e^2/\hbar$. Using the ab-initio values reported by [62] for the spin-orbit coupling strengths and onsite potential, we calculate the Berry curvature of the graphene supercell with an adatom. The SO coupling strengths are $\lambda_R = 1.14 \times 10^{-4}\ t$, $\Lambda_{PIA} = -2.66 \times 10^{-4}\ t$ and $\Lambda_I = -7.26 \times 10^{-5}\ t$. The magnitude of the exchange splitting at the nearest neighbors of the adatom site is set at 0.1 t throughout this calculation. A close-up of the band structure around the gap, and the Berry curvature profiles for these values are shown in panels (a) and (c) of Fig. (2.11), integration over the Brillouin zone yields $\mathcal{C} = 0$. The Berry curvature has different signs in opposite valleys and the Chern number around each valley is not an integer. This situation is similar to the Valley Hall effect in graphene in the presence of a sub lattice staggered potential, where valley currents are formed in the direction transverse to an applied in-plane electric field.

We will investigate the conditions for achieving a QAH state in this setting, we do this by checking the low-energy band structure and Berry curvature while increasing the Rashba parameter. A closing and reopening of the gap occurs at the topological phase transition from the Valley-Hall regime to the QAH state. We found this to occur for values of the Rashba parameter that are 10^4 times larger than the ab-initio values of [62] ($\lambda_R = 3.25$ t). Panel (b) in Fig. (2.11) shows the band structure for this situation of very large Rashba coupling, whereas panel (d) shows the profile of the Berry curvature in the same situation. The magnetization breaks both time reversal symmetry and sub lattice symmetry, since the adatoms are located only in one sublattice. We find the Berry curvature to be almost entirely concentrated around the K valley. We find $\mathcal{C} = 1$. We have investigated the band gaps at half-filling for lower adatom concentrations, and we have found the QAH phase to exist within a region of parameter space beyond physically realistic values [93]. Therefore, although theoretically the simultaneous existence of exchange and Rashba couplings in graphene might be able to create a quantum anomalous Hall state, within the realistic values such phase is not expected to be observed. Nevertheless, it is worth to note that the present model can be also applied to model further 2D honeycomb systems with stronger SOC, in which the topological state could be realized. In the following section, we will show how in these systems, where apart form the Rashba coupling there is a strong intrinsic SOC, the topological state can be easily realized.

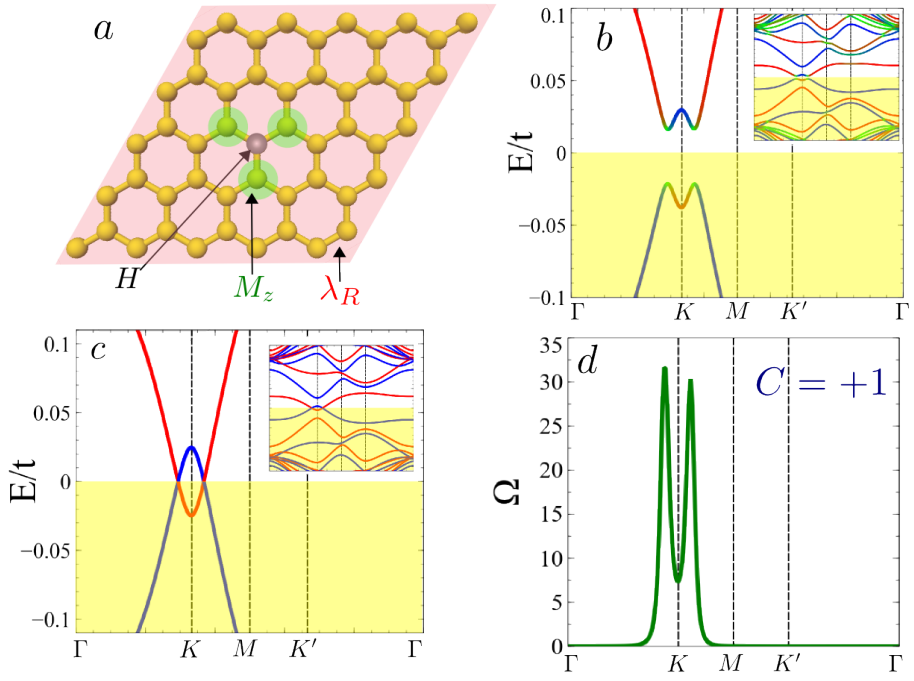

Figure 2.12: Scheme (a) of unit cell with vacancy induced local magnetism, and uniform Rashba induced by off-plane electric field. Band structure with vacancy, local magnetism, uniform intrinsic SOC with (b) and without Rashba (c). Berry curvature for (b), showing a Chern number $C = +1$. In comparison with Fig.(2.11), the anomalous Hall state (b) appears at arbitrary small Rashba field, provided intrinsic SOC closes the band gap (c).

2.4 Honeycomb lattice with adsorbates and uniform SOC

Moving away from graphene, we will explore this model in the regime of stronger SOC, which will be representative of heavier graphene-like honeycomb lattices. We have seen that the hydrogen-induced local Rashba is not strong enough to induce a topological phase transition to a QAH insulator, now we investigate the possibility of achieving such a state in a different setting: a supercell of a graphene like honeycomb crystal in which the intrinsic SO coupling cannot be neglected, in the presence of a substrate that induces a uniform Rashba effect, see panel (a) in Fig. (2.12). This model can be applied to a large family of systems such as silicene, germanene, stanene, hydrogenated bismuth, metal organic frameworks [95–100]. For the sake

of simplicity, we will spin split the flat band induced by the impurity by just applying a local exchange field to the first neighbors of the vacancy. We stress that this approach retains all the relevant features of the band structure. The spin-orbit coupling Hamiltonian in this model will be also introduced in a simpler form as:

$$\begin{aligned} H_{SO} &= \\ &+ \frac{2i}{3}\sum_{\langle i,j\rangle} c_{is}^{\dagger} c_{js'} \left[\lambda_R(\mathbf{s}\times \hat{d_{i,j}})_z\right]_{ss'} \\ &+ \frac{i}{3}\sum_{\langle\langle i,j\rangle\rangle} c_{is}^{\dagger} c_{js'} \left[\frac{\Lambda_I}{\sqrt{3}}\nu_{i,j}s_z\right]_{ss'} + H.c. \end{aligned} \tag{2.18}$$

where the SO hoppings are now uniformly distributed around the supercell and ν_{ij} is ± 1 depending on whether the second neighbor is reached clockwise or anticlockwise. The first term can be externally tuned by a perpendicular electric field, whereas the second is the intrinsic SO of the honeycomb lattice for that particular system.

Apart from this, the supercell Hamiltonian remains unchanged. Since the magnitude of the gap between the impurity bands decreases with adatom concentration, we can consider a regime in which the Kane-Mele intrinsic SO coupling is strong enough to close the exchange-splitted gap, as shown in panel (c) of Fig. (2.12). This situation can be observed with $\Lambda_I = 0.03$ t, $\lambda_R = 0.0$ t, and a exchange splitting of 0.25 t in the nearest-neighbors of the adatom. There is no gap around the K valley in this regime. Once the Rashba SO coupling is induced, a gap with topologically non-trivial properties appears as shown in panels (b) and (d) of Fig. (2.12), for the band structure and Berry curvature respectively, for a Rashba of $\lambda_R = 0.02$ t. Integration yields a Chern number $\mathcal{C} = 1$, signaling a QAH state with 1 edge state. The edge state can be observed in the energy spectrum of the hydrogenated nano ribbon, see panel (a) in Fig.(2.13) confirming the result obtained from the Berry curvature analysis . The edge state can also be observed from the k-resolved density of states at the zigzag edge of a semi-infinite plane, following the same calculation method as in [101], see panel (b) in Fig. (2.13)

A qualitative description of the properties of the system can be seen from the phase diagram in panel (a) of Fig. (2.14). For small values of the intrinsic and Rashba SO couplings the system is a trivial insulator. By increasing the values of either the Kane-Mele or Rashba the system turns into a metal, whereas the combination of higher intrinsic and Rashba couplings changes the system into a QAH insulator with one conducting edge state. The regime where the system is a trivial insulator, is characterized by Berry curvatures

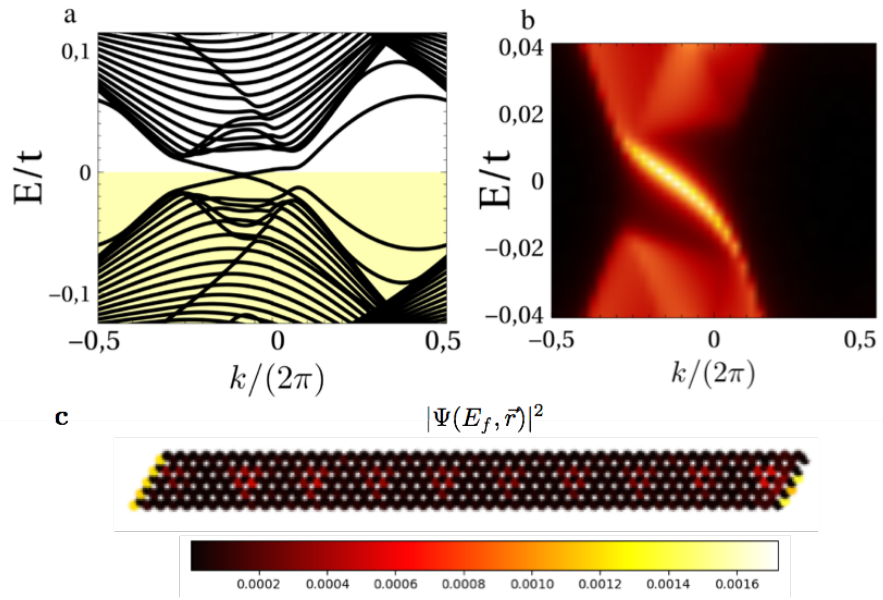

Figure 2.13: (a) Low-energy band structure of hydrogenated nano ribbon, the unit cell of 1,000 carbon atoms is constructed from the repetition of bulk cells. $\Lambda_I = 0.03t$, $\lambda_R = 0.02t$ and $\Delta = 0.25t$. (b) Density of states in the zigzag edge of a semi-infinite plane showing the existence of the edge state. (c) Distribution of the LDOS at the Fermi energy

of opposite signs in opposite valleys.

2.5 Hydrogenated graphene away from half filling

So far, we have considered the topological properties of the superlattice of adsorbates at half-filling. The adsorbates break sub lattice inversion symmetry, and in the trivial insulating case, they generate a Berry curvature distribution similar to that of graphene in the presence of a sublattice staggered potential, characterized by peaks of opposite signs at the two valleys. When the Fermi level is tuned to be at the bottom of the conduction band, which can be done by applying a gate voltage, the Berry curvature distribution continues to be asymmetric in opposite valleys, as shown in panels (c) and (d) of Fig. (2.14)., giving rise to a non-quantized Valley-Hall effect, i.e. skew-scattering for electrons in opposite valleys (see panel b), and thus a net valley current that travels in the bulk. The sign of the anomalous velocity can be switched by changing the sub lattice in which the adsorbates are placed.

This later effect is independent of any spin orbit coupling or magnetism,so it is expected to be observed in atomically engineered hydrogenated graphene. The assumptions for it to be observed is that, on one hand impurities have to be located in the same sublattice and on the other hand the concentration of adsorbates has to be such that the Bloch super cells have dimensions that preserve the Valley degree of freedom (i.e, $N \times N$ super cells where N is not an multiple of 3) [102] . It is important to note that random hydrogenation, even if clustering is avoided [103], will lead to hydrogen lying randomly in both sublattices, giving a vanishing net valley Hall effect. In comparison, if all the hydrogen atoms are located in the same sublattice, the net valley Hall current will be different from zero and strong non-local signal might be observed, very much like in gated bilayer graphene [104].

2.6 Hubbard mean-field

In this section we briefly present an extreme case to justify that the details of the local magnetic order are not critically important. In particular, we compare the result for a self-consistent Hubbard solution $H_Z = \sum_i U[\langle n_\uparrow \rangle n_\downarrow + \langle n_\downarrow \rangle n_\uparrow]$ to a situation where the exchange takes place only in the nearest neighbor atoms of the vacancy $H_Z = \sum_{NNv} JS_z$. The relative independence of the results of the details of the magnetism away from the vacancy can be rationalized as follows. The sublattice polarized zero energy state created by the hydrogen adatom is the one responsible for magnetism, and it is strongly localized close to the impurity. Even though this state is somewhat extended, a full selfconsistent solution gives a magnetism strongly localized in the proximity of the impurity. Therefore, a NN magnetism, localized in the three atoms yields a similar band structures compared with a Hubbard self-consistent calculation Fig. (2.15).

2.7 Magnetic anisotropy. Angle-dependent mean-field

Once a SOC term is included in the Hamiltonian, not all the directions for a magnetic solution are equivalent and the system is expected to develop a certain magnetic anisotropy. Nevertheless, for a single $S = 1/2$, no anisotropy is allowed in a single spin Hamiltonian due to $\sigma_x^2 = \sigma_y^2 = \sigma_z^2 = I$, and therefore a single vacancy is not expected to have magnetic anisotropy. In the case presented in this work, the periodic system has a an infinite number of $S = 1/2$ adsorbates and therefore certain anisotropy is allowed in the Hamiltonian. A perturbative argument in the SOC strength in the polarized vacancy bands yields a vanishing first order contribution, and therefore

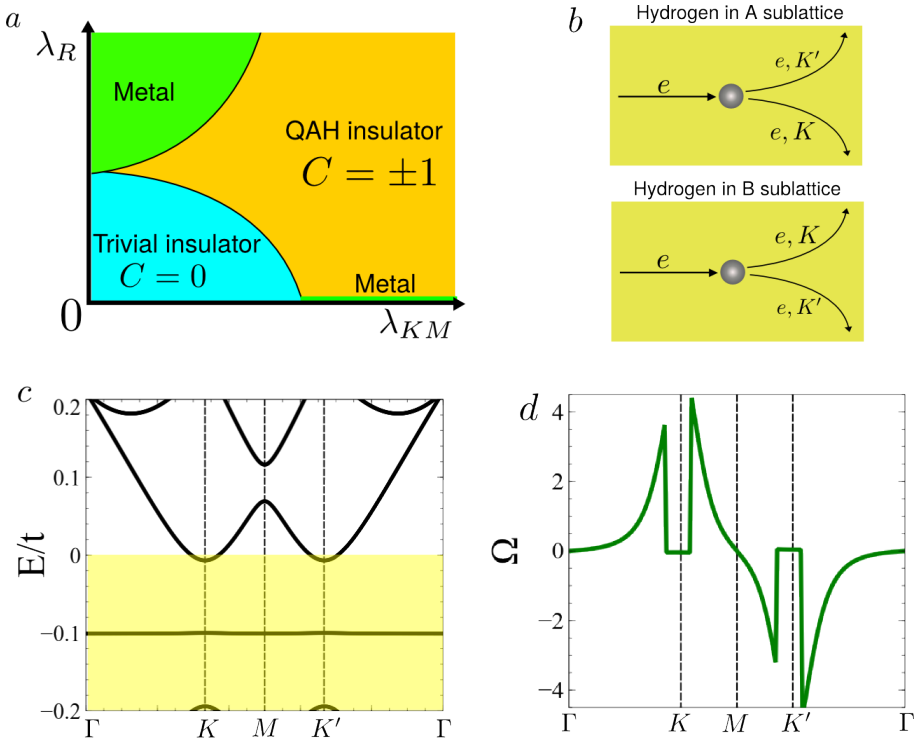

Figure 2.14: (a) Schematic phase diagram of the adatom in the supercell with intrinsic and Rashba SO couplings as parameters, the exact values of the SO couplings vary as a function of impurity concentration. (b) The Berry curvature is concentrated in one valley or the other depending on which sub lattice the impurities are located. Valley currents of opposite signs may be thus be engineered at will. (c) and (d) show respectively, the band structure and Berry curvature for slightly doped graphene. If the Fermi level now lies at the bottom of the conduction band the Berry curvature still has opposite signs at opposite valleys.

the first non-vanishing contribution is expected to be of the order

$$\Delta E_{anis} = \Lambda_{SOC}^2/t \tag{2.19}$$

where Λ_{SOC} is the SOC stregth, which will comprise both Rashba and Kane Mele-like SOC. Being a quadratic contribution it is expected to be rather small, as similar anisotropies in graphene-like systems [106]. In order to investigate the easy axis we use an angle-dependent collinear mean-field model; in this approach the spin-quantization axis is:

$$\Omega = (\sin\theta\cos\varphi, \sin\theta\sin\varphi, \cos\theta) \tag{2.20}$$

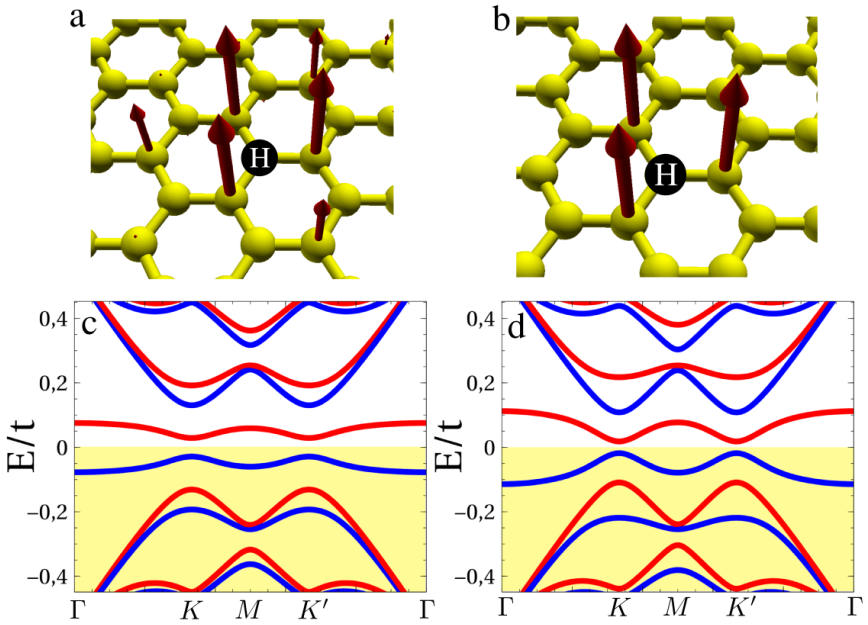

Figure 2.15: Comparison of the magnetic structures (a,b) and band structures (c,d) of a selfconsistent Hubbard calculation for vacancy (a,c), and only a NN magnetism (b,d). It is observed that band structures show very similar features. For (a,c) we took U=1.5t, whereas for (d,e) J=0.3t.

The number operators expressed in the rotated axis Ω are:

$$n_{i\uparrow\Omega} = \begin{pmatrix} \cos^2\frac{\theta}{2} & e^{-i\varphi}\sin\frac{\theta}{2}\cos\frac{\theta}{2} \\ e^{-i\varphi}\sin\frac{\theta}{2}\cos\frac{\theta}{2} & \sin^2\frac{\theta}{2} \end{pmatrix} \tag{2.21}$$

$$n_{i\downarrow\Omega} = \begin{pmatrix} \cos^2\frac{\theta}{2} & -e^{-i\varphi}\sin\frac{\theta}{2}\cos\frac{\theta}{2} \\ -e^{-i\varphi}\sin\frac{\theta}{2}\cos\frac{\theta}{2} & \sin^2\frac{\theta}{2} \end{pmatrix} \tag{2.22}$$

$$H_{MF} = U\sum_{i,s}\left[\langle n_{is\Omega}\rangle n_{is'\Omega} - \langle n_{i\downarrow\Omega}\rangle\langle n_{i\uparrow\Omega}\rangle\right] \tag{2.23}$$

With this approach the total energy can be calculated as a function of the angle θ. Importantly, the easy axis is found to be in-plane.

In the present case, the topological insulating phase requires a non-zero off-plane component. We show in Fig. (2.16) a system analogous to Fig. (2.12) , but now with the magnetization localized in-plane. In this case the total Chern number yields zero, so that this configuration is a trivial insulating state. In order to observe the QAH state, the off-plane moment must be stabilized, either by an off-plane magnetic field, or by exchange coupling to a magnetic substrate.

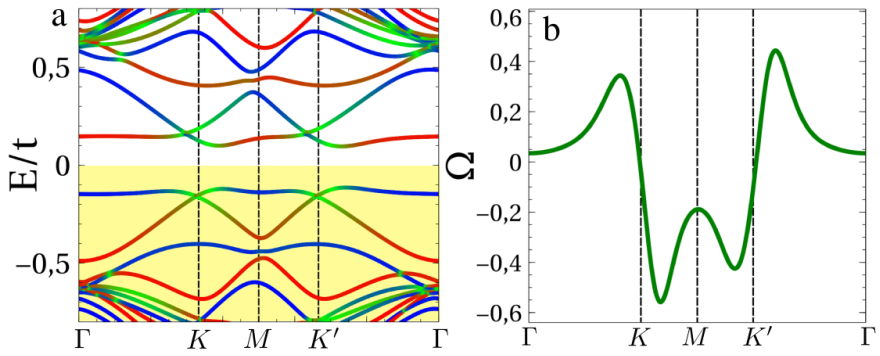

Figure 2.16: Panel (a) shows the band structure of the system for in-plane magnetization with $\lambda_R = 0.02$t; $\lambda_I = 0.03$t and a Zeeman splitting of $\Delta = 0.4$t in the nearest-neighbors of the adatom. Panel (b) shows the Berry curvature distribution yielding a Chern number $\mathcal{C} = 0$. In-plane magnetization yields a trivial insulating regime.

2.8 Summary and discussion

We have aimed at an understanding of the topological properties of honeycomb superlattices with adatoms in the dilute limit, by a Berry curvature analysis of the bulk gap at half filling. This gap is opened by the splitting of the impurity bands due to the exchange field. It is influenced by adatom concentration inasmuch as the vacancy state and the induced magnetic moment depend on the distance between adatoms [151]. We have found that within the range of realistic values for the SO couplings and onsite potential reported in [62] the sub lattice asymmetry induced by the adatom predominates over the exchange field and local SO couplings. The predominant phase is similar to the Valley Hall effect in gapped graphene, where electrons in opposite valleys acquire anomalous velocities transverse to an in-plane electric field in opposite directions. Finally, it is worth to remind that randomly distributed hydrogen adatoms would give rise to a net vanishing response, due to the statistical compensation between both sublattices.

We also extended our model in order to study the topological properties of arrays of adsorbates in honeycomb crystals in which the uniform intrinsic and Rashba SO couplings cannot be neglected, such as stanene, silicene or germanene. Starting from a situation in which the intrinsic SOC is strong enough to mix the exchange-splitted impurity bands, a situation that can be realized for low concentrations of impurities, we have found that the

Rashba parameter is capable of opening a gap with non-trivial topological properties, effectively turning the system into a QAH insulator. Finally we also considered the situation in which the Fermi level lies inside the bottom of the conduction band, we have found a Berry curvature distribution of peaks of opposite signs in the two valleys, marking the the presence of bulk valley currents in a direction transverse to an applied electric field.

Chapter 3

Modulation of Kekulé adatom ordering due to strain in graphene

Much of the rich physics of graphene stems from the peculiarities of its intrinsic electronic structure, such as its gapless Dirac spectrum, the chirality of its carriers, or the emergence of pseudogauge fields as a result of inhomogeneous strains [114–116] . These are all intra-valley properties, defined independently within valleys $\mathbf{K}$ and $\mathbf{K}'$. They are responsible for e.g. graphenes high mobilities [117], Klein tunneling [118], the valley-Hall effect [119] or the emergence of topologically protected boundary states in bilayers [120, 195]. They remain robust as long as valley symmetry is preserved, i.e. as long as any perturbation or disorder present in the sample acts symmetrically on the two sublattices of the crystal. Atomic-like defects are one important type of perturbation that does not in general preserve valley symmetry, and allows for scattering events with an intervalley $\Delta\mathbf{K} = \mathbf{K} - \mathbf{K}'$ momentum transfer ($\hbar = 1$) [121].

Intervalley scattering may be important at the edges of a generic graphene flake [122, 123], at substitutional dopants [124–126], or at certain adatoms [127] that adsorb to graphene in a top configuration (i.e. adsorbed atop individual carbon atoms), such as Fluor [128] or Hydrogen [91], thereby breaking sublattice symmetry. Despite destroying the chiral nature of carriers in graphene, intervalley scattering is also fundamentally interesting in its own right [129], and can actually become a powerful tool, particularly for graphene functionalization. It is crucial for the engineering of enhanced spin-orbit couplings and finite bandgaps in graphene via decoration with adatoms [130–133], by the effect of a crystalline substrate [134–136], or through electron-phonon interaction [137].

Here, we will focus on another effect of intervalley scattering, the unique ordering mechanism of top adatoms [131] and similar atomic-like defects [138, 139] in graphene. Adatom-ordering results from the electron-mediated interactions between defects as graphene quasiparticles scatter between them [140–142]. Scattering at adatoms locally modifies the electronic density of states in graphene, which gives rise to Friedel oscillations [124, 143] (see Appendix B for a detailed discussion) and to a change in the total electronic energy that depends on the distance between adatoms. This effect has been shown to be the dominant contribution in the interaction between graphene adatoms [144]. It leads to the self-organization of atomic defects and adatoms at different levels, including sublattice ordering [132,142], Kekulé ordering [141] and spatial clustering [140]. Kekulé ordering, recently demonstrated in experiment [139], is probably the most striking of these.

Via an approach that combines ab initio density functional theory, and a tight-binding approach, the authors of [144] found that the interaction between top-adatoms in graphene has two regimes of radial dependence: a short-distance regime in which the interaction decays as $1/r$, and a long-distance regime in which the interaction decays as $1/r^3$. In the short-distance regime, the interaction is attractive when adatoms lie in opposite sublattices (AB configuration) and repulsive when in the same sublattice (AA configuration), whereas the situation is reversed in the long-distance regime. The transition between the short- and long- distance regimes occurs abruptly at a critical distance that depends heavily on the strength of the adatom onsite potential (ϵ_0) and the adatom-graphene coupling t'. Importantly, the interaction potential oscillates according to a Kekulé periodicity $\cos^2[\frac{1}{2}(\mathbf{K}-\mathbf{K}').\mathbf{r}]$. The RKKY interaction between magnetic adatoms has a similar Kekulé oscillatory behavior. Furthermore it is ferromagnetic when the impurities are in AA-configuration, and antiferromagnetic when in AB-configuration, a result that has been confirmed for the case of hydrogen adatoms by using first-principle calculations in [91]. By contrast, the interaction potential between plaquette-type impurities (i.e. hollow-adatoms positioned at the center of a graphene hexagon) , which do not produce intervalley-scattering, shows a similar $1/r^3$ asymptotical dependence but without the Kekulé $\cos^2(\frac{1}{2}\Delta\mathbf{K}.\mathbf{r})$ oscillations. In Appendix B we will address in more detail the intervalley scattering and Friedel oscillations produced by a top-adatom, and the experimental evidence of the Kekulé adatom-ordering in graphene will be discussed in section 3.1 .

In this chapter, we show that electron-mediated Kekulé ordering is extremely sensitive to elastic strains in the underlying graphene. The connection arises from the effect of strain-induced pseudogauge fields on intervalley scattering, and could provide a sensitive way to measure strains through

adatom distributions, or conversely to control Kekulé ordering of adatoms through strain engineering. The chapter is structured as follows: in section (3.1) we discuss an experiment by Gutierrez et al. [139] where they found evidence of Kekulé ordering of impurities in graphene; in section (3.2) we explain our model for the calculation of the interaction energy between adsorbates, and we apply it to the case of top-adatoms on unstrained graphene confirming the findings of previous literature; in section (3.3) we apply our model to the case of top-adatoms in graphene under elastic strain, in section (3.4) we discuss the case of strongly-coupled adatoms, in section (3.5) we include in our discussion the effects of adatom magnetization (here modelled by a mean-fied Hubbard Hamiltonian), in section (3.6) we explain how our model yields the same $1/r^3$ asymptotic dependence in a limit without dissipation, and finally in section (3.7) we discuss other kinds of adsorbates: adatoms in the hollow position as well as benzene molecules, and study their interaction potential.

3.1 Gutierrez et al. experiment. Hidden Kekulé order in graphene

The Kekulé distortion in graphene is a phase characterized by a periodic altering of the strength of 1/3 of the C-C bonds, schematically depicted in Fig. (3.1 a) where bonds in black (blue) have a hopping strength of t (t'); this distortion triples the unit cell, the original lattice vector of the honeycomb lattice is shown in red in Fig. (3.1 a), whereas the lattice vectors of the Kekulé distorted lattice are depicted as yellow. This bond-distortion opens a gap at the Dirac points (citations needed).

A path to engineering the Kekulé phase in graphene, is by adsorption of ad-atoms in top-positions of graphene. An impurity induces Friedel oscillations that have the same wavelength as the periodicity of the Kekulé superlattice (see Appendix B). Adatoms in graphene, upon cooling, are expected to arrange themselves in such a way that they lie in the same Kekulé sublattice, Fig. (3.1 d), yielding an ordered state in which their Friedel oscillations are amplified by constructive interference. This causes displacements in the carbon atom positions, generating a Kekulé distorted graphene lattice. Thus, within this proposal,the Kekulé distorted phase should manifest in the positions of the impurities, see Fig. (3.3), and in the fact that STM-imaging should show and additional periodicity of the tripled-unit cell.

The experiment carried out by [139], performed STM-imaging of epitaxial graphene grown on a copper substrate, the geometry is shown in Fig. (3.2 a). STM images reveal the presence of atomic features, see Fig. (3.3 a). The atomic features show the "Y" shape characteristic of top-adsorbates,

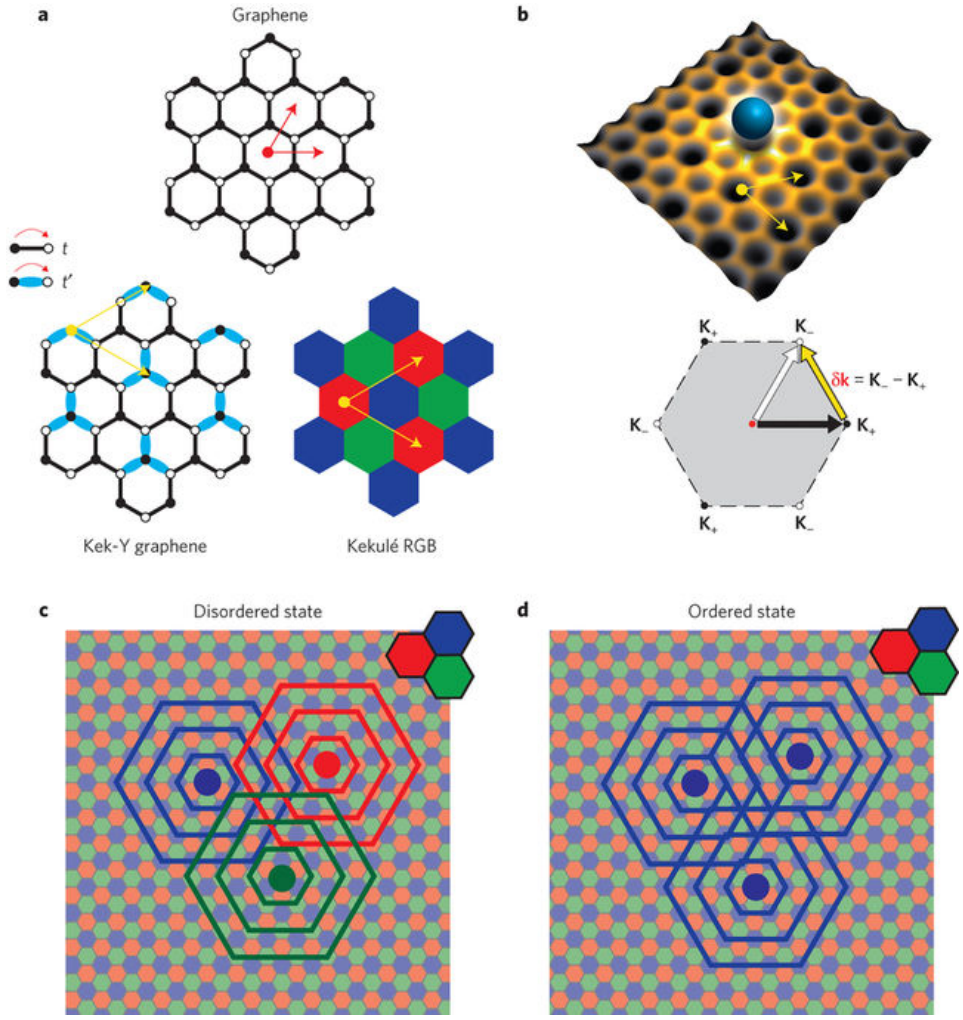

Figure 3.1: Adatom-induced Kekulé distortion (KD) in graphene. a) Real-space schematic of pristine graphene (top) and KD graphene (bottom left). In the KD phase, a third of the bonds in graphene (shown here in blue) are differente owing to the two hopping energies t,t_0. The KD phase of graphene can be represented by making a three-colour mosaic tiling of the pristine graphene lattice, as shown in the bottom right. b) Illustration of how an adatom adsorbed onto graphene creates Friedel oscillations with the KD wavevector in its immediate vicinity. c),d), Illustrations of the disordered and hidden Kekulé ordered (HKO) states of adatoms, respectively. Adapted with permission from [139]

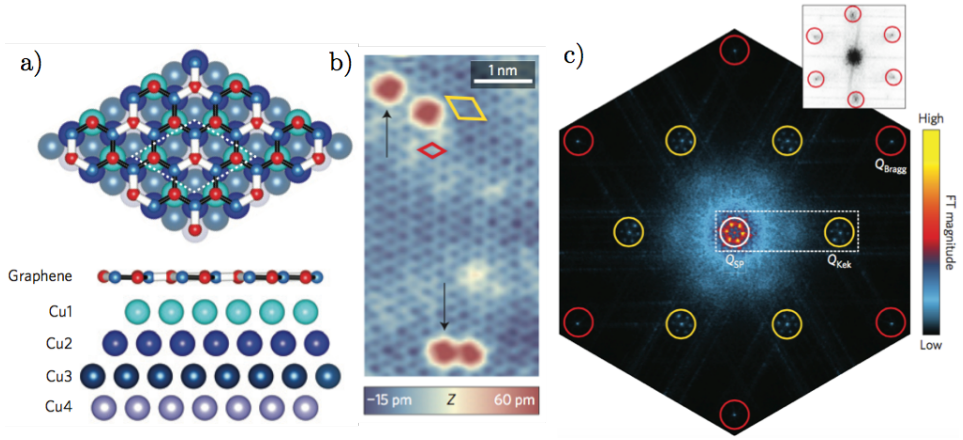

Figure 3.2: a) Relaxed DFT structural model of graphene-Cu(111). C-C bonds (white) contr act above Cu1 vacancies. b) Atomically resolved STM topograph (V_b = 100 mV, I = 120 pA) showing the graphene honeycomb lattice (red diamond) and KD supercell (yellow diamond). The topography also shows several bright spots (indicated by black arrows). c) Fourier transform (FT) of a large-area atomically resolved topography (V_b = 5 mV, I = 120 pA). The six red circles are at the graphene Bragg peak locations, and the six yellow circles are at the wavelength of the KD. The inset shows a corresponding FT from graphene grown on a rare patch of amorphous copper foil. This FT shows the graphene Bragg peaks (red circles) but no KD. Adapted with permission from [139]

but their apparent height is much smaller than typical for an adatom, the atomic feature is actually caused by vacancies in the Cu1 layer of copper that lies immediately beneath graphene. As expected from theory, the ghost adatoms tend to cluster in the same Kekulé sublattice, even in very large areas, see Fig. (3.3 d). STM topography shows patches with larger honeycomb patterns with a darker depression at every other graphene hollow position, thus forming a triple unit cell (yellow rhombus in Fig. 3.2 b, the red rhombus shows the graphene unit cell). The Fourier transform of STM-topographic images show three distinct periodicities, there are six outer peaks (surrounded by red circles) located at the wavelength of the reciprocal lattice of graphene; but additional peaks (surrounded by yellow circles) arise at the wavelength of the Kekulé tripled unit cell, which is the same wavelength of the Friedel oscillations of a top-impurity or adatom, the "yellow" peaks are absent in pristine undistorted graphene (see inset in Fig. 3.2 c) and constitute the main signature of the Kekulé distortion of graphene.

3.2 Adsorbate-adsorbate interactions in graphene

3.2.1 Single-impurity Anderson model

The Anderson impurity model is used to describe magnetic impurities adsorbed in a metallic host [110]. We will use it here to obtain the mean-field Hubbard Hamiltonian of a single molecule adsorbed on a graphene lattice. Our model starts from a frequency dependent Hamiltonian for the molecule:

$$H_{eff}^{mol}(\omega) = H_0^{mol} + U\sum_i \langle n_{i\uparrow}\rangle n_{i\downarrow} + \langle n_{i\downarrow}\rangle n_{i\uparrow} + \Sigma^{gr}(\omega) \tag{3.1}$$

where $H_0^{mol} + U\sum_i \langle n_{i\uparrow}\rangle n_{i\downarrow} + \langle n_{i\downarrow}\rangle n_{i\uparrow}$ is the Hamiltonian of the isolated molecule, and $\Sigma^{gr}(\omega) = -t'^{\dagger} G_0^{gr}(\omega) t'$ is the self-energy of the graphene bath on the molecule; the matrix t' is the hopping between the molecule and graphene and $G_0^{gr}(\omega)$ is the pristine Green's function of graphene. The mean values of the number operators for each site i and each spin variety σ are calculated from the effective Hamiltonian of the molecule via the integral:

$$\langle n_{i,\sigma}\rangle = \int_{-\infty}^{\epsilon_f} \rho_{i\sigma,i\sigma}^{mol}(\omega)d\omega = -\frac{1}{\pi}\Im \int_{-\infty}^{\epsilon_f} \left[\omega - H_{eff}^{mol}(\omega)\right]^{-1}_{i\sigma,i\sigma} d\omega \tag{3.2}$$

Once we have obtained the mean-field Hamiltonian of the adsorbate, we now obtain the Green's function of graphene in the presence of the adsorbate. This can be obtained via Dyson's equation:

$$G^{gr} = G_0^{gr} + G_0^{gr}\Sigma^m G^{gr} = G_0^{gr} + G_0^{gr}\Sigma^m \left(G_0^{gr} + G_0^{gr}\Sigma^m G_0^{gr} + ...\right) \tag{3.3}$$

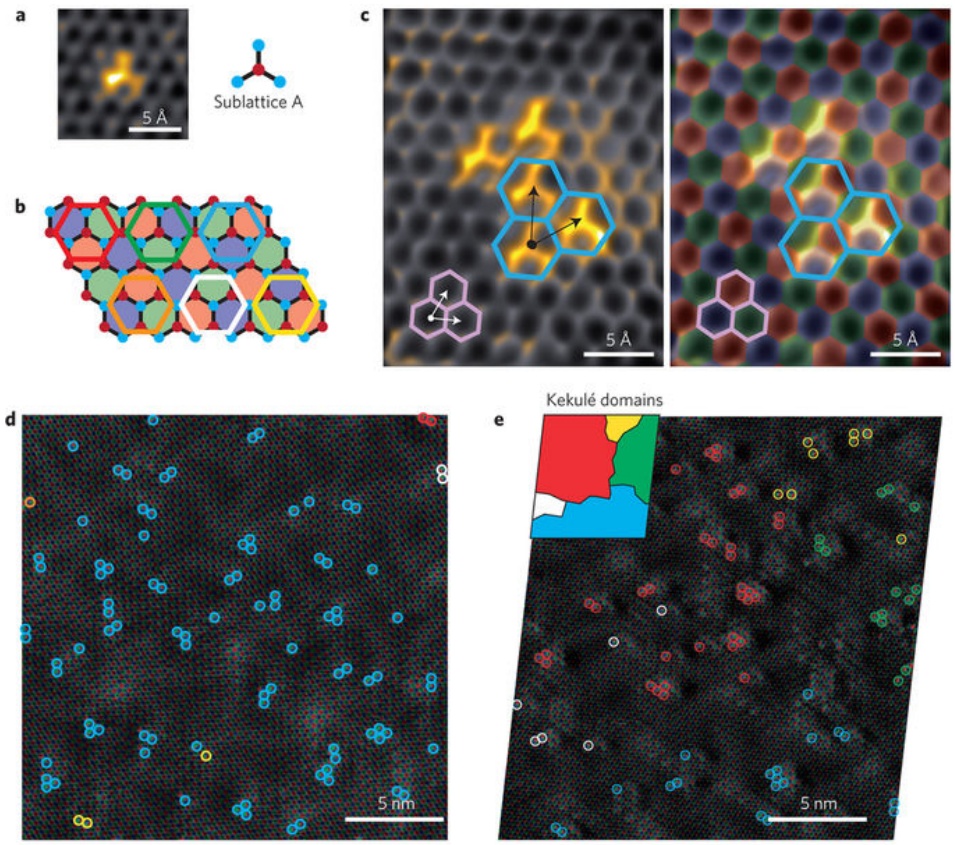

Figure 3.3: a, Close-up topograph around a single atomic feature (AF) ($V_b = -5$mV, $I = 120$pA) showing the atomic structure of the AF. We note that this detailed "Y" shape is more apparent at low biases, $|V_b| \leq 10$mV. b) Graphene can be considered as three inter-penetrating Kekulé mosaic lattices that can be represented by the three colours as shown. The AF's can be classified by six colours, for the three phases of KD and two sublattices. Hidden Kekulé ordering (HKO) of the AF's corresponds to the selection of one colour of the AF's in a given topograph. c) Three-dimensional STM topograph of several AF's showing the presence of local HKO in the AF's ($V_b = -5$mV, $I = 120$pA). The image on the right is overlayed with the three-colour representation of the graphene lattice. d) Large-scale topograph showing several AF's that are colour-coded as in b ($V_b = 80$mV, $I = 650$pA). The image shows that the AF's are almost completely ordered over large areas onto a single Kekulé lattice, evidence of the HKO state. e) Large-scale topograph showing the presence of several Kekulé domain boundaries in the graphene. We note that the graphene sheet itself is perfectly continuous across the area and has no defects ($V_b = -5$mV, $I = 120$pA). Adapted with permission from [139]

where G_0^{gr} is the Green function of pristine graphene and Σ^m is the self-energy term in graphene due to the adsorbed molecule:

$$\Sigma^m(\omega) = -t'^{\dagger}\left[(\omega + i\eta) - H_0^{mol} - H_{mf}^{mol}\right]^{-1} t' \tag{3.4}$$

where $H_{mf}^{mol} = U\sum_i \langle n_{i\uparrow}\rangle n_{i\downarrow} + \langle n_{i\downarrow}\rangle n_{i\uparrow}$ is the part of the Hamiltonian that accounts for the electron-electron repulsion within the mean-field approximation; this equation can be rearranged as :

$$G^{gr} = G_0^{gr} + G_0^{gr}\left(\Sigma^m + \Sigma^m G_0^{gr}\Sigma^m + ...\right)G_0^{gr} = G_0^{gr} + G_0^{gr}TG_0^{gr} \tag{3.5}$$

where the T matrix is given by the expansion :

$$T = \Sigma^m + \Sigma^m G_0^{gr}\Sigma^m + \Sigma^m G_0^{gr}\Sigma^m G_0^{gr}\Sigma^m + ... \tag{3.6}$$

$$T = \Sigma^m + \Sigma^m\left(G_0^{gr} + G_0^{gr}\Sigma^m G_0^{gr} + G_0^{gr}\Sigma^m G_0^{gr}\Sigma^m G_0^{gr} + ...\right)\Sigma^m \tag{3.7}$$

we will now prove that the expansion within parenthesis can be written as $\left((G_0^{gr})^{-1} - \Sigma^m\right)$. On the one hand we have that:

$$(1 - \Sigma^m G_0^{gr})^{-1} = \left[\left((G_0^{gr})^{-1} - \Sigma^m\right)G_0^{gr}\right]^{-1} = (G_0^{gr})^{-1}\left[(G_0^{gr})^{-1} - \Sigma^m\right]^{-1} \tag{3.8}$$

$$(G_0^{gr})^{-1}\left[(G_0^{gr})^{-1} - \Sigma^m\right]^{-1} = 1 + \Sigma^m G_0^{gr} + \Sigma^m G_0^{gr}\Sigma m G_0^{gr} + ... \tag{3.9}$$

$$\left[(G_0^{gr})^{-1} - \Sigma^m\right]^{-1} = G_0^{gr} + G_0^{gr}\Sigma^m G_0^{gr} + G_0^{gr}\Sigma^m G_0^{gr}\Sigma^m G_0^{gr} + ... \tag{3.10}$$

Therefore, one can write the T matrix of graphene in the presence of the adsorbed molecule as:

$$T(\omega) = \Sigma^m + \Sigma^m\left[(G_0^{gr})^{-1} - \Sigma^m\right]^{-1}\Sigma^m \tag{3.11}$$

Once the T matrix is obtained, we have solved the problem of finding out the effect of the adsorbate on graphene. In specific, the magnetic moment in each graphene site, which comes from the difference in density of states for each spin variety can be derived from the graphene Green function as:

$$M_z(\mathbf{r_i}) = \langle n_{i\uparrow}\rangle - \langle n_{i\downarrow}\rangle = \int_{-\infty}^{\epsilon_f} d\omega\left[\rho_{i\uparrow}^{gr}(\omega) - \rho_{i\downarrow}^{gr}(\omega)\right] \tag{3.12}$$

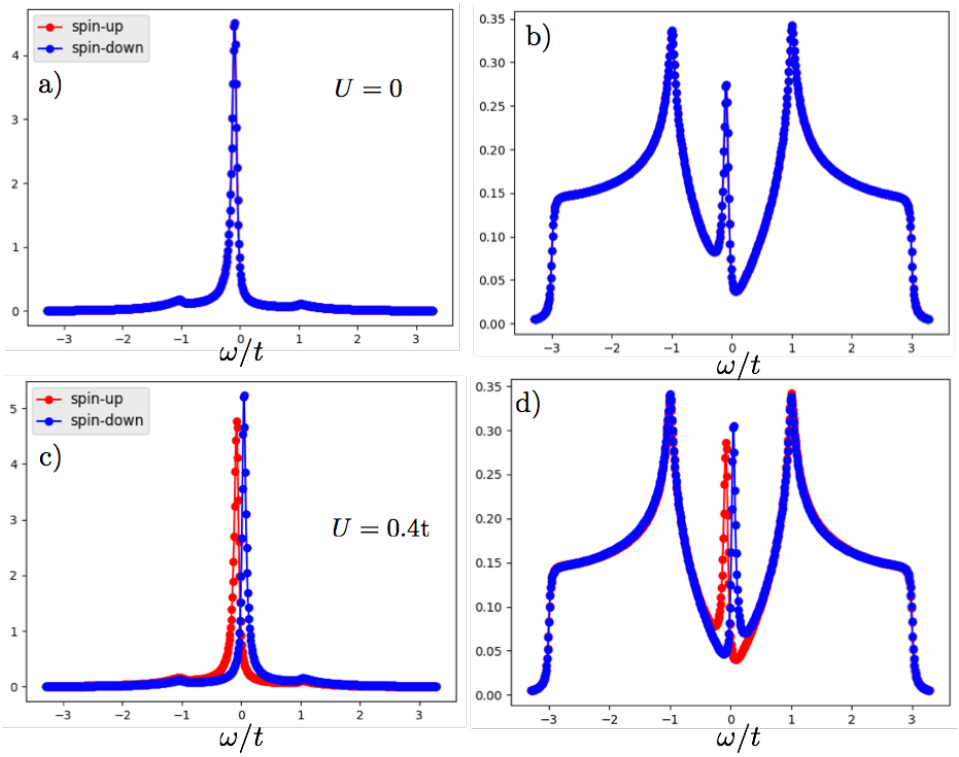

Figure 3.4: DOS of an adatom and LDOS in the nearest neighbor of the adsorbed site in graphene for $U = 0$ (a,b) and $U = 0.4$ t (c,d). $\epsilon_0 = -0.15$t and $t' = -0.7$t.

$$M_z(\mathbf{r_i}) = -\frac{1}{\pi}\int_{-\infty}^{\epsilon_f} d\omega \Im\left[G^{gr}_{i\uparrow,i\uparrow}(\omega) - G^{gr}_{i\downarrow,i\downarrow}(\omega)\right] \tag{3.13}$$

As an example, we consider an adatom adsorbed in the top position of a graphene site. The top-adatom is represented as a single orbital with onsite energy $\epsilon_H = -0.15$ t that is slightly lower than the Fermi level of graphene set at half-filling; the hopping between the hydrogen and the carbon site below is $t' = -0.7\ t$. Panels (a,b) of Fig. (3.4) show the DOS at the adatom and the LDOS in the nearest-neighbor of the adatom for $U = 0$. For the interacting case, with $U = 0.4$t, panels (c,d) of Fig. (3.4) show the spin-splitting of the peaks near the Fermi level.

3.2.2 Two-impurity Anderson model

Now, we consider the problem of adsorption of two molecules M_1 and M_2 separated by a vector $\mathbf{R_{12}} = \mathbf{r_2} - \mathbf{r_1}$. We are interested in exploring not only the magnetism arising in both graphene and the molecules but also, we want

to explore the dependence of the total energy of the system as a function of $\mathbf{R_{12}}$. In this model, the self-consistent calculation of the Hamiltonian must be carried out simultaneously for the two adsorbates. The effective mean-field Hamiltonian in M_2 is given by:

$$H_{eff}^{m2}(\omega) = H_0^{m2} + U\sum_{i,\sigma}\langle n_{i\sigma}^{m2}\rangle n_{i\sigma'}^{m2} + \Sigma^{gr,m1}(\omega) \tag{3.14}$$

where the self-energy $\Sigma^{gr,m1}(\omega) = -t'^{\dagger}G_{m1}^{gr}(r_2,r_2)t'$. Notice that the graphene Green function in the self-energy term is not the Green function of pristine graphene, but the Green function of pristine graphene $G_0^{gr}(r_2,r_2)$ plus the effect of the neighboring molecule M_1 contained in the T-matrix $T_1(\omega)$, the self-energy thus represents the influence of graphene and M_1 on M_2:

$$G_{m_1}^{gr}(r_2,r_2) = G_0^{gr}(r_2,r_2) + G_0^{gr}(r_2,r_1)T_1(\omega)G_0^{gr}(r_1,r_2) \tag{3.15}$$

where $T_1(\omega) = \Sigma^{m1}\left[1 - G_0^{gr}(r_1,r_1)\Sigma^{m1}\right]^{-1}$ and the self-energy of M_1 on graphene is :

$$\Sigma^{m1}(\omega) = -t'^{\dagger}\left[(\omega+i\eta) - H_0^{m1} - U\sum_{i,\sigma}\langle n_{i\sigma}^{m1}\rangle n_{i\sigma'}^{m1}\right]^{-1} t' \tag{3.16}$$

with this Green function the mean-values of the number operators in the sites of M_2 can be calculated :

$$\langle n_{i\sigma}^{m2}\rangle = -\frac{1}{\pi}\Im\int_{-\infty}^{\epsilon_f} d\omega\left[(\omega+i\eta) - H_0^{m_2} - U\sum_{i,\sigma}\langle n_{i\sigma}^{m_2}\rangle n_{i\sigma'}^{m_2} - \Sigma^{gr,m_1}(\omega)\right]^{-1}_{i\sigma,i\sigma} \tag{3.17}$$

The analogous expressions for molecule M_1 are :

$$H_{eff}^{m_1}(\omega) = H_0^{m_1} + U\sum_{i,\sigma}\langle n_{i\sigma}^{m_1}\rangle n_{i\sigma'}^{m_1} + \Sigma^{gr,m_2}(\omega) \tag{3.18}$$

$$\Sigma^{gr,m_2} = -t'^{\dagger}G^{gr,m_2}(r_1,r_1)t' \tag{3.19}$$

$$G^{gr,m_2}(r_1,r_1) = G_0^{gr}(r_1,r_1) + G_0^{gr}(r_1,r_2)T_2(\omega)G_0^{gr}(r_2,r_1) \tag{3.20}$$

$$T_2(\omega) = \Sigma^{m2}\left[1 - G_0^{gr}(r_1,r_1)\Sigma^{m2}\right]^{-1} \tag{3.21}$$

$$\langle n_{i\sigma}^{m_1}\rangle = -\frac{1}{\pi}\Im\int_{-\infty}^{\epsilon_f} d\omega\left[(\omega+i\eta) - H_0^{m_1} - U\sum_{i,\sigma}\langle n_{i\sigma}^{m_1}\rangle n_{i\sigma'}^{m_1} - \Sigma^{gr,m_2}(\omega)\right]^{-1}_{i\sigma,i\sigma} \tag{3.22}$$

After convergence of the mean-field Hamiltonian, we can obtain the Green's function of graphene under adsorption of two molecules as:

$$G^{gr}_{m_1,m_2}(\omega) = G^{gr}_0(\omega) + G^{gr}_0(\omega) T_{m_1,m_2}(\omega) G^{gr}_0(\omega) \tag{3.23}$$

From now on, to simplify our notation $G^{gr}(\omega)$ will be understood to be the Green function of graphene in the presence of M_1 and M_2.

$$G^{gr}_0(\omega) = \begin{pmatrix} G^{gr}_0(r_1,r_1) & G^{gr}_0(r_1,r_2) \\ G^{gr}_0(r_2,r_1) & G^{gr}_0(r_2,r_2) \end{pmatrix}$$

$$\Sigma_{m_1,m_2}(\omega) = \begin{pmatrix} \Sigma^{m1} & 0 \\ 0 & \Sigma^{m2} \end{pmatrix}$$

$\Sigma_{m_1,m_2}(\omega)$ is the self-energy in graphene due to the presence of molecules M_1 and M_2 analogous to (3.4) in the single-adsorbate case, and $T_{m_1,m_2}(\omega) = \Sigma_{m_1,m_2}\left[1 - G^{gr}_0(\omega)\Sigma_{m_1,m_2}\right]^{-1}$ is the T-matrix of the two molecules. With the Green functions of graphene ($G^{gr}(\omega)$) and M_1, M_2, one can also calculate the total energy of the system :

$$E_T = -\frac{1}{\pi}\Im \int_{-\infty}^{\epsilon_f} \omega Tr\left[G^{gr}(\omega) + G^{m_1}(\omega) + G^{m_2}(\omega)\right] d\omega \tag{3.24}$$

The contributions of M_1 and M_2 to the total energy are easy to compute from:

$$G^{m_{1,2}} = \left[(\omega + i\eta) - H_0^{m_{1,2}} - U\sum_{i,\sigma}\langle n^{m_{1,2}}_{i,\sigma}\rangle n^{m_{1,2}}_{i,\sigma'} - t'^{\dagger} G^{gr}_{m_{2,1}} t'\right]^{-1} \tag{3.25}$$

the total sum is over the the number of orbitals of each adsorbate. The contribution from graphene is less trivial to calculate, given that the trace of $G^{gr}(\omega)$ is a summation over an infinite number of atomic sites of graphene. We only need to consider the diagonal terms $G^{gr}_{ii}(\omega) = G^{gr}_{0,ii} + G^{gr}_{0,ij} T_{j,j'}(\omega) G^{gr}_{0,j'i}$. The first term in the right hand side corresponds to pristine graphene and it is irrelevant for our purposes since it is independent of the presence of the adsorbates, and we will neglect it henceforth. In order to work around the difficulty of summing over all graphene sites, we expand the pristine graphene terms as a sum over k points in the Brillouin zone:

$$G^{gr}_{0,ij} = \frac{1}{N_k}\sum_{\mathbf{k}} \frac{e^{i\mathbf{k}.(\mathbf{r}_i - \mathbf{r}_j)}}{(\omega + i\eta) - H^{gr}_0(\mathbf{k})} \tag{3.26}$$

using this expansion, the trace of the Green's function can be written as:

$$\sum_i G^{gr}_{ii} = \frac{1}{{N_k}^2}\sum_{\mathbf{k},\mathbf{k}'}\sum_{j,j',i} e^{i(\mathbf{k}-\mathbf{k}').\mathbf{r}_i} e^{-i\mathbf{k}.\mathbf{r}_j} e^{-i\mathbf{k}'.\mathbf{r}_{j'}} Tr\left[\frac{1}{\omega - H^{gr}(\mathbf{k})} T_{jj'}(\omega) \frac{1}{\omega - H^{gr}(\mathbf{k})}\right] \tag{3.27}$$

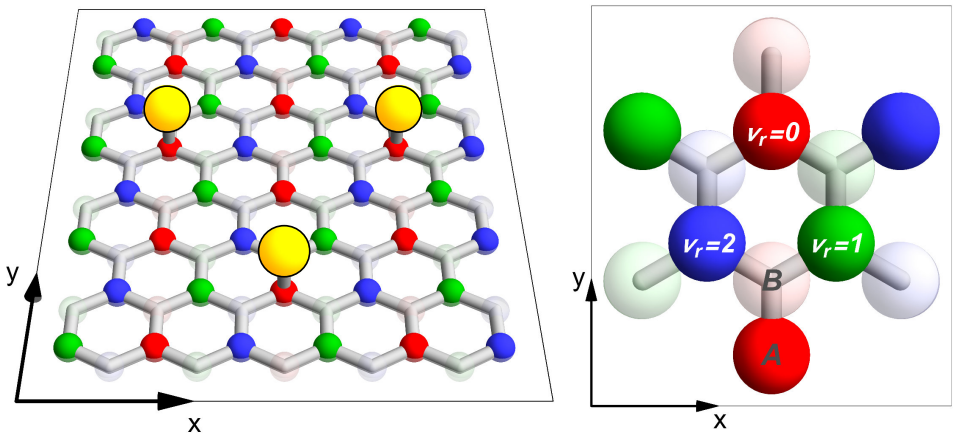

Figure 3.5: Sketch of the Kekulé index $\nu_{\mathbf{r}} = 0, 1, 2$ (red,greeen,blue) on each sublattice of graphene. Hidden Kekulé ordering of top-adatoms (yellow balls in panel a) corresponds to adsorption on sites with equal $\nu_{\mathbf{r}}$ as a result of adatom interaction mediated by carriers in graphene that undergo intervalley scattering.

given that $\sum_i e^{i(\mathbf{k}-\mathbf{k}').\mathbf{r_i}} = N_k\delta(\mathbf{k}-\mathbf{k}')$, this expression can be simplified further:

$$\sum_i G^{gr}_{ii} = \frac{1}{N_k}\sum_{\mathbf{k}} Tr\left[\frac{1}{\omega - H^{gr}(\mathbf{k})}\sum_{j,j'} e^{i\mathbf{k}.(\mathbf{r}_j-\mathbf{r}'_j)}T_{jj'}(\omega)\frac{1}{\omega - H^{gr}(\mathbf{k})}\right] \tag{3.28}$$

the summation over indices j, j' in the right hand side of (3.28) is carried out over atomic orbitals of the adsorbate, instead of the sum over graphene sites with the i index. Thus, in (3.28) we have transformed a sum over an infinite number of graphene sites into a sum over a finite number of adatom positions.

3.2.3 Top adatoms

We now apply the model described in the previous section to the case of two identical adatoms in top-positions in unstrained graphene. Consider a top adatom on sublattice σ =A,B of a graphene unit cell centered at $\mathbf{r} = n_1\mathbf{a_1} + n_2\mathbf{a_2}$ ($\mathbf{a_i}$ are graphene's lattice vectors with $|\mathbf{a_i}| = a_0$ and $|\Delta\mathbf{K}| = 8\pi/\sqrt{3}a_0$). One may classify such adatom by the sublattice σ and an integer Kekulé index $\nu_{\mathbf{r}}$, such that $\Delta\mathbf{K}\cdot\mathbf{r} = 2\pi\nu_{\mathbf{r}}/3 + 2\pi n$ for some integer n, i.e.

$$\nu_r = \frac{\Delta\mathbf{K}\cdot\mathbf{r}}{2\pi/3} \tag{3.29}$$

These three possibilities are color-coded as "red", "green" and "blue" here, and are shown in Fig. 3.5 for one of the graphene sublattices. Hidden Kekulé order consists of collections of top adatoms or atomic defects which minimise their quasiparticle-mediated interaction energy by adopting the same values of $\nu_{\mathbf{r}}$, and (possibly) the same value of σ, see yellow adatoms in Fig. 3.5. We now describe the mechanism that gives rise to Kekulé ordering, and in the next section we analyse how it is affected by the presence of elastic strains.

In Fig. (3.6) we show plots of the interaction energy between the adatoms along the x axis. The magnitude and even the sign of the interaction strongly depends on the t'/t ratio, i.e. on how strongly the adatoms couple to graphene. Two regimes can be easily distinguished, one for $t'/t < 1.5$ in which the interaction is attractive for adatoms in the same sublattice (we will call this "weak coupling regime"), and another for $t'/t \geq 1.5$ in which the opposite-sublattice configuration is energetically favorable ("strong-coupling regime"). The weak-coupling regime has been observed experimentally at room temperature for a specific type of vacancy [139].

Fig. (3.7) shows the density of states of the adatom (panel a) and the local density of states in the nearest-neighbor graphene site of the adatom in the weak-coupling regime ($\epsilon_0 = -0.15$t and $t' = -0.7$t) in panel b).The LDOS at the nearest-neighbor graphene site acquires a peak near the Fermi level due to the coupled adatom. The spatial map of the interaction energy $U_{AA}(\mathbf{r}_{12})$ between adsorbates in the same sublattice can be seen in Fig. (3.8), each point is colored according to its Kekulé index $\nu_{\mathbf{r}}$, the size of each point is proportional to the magnitude of the attractive potential, therefore the most visible color shows the most favored Kekulé component. We can see that the Kekulé modulation is given by:

$$U_{AA}(\mathbf{r}) = v_{AA}(r)\cos^2\left(\frac{\mathbf{\Delta K}}{2}\cdot\mathbf{r}\right) \tag{3.30}$$

Panel b) of Fig. (3.8) shows the repulsive interaction acting between adatoms in opposite sublattices with a dependence:

$$U_{AB}(\mathbf{r}) = v_{AB}(r)\sin^2\left(\frac{\mathbf{\Delta K}}{2}\cdot\mathbf{r}+\theta\right) \tag{3.31}$$

where θ is the angle between $\mathbf{\Delta K}$ and $\mathbf{r}$. In other words, interaction potentials (3.30) and (3.31) shows the same angular dependence as the Friedel oscillations of a single impurity from (B.7), (B.8) . The radial dependence of the interaction is encoded in the functions $v_{AA}(r)$ and $v_{AB}(r)$, their signs are controlled by the adatom coupling t'. The most relevant property of these functions is that for weak-couplings v_{AA} is attractive and v_{AB} is repulsive, whereas the opposite situation is true for strong couplings ($|t'| > 1.5t$); the radial dependence will be studied in more detail in section (3.6) where we will see that in absence of dissipation they fall as $1/r^3$ at long distances.

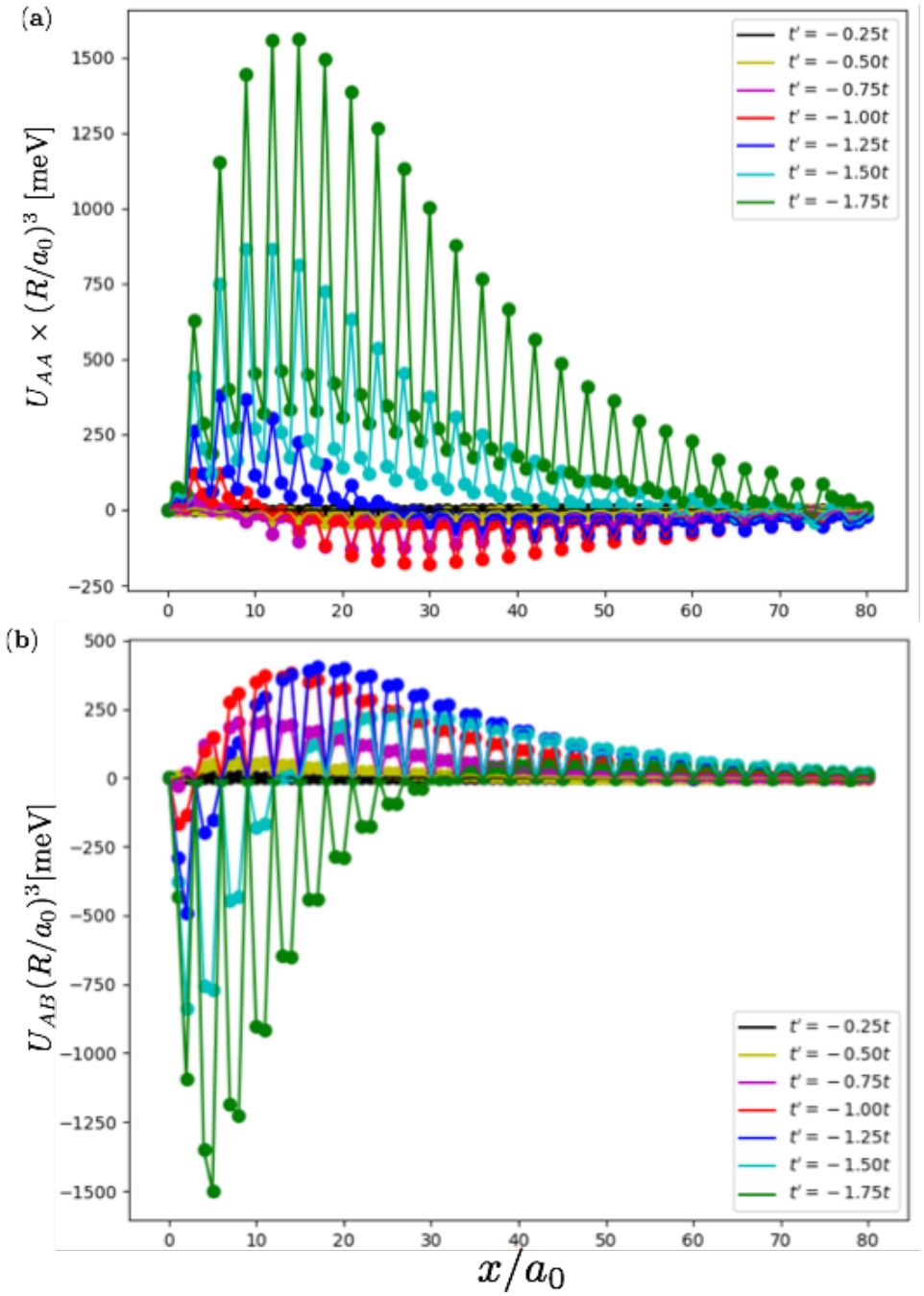

Figure 3.6: Interaction potential along the y direction for same-sublattice (panel a) and opposite-sublattice (panel b) for a set of values of t'. The transition from weak-coupling regime to strong-cupling regime occurs near $t' \approx 1.5t$

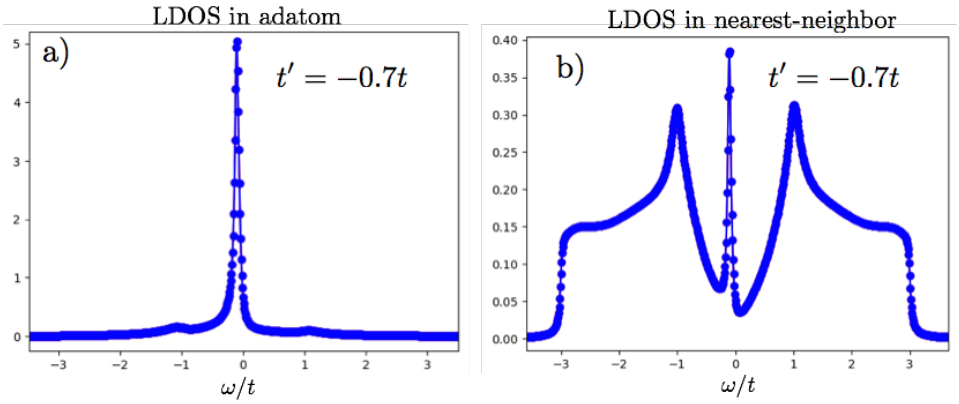

Figure 3.7: a) LDOS in the adatom in the weak-coupling limit $U = 0$ $\epsilon_0 = -0.15$t and $\gamma = -0.7$t for unstrained graphene. b) LDOS in the nearest neighbor of the host carbon

3.3 Kekulé ordering in strained graphene

3.3.1 Strained graphene

The positions of atoms in strained graphene are modified by $\mathbf{r}' = (1+\epsilon)\mathbf{r}$ where ϵ is the strain tensor:

$$\epsilon = \begin{pmatrix} \frac{\partial u}{\partial x} & \frac{1}{2}\left(\frac{\partial u}{\partial y} + \frac{\partial v}{\partial x}\right) \\ \frac{1}{2}\left(\frac{\partial u}{\partial y} + \frac{\partial v}{\partial x}\right) & \frac{\partial v}{\partial y} \end{pmatrix}$$

This modifies the nearest neighbor vectors of the honeycomb lattice $\delta_{\mathbf{1,2,3}}$. Due to modification of the bond-lengths, the hopping integrals between nearest neighbors in the presence of strain becomes:

$$t_i' = t_i e^{-\beta(\frac{\delta_i'}{a_{cc}} - 1)} \tag{3.32}$$

The modification of these distances also distorts the reciprocal lattice vectors $\mathbf{b_{1,2}} = \frac{2\pi}{a_0\sqrt{3}}(\pm 1, \frac{1}{\sqrt{3}})$:

$$\mathbf{b_1}' = \frac{2\pi}{a_0\sqrt{3}}\left(1 - \epsilon_{xx} - \frac{\epsilon_{xy}}{\sqrt{3}}, \frac{1}{\sqrt{3}} - \epsilon_{xy} - \frac{\epsilon_{yy}}{\sqrt{3}}\right) \tag{3.33}$$

$$\mathbf{b_2}' = \frac{2\pi}{a_0\sqrt{3}}\left(-1 + \epsilon_{xx} - \frac{\epsilon_{xy}}{\sqrt{3}}, \frac{1}{\sqrt{3}} + \epsilon_{xy} - \frac{\epsilon_{yy}}{\sqrt{3}}\right) \tag{3.34}$$

This shifts the K and K' valleys by an opposite pseudogauge vector [**?**]:

$$\mathbf{A} = \pm\frac{2\beta}{\sqrt{3}a_0}(\epsilon_{xx} - \epsilon_{yy}, -2\epsilon_{xy}) \tag{3.35}$$

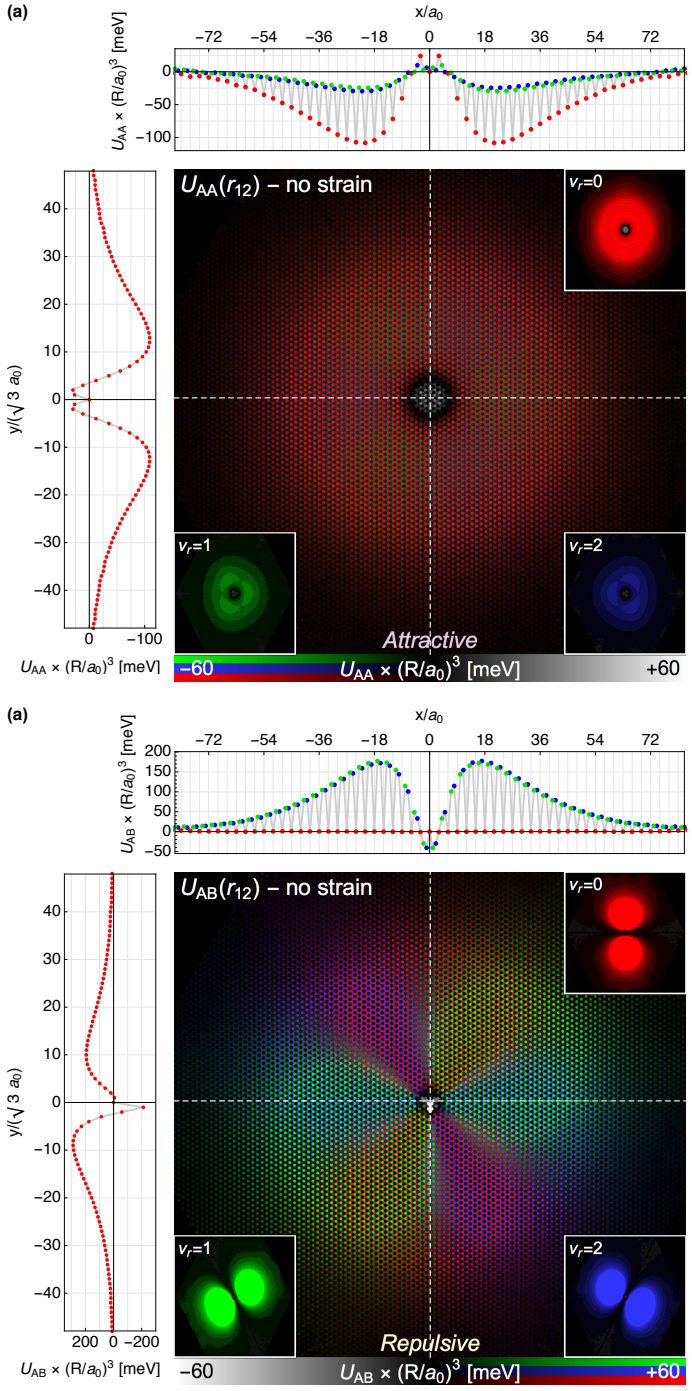

Figure 3.8: a) Map of the energy for top adsorbates in AA configuration for $U = 0$ $\epsilon_0 = -0.15$t and $\gamma = -0.7$t for unstrained graphene. The tight-binding approach gives a repulsive interaction the adatoms at very short distances, for larger distances the interaction becomes attractive with the typical $\cos^2 \frac{\Delta \mathbf{K}}{2}.\mathbf{r}$ Kekulé periodicity b) Interaction potential for adsorbates in AB configuration in the unstrained case for the same parameter values. The potential is repulsive for adatoms in different sublattices within this regime

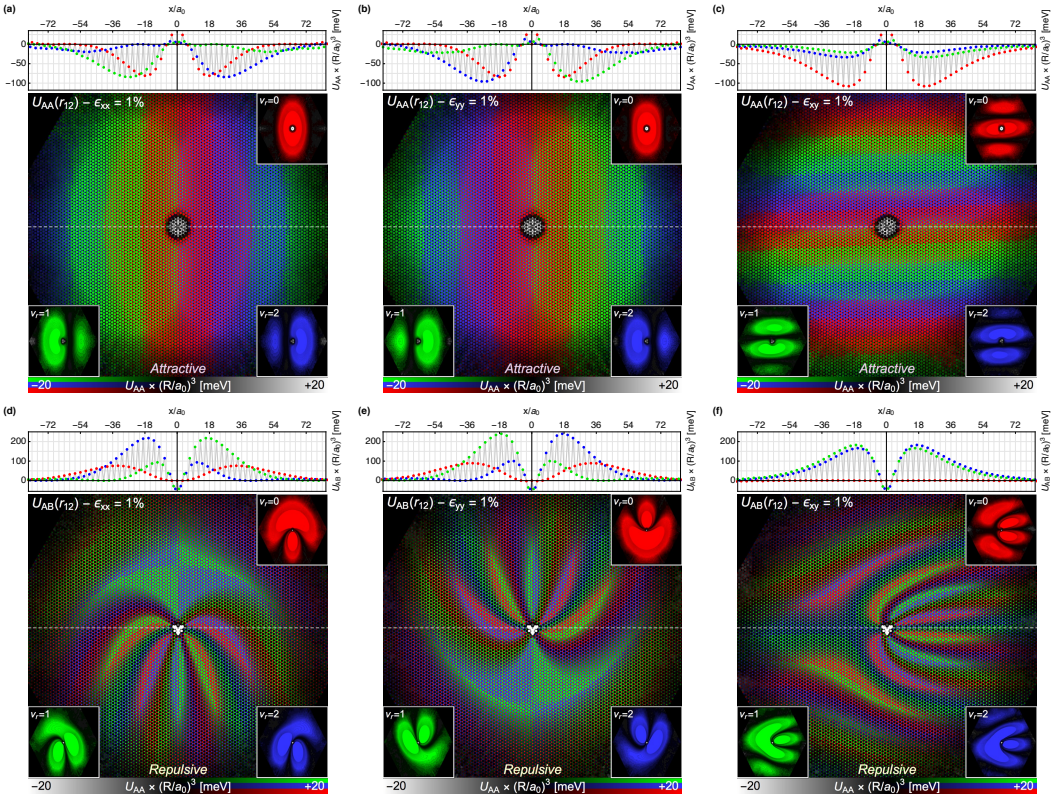

Figure 3.9: Interaction potential between adsorbates in the same sublattice in the presence of strain in graphene for a) $\epsilon_{xx} = 1\%$ b) $\epsilon_{yy} = 1\%$ and c) $\epsilon_{xy} = 1\%$. The Kekulé character acquires a modulation with distance that reflects the change of the intervalley separation $\mathbf{K} - \mathbf{K}'$ by a pseudogauge field. Panels d) e) and f) show the effects of the same strains in the case of adatoms in opposite-sublattices (repulsive interaction)

In the case of homogeneous strain, this pseudogauge potential is of no consequence to intra-valley physics, as it can be gauged away. It has however, a strong impact in intervalley scattering, since the Kekulé momentum transfer changes to $\mathbf{\Delta K} + 2\mathbf{A}$, therefore, it is expected that intervalley-dependent quantities such as the interaction potential between adatoms, to exhibit signatures of a uniform strain. The Kekulé modulation for weak-coupling now becomes:

$$U_{AA} = v_{AA}(r)\cos^2\left[(\mathbf{\Delta K} + 2\mathbf{A})/2 \cdot \mathbf{r}\right] \tag{3.36}$$

$$U_{AB} = v_{AB}(r)\sin^2\left[(\mathbf{\Delta K} + 2\mathbf{A})/2 \cdot \mathbf{r} + \theta\right] \tag{3.37}$$

This expectation is indeed confirmed by our numerical simulations. Figure 3.9 shows the modified potential U_{AA} (panels a-c) and U_{AB} (panels d-f) for the same parameters of Fig. 3.8 under an uniform 1% uniaxial strain along x and y directions, and a 1% uniform shear strain. We concentrate on the $U_{AA}(\mathbf{r})$ potential, as the U_{AB} remains repulsive and is thus irrelevant for the equilibrium adatom configurations. The equal-sublattice configuration is still the most stable one in the presence of strain in this regime. One immediately observes, however, a new spatial modulation in each of the Kekulé components that is linear in ϵ_{ij}. While a uniform Kekulé adatom configuration $\nu_{\mathbf{r}} = 0$ was favored in the case without strains, a 1% strain makes the potential minimum change Kekulé character with distance, precessing between $\nu_{\mathbf{r}} = 0, 1, 2$ (red, green, blue) as the two adatoms are separated (see vertical/horizontal stripes in Figs 3.9).

The spatial modulation is consistent with the form of $\mathbf{A}$ given in Eq. 3.35. Uniaxial strain ϵ_{xx} and ϵ_{yy} along the x and y directions both modulate the Kekulé character along the x direction, albeit in an opposite sequence order. In contrast, a shear strain ϵ_{xy} creates a modulation along the y direction, with a period that is half that of the uniaxial strain. The modulation period is given by $\pi/|6\mathbf{A}|$, i.e. around 3-4 nm for 1% of uniaxial strain.

For a large ensemble of adatoms, the Kekulé orientation of domains should also exhibit a spatial modulation. A given adatom will align its Kekulé index to nearby adatoms, with which interaction is strongest. However, the long-range coherence of Kekulé domains will be controlled by the long-range component of the interaction, so striped Kekulé domains are expected to arise even under weak uniform strains. This requires sufficiently long range interactions such as those observed in the experiment of Gutierrez et al (Kekulé domain sizes in the tens of nanometers and above, substantially greater than modulation periods at 1% strains). In such cases the spatial modulation of Kekulé alignement is expected to show a high sensitivity to the magnitude and type (uniaxial/shear) of strains in the sample.

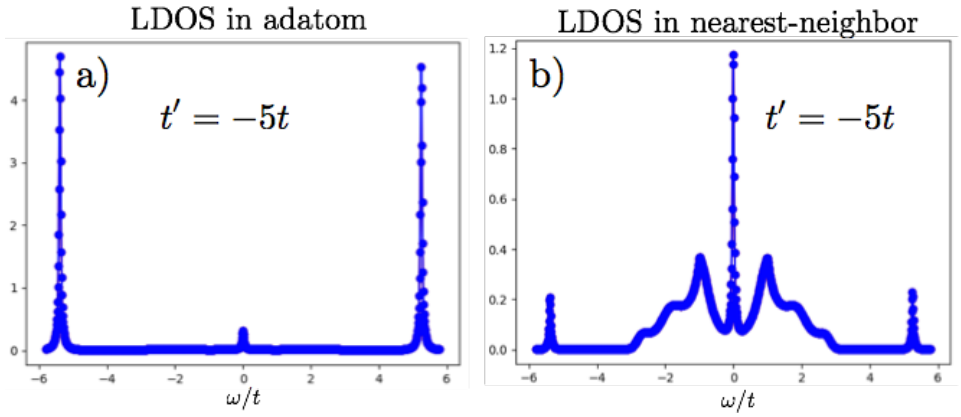

Figure 3.10: (a) Density of states in the strongly-coupled adatom (b) LDOS in the nearest neighbor of the host carbon atom. The coupling parameters are $\epsilon_0 = -0.15$t and $t' = -5.0$t.

3.4 Strong-coupling regime

In Fig. (3.6) , we have shown that for $t'/t \geq \pm 1.5$, the behavior of the interaction potential between adatoms in the same sublattice becomes repulsive, and the favored configuration for strongly-coupled adatoms is now in opposite sublattices. For $\epsilon_0 = -0.15$t and $t' = -5.0$t, the density of states of the strongly-coupled adatoms is modified, showing the peak near $\omega = \epsilon_0$ and two peaks beyond the bandwith of graphene, see Fig. (3.10). Without strain, different Kekulé alignments are favored (panel b) of Fig.(3.11) depending on the angle θ between $\mathbf{r}$ and $\mathbf{\Delta K}$ (here along the x direction). The U_{AB} potential that dominates the arrangement of adatoms is therefore non-isotropic, in contrast to the U_{AA} potential that controls the weak coupling regime. Most importantly, the magnitude of the adatom interaction is between one and two orders of magnitude stronger than in the weak coupling regime.

In the presence of strain, the interaction potential becomes modulated following the same pseudogauge mechanism described in the main text. However, since adatom ordering in the strong coupling regime is controlled by the non-isotropic potential U_{AB}, the effect of strain has a much richer structure in this case, see Figure 3.11b.

3.5 Adatom magnetization

Although we included the effect of electron-electron interactions in the description of the formalism of the two-impurity Anderson model, we have not yet discussed the case with $U \neq 0$. In this section, we consider intra-adatom

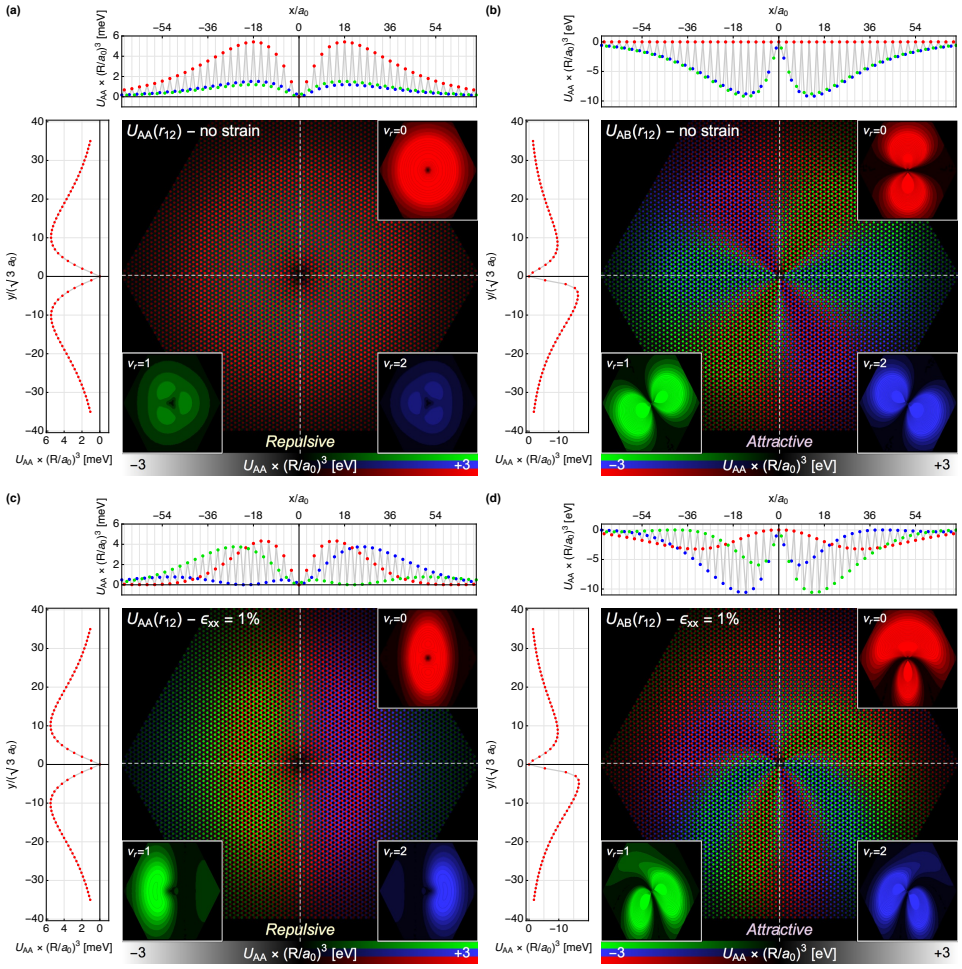

Figure 3.11: (a) Repulsive interaction potential U_{AA} for adatoms in opposite sublattices in the strong coupling regime, with no strain (b) Attractive interaction potential U_{AB} for adatoms in opposite sublattices in the strong coupling regime, with no strain c) Repulsive interaction potential U_{AA} for adatoms in the strong coupling regime, $\epsilon_{xx} = 1\%$ (d) U_{AB} in the strong coupling regime with $\epsilon_{xx} = 1\%$. The coupling parameters are $\epsilon_0 = -0.15$t and $t' = -5.0$t.

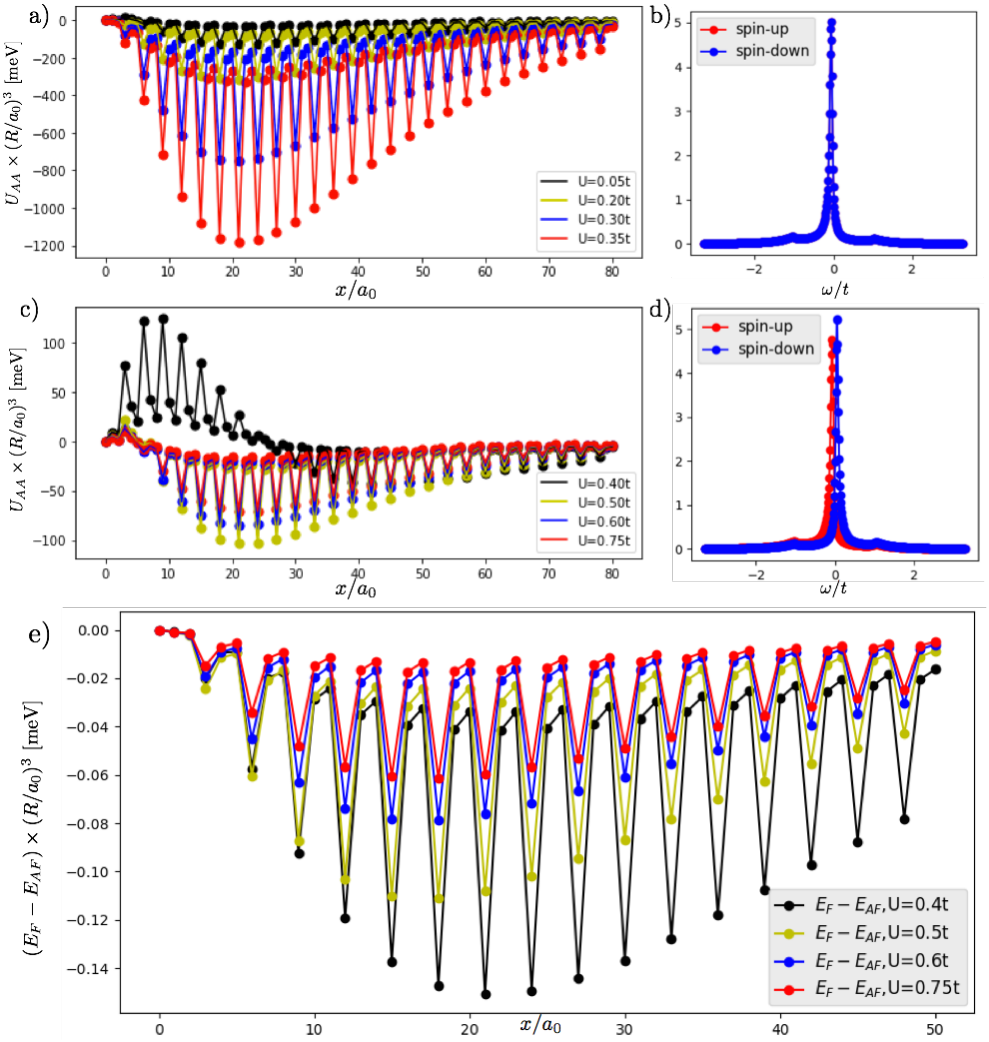

Figure 3.12: Panel (a) shows the interaction potential U_{AA} for values of U below U_c . (b) Density of states of the adatoms for $U = 0.25$t., there is no spin-splitting. (c) Interaction potential U_{AA} for $U > U_c$ (ferromagnetic regime) (d) Density of states of the adatoms for $U = 0.4$ t, showing the spin-splitting of the adatom energy level. e) Difference in energy between ferromagnetic alignment (E_F) and antiferromagnetic alignment (E_{AF}) between adatoms, it can be seen that the ground solution for AA adatoms is always ferromagnetic

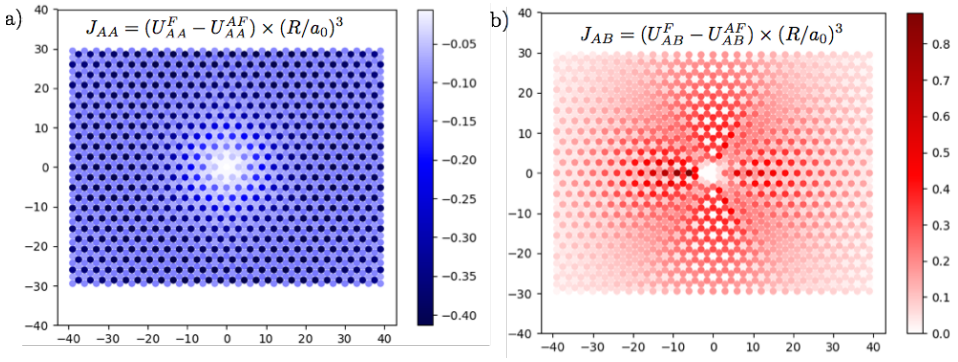

Figure 3.13: a) Exchange energy for adatoms in AA configuration. As stated before, the alignement is ferromagnetic. b) Exchange energy for adatoms in the AB configuration; in this case antiferromagnetic alignement is favored. The calculations were done with $U = 0.8$ t;$\epsilon_0 = -0.15$t; $t' = -0.7$t.

Hubbard interactions in the weak coupling limit. The spin-exchange interaction between magnetic adatoms in top positions is ferromagnetic when the adatoms are located in the same sublattice and antiferromagnetic when located in opposite sublattices [148,149], see Fig. (3.13). We have confirmed this result within our model, and have checked that the ferromagnetic character of the exchange remains unchanged under the application of strain in graphene. In the unstrained case, in the ferromagnetic regime the Kekulé $\cos^2\left(\frac{\Delta \mathbf{K}}{2} \cdot \mathbf{r}\right)$ periodicity is left intact. Only the envelope v_{AA} and v_{AB} of the oscillations is modified by the effect of U.

If the adatom is decoupled from graphene ($t' = 0$), the presence of an arbitrarily small U would open a spin-polarized splitting in the low-energy spectrum of the adatom. For $t' \neq 0$, our mean field approximation gives a minimum $U_c > 0$ required to create a non-zero magnetic moment in the adatoms. For $t' = -0.7$t and $\epsilon = -0.15$t , $U_c \approx 0.4$t. Our numerical calculations show that the effect of the electron-electron repulsion is two-fold. For $U < U_c$, the depth of the potential well increases with U, thus enhancing the attractive strength of the Kekulé ordering. In the regime of ferromagnetic alignment ($U > U_c$), the effect on the envelope is somewhat more complicated. For U very close to U_c the repulsive core around $\mathbf{r} = 0$ is increased, although the interaction quickly becomes attractive for longer distances. Upon further increase of U the repulsive core shrinks dramatically and the system returns to a behavior similar to the non-magnetic case. This behavior can be observed in Fig. 3.12.

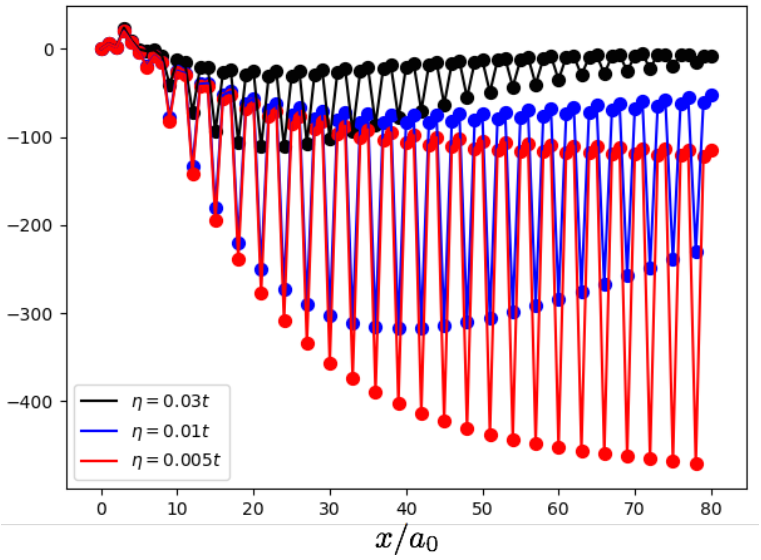

Figure 3.14: $U_{AA}(r)$ cut at $x = 0$ as the damping factor of electrons in graphene is reduced from $0.03t$ to $0.005t$. Note that as coherence increases, the potential becomes stronger and decays as $1/r^3$ (red line) at large distances.

3.6 Asymptotic radial dependence

It may be shown analytically [142] that a pristine and fully coherent graphene substrate leads to a same-sublattice adatom potential $U_{AA} = v_{AA}(r)\cos^2(\frac{\Delta \mathbf{K}}{2}\cdot \mathbf{r})$ that scales asymptotically as $v_{AA}(r) \sim 1/r^3$ with interadatom distance (at shorter distances, deviations are predicted depending on the adatom coupling strength [140]. This asymptotic result, however, assumes that dissipation is completely absent in the graphene electron liquid. Inelastic scattering events with phonons or through electron-electron interactions modify this result. In the previous sections, our simulations incorporated phenomenologically electronic dissipation by a finite imaginary part $\eta = 0.03t$ added to the energy $\omega + i\eta$ in the bare Green's functions g. The precise value of η adequate for a real system is model-dependent. Its effect on v_{AA}, however, is quite universal, and leads to a suppression of the interaction strength and a faster decay than $1/r^3$ at long distances. To make connection to the analytical results for fully coherent systems we present in this section results for $U_{AA}(\mathbf{r})$ as the damping factor η is reduced. Fig. 3.14 shows cuts at $x = 0$ as η is reduced from $0.03t$ to $0.005t$, in an $U_{AA}(r) \times (r/a_0)^3$ plot. We see clearly that the interaction strength is enhanced as the system becomes more coherent, and that the $1/r^3$ decay is recovered.

3.7 Hollow adatoms and benzene-like adsorbates

The formalism we explained in section 3.2 can be applied to other types of adsorbates, beyond the simple case of a top-adatom that couples to a single graphene site. Firstly, we discuss the case of adatoms located in the hollow position in the center of a graphene hexagon. Electrons in the hollow-adatom orbital can hop to the six closest graphene atoms. The interaction between hollow-adatoms provides an interesting counter-example to the case of top-adatoms, our numerical calculations show that the interaction potential between adatoms in hollow position does not present Kekulé oscillations; in agreement with [148, 149] and actually contradicting the results of [141]. In the magnetic case

We also consider the case of benzene adsorbates that become adsorbed in such a way that the atoms of the carbon atoms of the benzene lie in "bridge" position between two carbon atom of the graphene lattice, the geometry is shown in Fig. (3.16 a). The orbitals of the benzene adatoms are connected by nearest-neighbor hoppings and each benzene orbital has hoppings with its two nearest-neighbor graphene atoms. The spectrum of the adsorbed benzene molecule Fig. (3.16 b) shows a low DOS near the Fermi level, hence the benzene adsorbate does not become magnetic for reasonable values of the electron-electron interaction, and we neglect it in our discussion of benzene. Interestingly, the interaction between benzene adsorbates shows the same $\cos^2(\frac{\Delta \mathbf{K}}{2}.\mathbf{r})$ Kekulé periodicity as the interaction between top-adatoms Fig. (3.16 c-d).

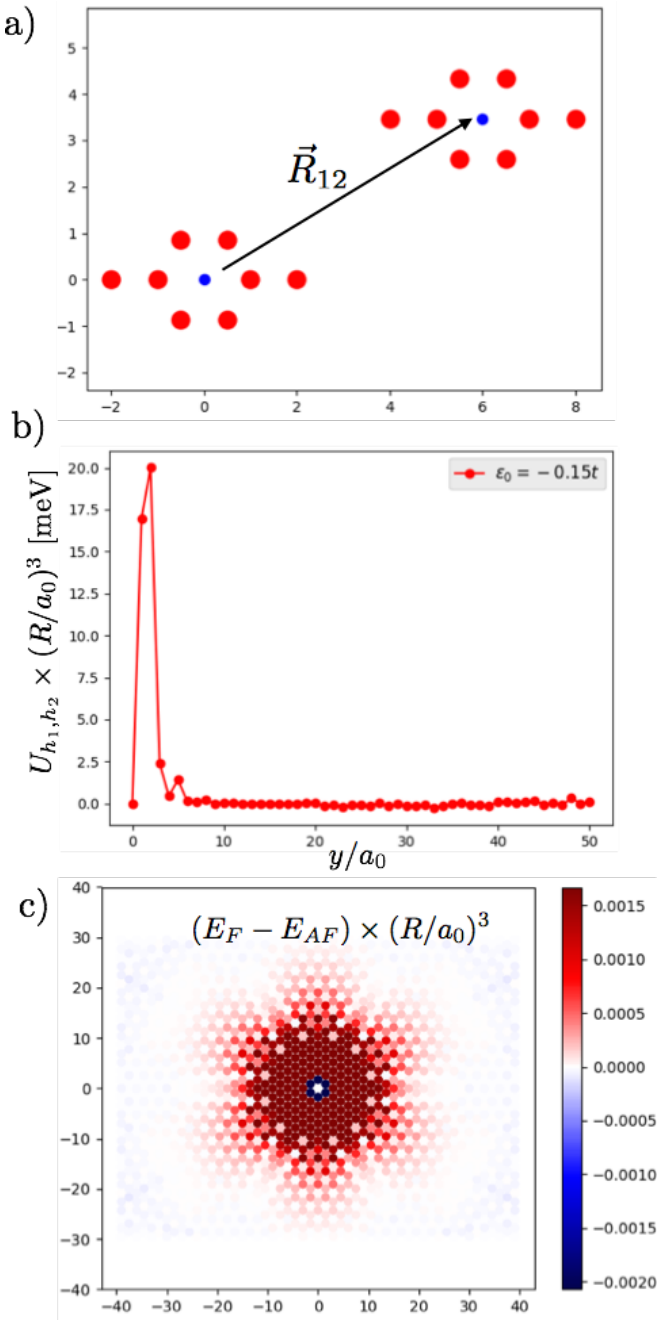

Figure 3.15: a) Geometry of the adatoms in the hollow position. Adatoms are shown in blue, red to the graphene unit cells below. b) Interaction potential between hollow adatoms ($t' = -0.7t$ and $\epsilon_0 = -0.15t$) in the $U = 0$ non-magnetic case. The interaction potential does not show Kekulé oscillations c) Map of the exchange energy. Blue regions are ferromagnetic, red regions prefer antiferromagnetic alignement. $U = 0.8$t

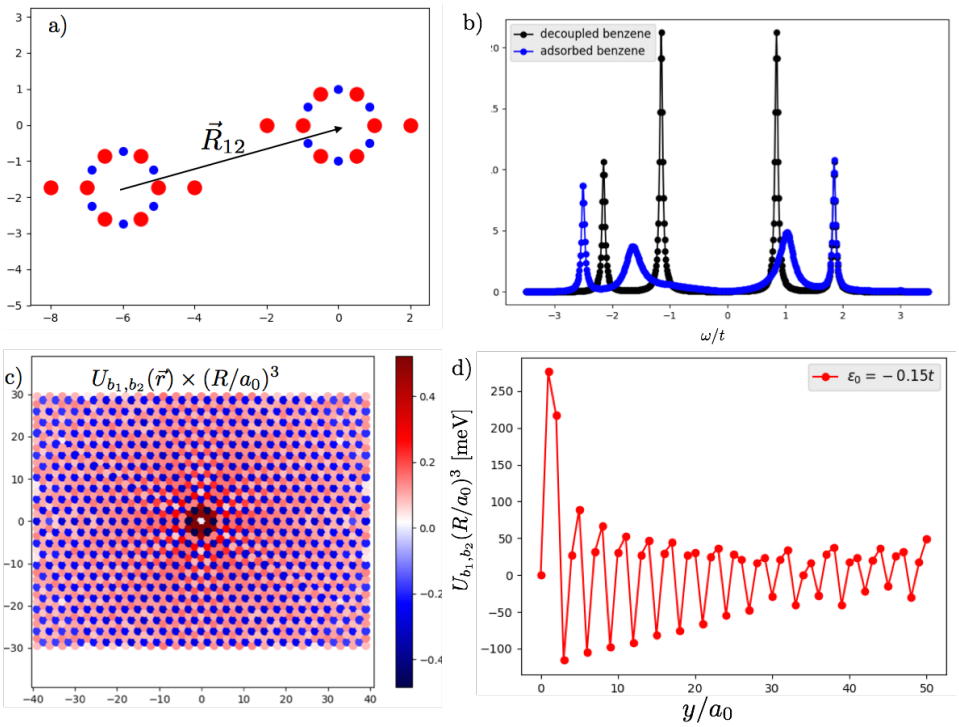

Figure 3.16: a) Geometry of benzene adsorbates. Blue atoms belong to benzene, red to the graphene unit cells below. b) DOS of the adsorbed benzene molecule ($t' = -0.7t$ and $\epsilon_0 = -0.15t$), unlike the top and hollow adatoms, the benzene adsorbate has a low DOS near the Fermi level c) Map of the interaction potential between the benzene molecules. The color scale here depicts points of attractive potential as blues, and points of repulsive potential as red d) Cut of the interaction energy between the benzenes along the y direction, showing the oscillatory Kekulé behavior

Chapter 4

Electrically controllable magnetism in twisted bilayer graphene

4.1 Introduction

Magnetism in 2D electronic systems is known to present a very different phenomenology from its three-dimensional counterpart due to the reduced dimensionality and the increased importance of fluctuations. Striking examples are the impossibility of establishing long range magnetic order in a 2D system without magnetic anisotropy [167] or the emergence of unique finite-temperature phase transitions that are controlled by the proliferation of topological magnetic defects [168]. In the presence of magnetic frustration, in, e.g., Kagome [169, 170] or triangular lattices [171–173], 2D magnetism may also lead to the formation of remarkable quantum spin-liquid phases [174, 175]. The properties of these states remain under active investigation, and have recently been shown to develop exotic properties, such as fractionalized excitations [176], long-range quantum entanglement of their ground state [177, 178], topologically protected transport channels [179], or even high-T_C superconductivity upon doping [219, 221].

The importance of 2D magnetism extends also beyond fundamental physics into applied fields. One notable example is data storage technologies. Recent advances in this field are putting great pressure on the magnetic memory industry to develop solutions that may remain competitive in speed and data densities against new emerging platforms. Magnetic 2D materials are thus in demand as a possible way forward [181]. Of particular interest for applications in general are 2D crystals and van der Waals heterostructures. These materials have already demonstrated a great potential for a

wide variety of applications, most notably nanoelectronics and optoelectronics [182–184]. Some of them have been shown to exhibit considerable tunability through doping, gating, stacking, and strain. Unfortunately, very few 2D crystals have been found to exhibit intrinsic magnetism [10,186], let alone magnetic frustration and potential spin-liquid phases.

Under the influence of a Hubbard term accounting for electron-electron repulsions, the half-filled honeycomb lattice undergoes a transition from a non-magnetic semimetal to an antiferromagnetic insulator [153]. At a Hartree-Fock mean-field level approximation, this transition is predicted to occur for $U_c \approx 2.23t$ where t is the hopping between nearest neighbors of the hexagonal lattice. In this, it differs from other bipartite lattices such as the square lattice which can support an antiferromagnetic ground state for any $U > 0$. A more powerful quantum Monte Carlo analysis of the Hubbard model that takes into account fluctuations (neglected in the mean-field approximation), shows that the antiferromagnetic transition occurs for $U_c \approx 4.5t$ [153–155]. Previously unnoticed, a gapped spin-liquid phase, in the region $3.5t < U < 4.3t$, showing no long-range antiferromagnetic order, was found to be intermediate between the semimetallic and the Mott insulating phase [156]. The phase diagram showing the gapped spin-liquid phase can be seen in Fig. (4.1).

For large twisting angles, twisted bilayer graphene (TBLG) has a low-energy band structure that is similar to that of the monolayer, showing a semi-metallic behavior. The Fermi velocity v_F of TBLG, however, is diminished with respect to the Fermi velocity of the monolayer, decreasing as the twisting angle is decreased. When a critical angle of around $\theta_c \approx 1.47^\circ$ is reached [157–159]; v_F becomes depleted, while for angles smaller than θ_c v_F enters an oscillatory regime, and the band structure is radically altered at low-energies. The Dirac cones of each separate monolayer cross at the M point of the moiré Brillouin zone, generating two low-energy Van-Hove peaks in the density of states around the Fermi energy. For small twisting angles the crossing at the M point occurs at very low-energies, eventually merging the Van-Hove peaks into a single peak at E_F for twisting of $\theta = 1.47^\circ$, see Fig. (4.2); in this critical angle regime the electron wave-function of this peak becomes localized in the AA regions of the moiré superlattice [160]. Furthermore, the application of an interlayer potential enhances the confinement of electrons in the AA-stacking regions of the moiré structure [195], in effect creating a triangular lattice of confined electrons.The problem of electron-electron interactions for the critical twist angle was hinted at in Ref. [162], but so far has not been treated in the literature.

The Hubbard model in triangular lattices at half-filling and zero temperature was studied in references [163,164] within a mean-field approxima-

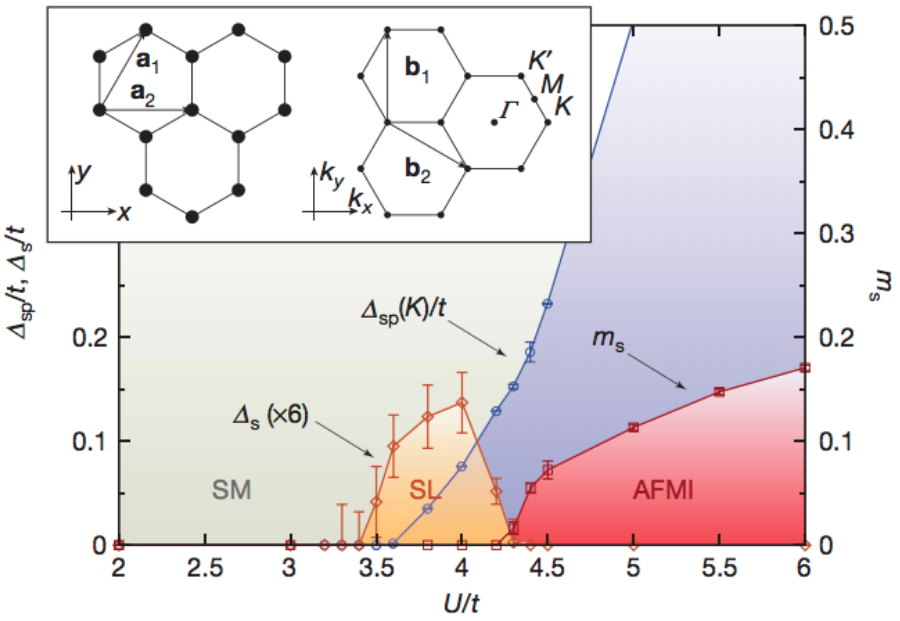

Figure 4.1: Phase diagram of the monolayer honeycomb lattice. SM (semimetallic phase) SL (gapped spin-liquid phase) AFMI (antIferromagnetic insulator phase) (Adapted with permission from [156])

tion. The triangular lattice undergoes phase transitions from a paramagnetic metal to a triangular antiferromagnetic insulator as the U/t ratio increases, see Fig. (4.3). Due to geometric frustration, in the triangular antiferromagnetic phase (also called spiral magnetic order) the spins of nearest-neighbor atoms have a relative orientation of 120° to one another, as can be seen in the inset of Fig. (4.3), thus yielding a zero net magnetization. Remarkably, the spiral magnetic order is not destroyed by quantum fluctuations around the ground state [165, 166].

For some twisting angles. see section (4.2), twisted bilayer graphene shows a commensurate triangular moiré pattern in the local stacking, alternating between three types of stacking (AA,AB and BA), see Fig. (4.4 c). We predict that twisted graphene bilayers could realize a peculiar magnetism on an effective triangular superlattice of AA regions, and with exchange interactions that may be tuned by an external electric bias. We show that, at a mean-field level, spontaneous magnetization of two different types may develop for small enough twist angles $\theta \leq 2°$ as a consequence of the moiré pattern in the system. This effect is a consequence of the high local density of states generated close to neutrality at moiré regions with AA stacking, triggering a Stoner instability when electrons interact. The local order is

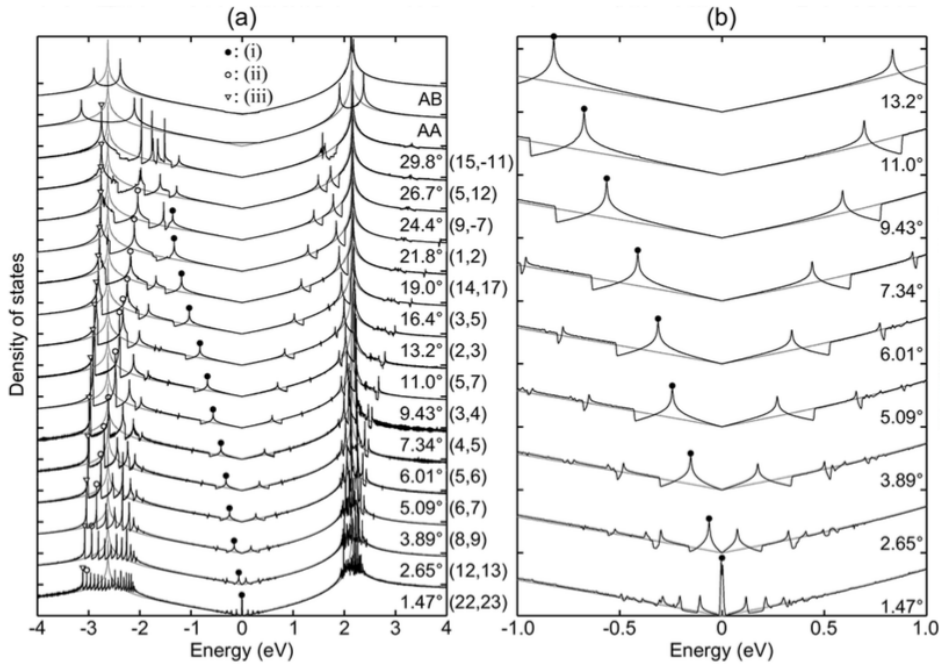

Figure 4.2: Densities of states of TBLG's with different twisting angles in (a) wide and (b) narrow ranges of the energy. The light gray lines in panel (b) correspond to the DOS of uncoupled bilayer graphene (twice the monolayer's DOS). Peaks of type (i) generate from the crossing of the Dirac cones of the separate monolayers, this band-crossing occurs for lower energies as the twisting-angle decreases.(Adapted with permission from [196])

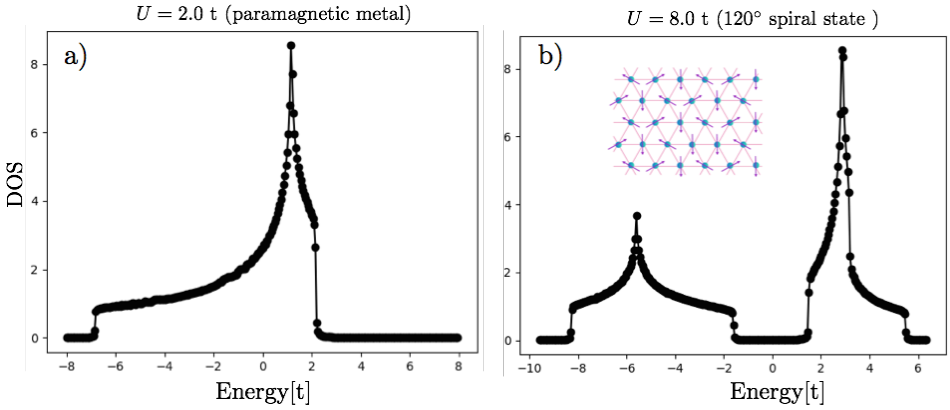

Figure 4.3: DOS of triangular lattice in the paramagnetic metallic phase (a) and the 120° spiral insulator phase (b). The inset in panel (b) shows schematically the orientations of the magnetic moments in the lattice in the spiral phase.

localized at AA regions but may be either antiferromagnetic (AF) or ferromagnetic (FM). The two magnetic orders can be switched electrically by applying a voltage bias between layers. Interestingly, the relative ordering between different AA regions in the FM ground state is predicted to be spiral, despite the system possessing negligible spin-orbit coupling. This type of magnetism combines a set of unique features: electric tunability, magnetic frustration, the interplay of two switchable magnetic phases with zero net magnetization, spatial localization of magnetic moments, and an adjustable period of the magnetic superlattice. In section 4.2, we present our re-escaled tight-binding model for TBLG, which allows us to reproduce the low-energy electronic structure of the low-angle regime with much smaller unit cells, we also discuss the effects of an interlayer potential bias in the non-interacting case. In section 4.3 we show the results of our collinear mean-field calculations within the minimal cell, in section 4.4 we address the issue of how the magnetic moments in neighboring AA-regions interact with one another via a non-collinear mean-field approach, presenting a phase diagram of the system as a function of electron-electron interaction and interlayer potential. Finally, in section 4.5 we summarize and discuss our results.

4.2 Tight-binding model for twisted graphene bilayers. Re-escaling

The TBLG lattice consists of two super-imposed graphene lattices rotated by an angle θ separated by a distance $d = 3.35$ A, see panel (a) Fig. (4.4). We label the bottom (top) monolayer by 1 (2). The carbon atoms of the monolayer 1 are located in positions given by the vectors:

$$\mathbf{r_{n,m}}^{1A} = n\mathbf{a_1} + m\mathbf{a_2} \tag{4.1}$$

$$\mathbf{r_{n,m}}^{1B} = n\mathbf{a_1} + m\mathbf{a_2} + \delta_\mathbf{1} \tag{4.2}$$

n and m are integers, $\delta_\mathbf{1}$ is the vector separating the A and B sublattices and $\mathbf{a_1}$ and $\mathbf{a_2}$ are the lattice vectors of graphene:

$$\mathbf{a_1} = a\left(\frac{\sqrt{3}}{2}\hat{x} - \frac{1}{2}\hat{y}\right) \tag{4.3}$$

$$\mathbf{a_2} = a\left(\frac{\sqrt{3}}{2}\hat{x} + \frac{1}{2}\hat{y}\right) \tag{4.4}$$

$$\delta_\mathbf{1} = \frac{\mathbf{a_1} + \mathbf{a_2}}{3} \tag{4.5}$$

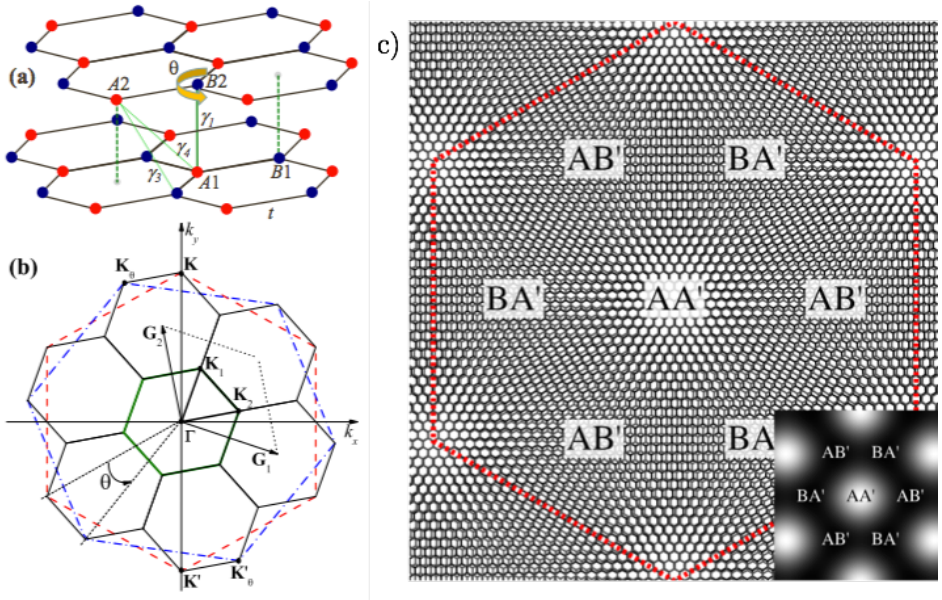

Figure 4.4: (a) Structure of the AB stacked graphene bilayer (b) The large hexagons show the Brillouin zones of individual layers: the red dashed hexagon corresponds to the bottom layer, the blue dot-dashed hexagon corresponds to the top layer for the twist angle $\theta = 21.787°$ ($m_0 = 1$, r=1). The first Brillouin zone of the bilayer is shown by the central (green) thick solid hexagon. The next several Brillouin zones of the tBLG are depicted by the six surrounding (black) thin solid hexagons. (c) Triangular moiré pattern of the TBLG showing the regions of AA, AB and BA stacking. Adapted with permission from [192]

The positions of atoms in monolayer 2 are given by:

$$\mathbf{r_{n,m}}^{2B} = n\mathbf{a_1}' + m\mathbf{a_2}' \tag{4.6}$$

$$\mathbf{r_{n,m}}^{2A} = \mathbf{r_{n,m}}^{2B} - \delta_\mathbf{2} \tag{4.7}$$

where $\mathbf{a_1}'$ and $\mathbf{a_2}'$ are given by:

$$\mathbf{a_1}' = \left(\cos\theta - \frac{\sin\theta}{\sqrt{3}}\right)\mathbf{a_1} + \frac{2\sin\theta}{\sqrt{3}}\mathbf{a_2} \tag{4.8}$$

$$\mathbf{a_2}' = \left(\cos\theta + \frac{\sin\theta}{\sqrt{3}}\right)\mathbf{a_2} - \frac{2\sin\theta}{\sqrt{3}}\mathbf{a_1} \tag{4.9}$$

and $\delta_\mathbf{2} = \left(\frac{\mathbf{a_1}'+\mathbf{a_2}'}{3}\right)$. For random θ angles the structure is incommensurate, and no unit cell can be constructed. The twisted bilayer graphene forms

periodic moiré patterns for θ angles that satisfy the condition:

$$\cos\theta = \frac{3m_0^2 + 3m_0 r + r^2/2}{3m_0^2 + 3m_0 r + r^2} \tag{4.10}$$

with m_0 and r are coprime positive integers. The number of atoms in the moiré unit cell is given by $N(m_0, r) = 4(3{m_0}^2 + 3m_0 r + r^2)$. The lattice vectors of the superlattice are:

$$\mathbf{R}_1 = m_0\mathbf{a}_1 + (m_0 + r)\mathbf{a}_2 \tag{4.11}$$

$$\mathbf{R}_2 = -(m_0 + r)\mathbf{a}_1 + (2m_0 + r)\mathbf{a}_2 \tag{4.12}$$

We consider a tight-binding Hamiltonian for the p_z orbitals of the carbon atoms in the lattice:

$$H = \sum_{i,j} -t_{i,j}(\mathbf{r_{ij}}){c_j}^\dagger c_i + \sum_i V_i c_i^\dagger c_i \tag{4.13}$$

where c_i destroys an electron in the p_z orbital of the i-th site and ${c_j}^\dagger$ creates an electron in the p_z orbital of the j-th site, $\mathbf{r}_{ij} = \mathbf{r}_i - \mathbf{r}_j = (x, y, z)$ is the vector separating the i-th and j-th site. The interlayer bias V_i is an onsite energy term with opposite sign in monolayers 1 and 2. The hopping parameter $t_{i,j}(\mathbf{r}_{ij})$ takes into account the fact that the distances between the atoms of the different monolayers are all different. The hopping function is:

$$\begin{aligned} t_{i,j}(\mathbf{r_{ij}}) = \gamma_0 \exp\left[\beta\left(\frac{r_{ij}}{a_{cc}} - 1\right)\right]\left(\frac{x^2 + y^2}{r_{ij}^2}\right) \\ +\gamma_1 \exp\left[-\beta\left(\frac{r_{ij} - d}{a_{cc}}\right)\right]\frac{z^2}{r_{ij}^2} \end{aligned} \tag{4.14}$$

where $\gamma_0 = -2.70$ eV is the hopping between nearest-neighbors in the same monolayer and $\gamma_1 = 0.48$ eV is the hopping between atoms belonging to different monolayer that are on top of each other. On the other hand, $\beta = 3.137$ is a dimensionless exponential decay factor. Hoppings between atoms for $r_{ij} > 4a_{cc}$ are negligible.

The Brillouin zone of the monolayers of the moiré superlattice are also rotated by an angle θ and their respective K points are separated by a distance $\Delta K(\theta) = \frac{4\pi}{3\sqrt{3}} 2\sin\theta/2$ in momentum space, see panel (b) in Fig. (4.4). The Dirac cones of the monolayers intersect in the M point of the Brillouin zone of the twisted bilayer superlattice. This intersection is observed as low-energy Van-Hove singularites in the total density of states of the superlattice. In the low θ limit, ΔK becomes increasingly smaller and the Dirac cones essentially intersect around zero energy, giving rise to a flat

band around the Fermi level for $\theta \approx 1.47^{\circ}$, corresponding to $r = 1$, $m_0 = 22$. Our main goal is to study the magnetic order in the mean-field limit originating from the electron confinement in the AA-stacking. However, this approach is extremely time-consuming since the unit cells for these angles contain more than 5000 atoms. Our strategy is therefore to do a re-escaling, in which low-energy electronic structure of the small-angle limit can be reproduced with a unit cell containing a smaller number of atoms (and larger twisting angle), while keeping invariant the two most important observables: the Fermi velocity and moiré period. It is easy to check that all this can be accomplished by setting:

$$\gamma_0' \to \frac{1}{\lambda}\gamma_0 \tag{4.15}$$

$$a_{cc}' \to \lambda a_{cc} \tag{4.16}$$

and:

$$d' \to \lambda d \tag{4.17}$$

where the dimensionless re-escaling parameter λ is given by:

$$\lambda = \frac{\sin\frac{\theta'}{2}}{\sin\frac{\theta}{2}} \tag{4.18}$$

In our notation all the primed quantities label the parameters of the re-escaled system. It is important to remark that our approach keeps invariant both the decoupled monolayer Fermi velocity as well as the renormalized Fermi velocity of the bilayer. We now study the density of states of the of a ($m_0 = 22$,$r = 1$) moiré reescaled into a ($m_0 = 8$,$r = 1$), see Fig. (4.5), panels (b) and (e). We obtain the spatial distribution of the peak at the Fermi level by plotting the local density of states in each site at $E = E_F$, shown in panels a) and d) of Fig. (4.5) for $V_b = 0$ and $V_b = 300$meV, respectively. We obtain the LDOS from the usual Green function expression $\rho(\mathbf{r_i}) = -\frac{1}{\pi} Im\left[G_{ii}(E = E_F)\right]$ where $G(E, \mathbf{r}) = \sum_k [(E + i\eta) - H(\mathbf{k})]^{-1}$. One can see that the re-escaling preserves the density of states (and the geometric distribution of the confined state in the lattice) of the low-angle case with a much smaller number of atoms, thereby speeding up our mean-field calculations. In the following section, our mean-field calculations will be carried out in the re-escaled unit cell.

Twisted graphene bilayers are characterized by a relative rotation angle θ between the two layers [157]. The rotation produces a modulation of the relative stacking at each point, following a moiré pattern of period $L_M \approx a_0 = \theta$ at small θ, where $a_0 = 0.24$ nm is graphenes lattice constant [159]. The stacking smoothly interpolates between three basic types, AA (perfect

local alignment of the two lattices), and AB or BA (Bernal stackings related by point inversion) [187]. The stacking modulation leads to a spatially varying coupling between layers. This results in a remarkable electronic reconstruction [188,189], particularly at small angles $\theta \leq 12^\circ$, for which the interlayer coupling $\gamma_1 \approx 0.3$ eV exceeds the moiré energy scale $\epsilon_M = \hbar v_F \Delta K$ [here, $\Delta K = 4\pi/(3L_M)$ is the rotation-induced wave vector shift between the Dirac points in the two layers, and $v_F \approx 10^6$ m/s is the monolayer Fermi velocity]. It was shown [159, 161, 162, 190–192] that in such a regime the Fermi velocity of the bilayer becomes strongly suppressed, and the local density of states close to neutrality becomes dominated by quasi- localized states in the AA regions [160]. The confinement of these states is further enhanced by an interlayer bias V_b, which effectively depletes the AB and BA regions due to the opening of a local gap [193, 194]. At sufficiently small angles this was also shown to result in the formation of a network of helical valley currents flowing along the boundaries of depleted AB and BA regions [195].

The quasilocalized AA states form a weakly coupled triangular superlattice of period L_M. Each AA dot has space for eight degenerate electrons, due to the sublattice, layer, and spin degrees of freedom. A plot of their spatial distribution under zero and large bias $V_b = 300$ meV is shown in Figs. (4.5 (a)) and 4.5(d), respectively. These AA states form an almost flat band at zero energy [158], see Figs. 4.5(c) and 4.5(e), which gives rise to a zero-energy peak in the DOS. The small but finite width of this zero-energy AA resonance represents the residual coupling between adjacent AA dots due to their finite overlap. The electronic structure presented here was computed using the tight-binding approach described, which includes a scaling approximation that allows the accurate and efficient computation of the low-energy band structure in low-angle twisted bilayers.

The interlayer potential bias has a twofold effect in the distribution of the flat-band state. In absence of bias the flat-band wave-function is equally distributed in both monolayers, but once a bias potential is applied the wave-function has different amplitudes in the two monolayers. We quantify this layer polarization by the adimensional quantity:

$$P_{layer} = \frac{\rho_2 - \rho_1}{\rho_2 + \rho_1} \tag{4.19}$$

where $\rho_{1,2}$

$$\rho_{1,2} = \sum_{layer 1,2} |\Psi(E_f, \mathbf{r_i})|^2 \tag{4.20}$$

The layer polarization increases almost linearly with interlayer bias as shown in panel (a) of Fig. (4.6). On the other hand, the interlayer potential also increases the confinement of the flat-band wave-function in the AA

region, thereby, depleting the AB-regions of electrons. This can be seen by plotting the ratio of the electron density in an atom of the AB region to an atom of the AA-region $|\Psi(E_f, AB)|^2/|\Psi(E_f, AB)|^2$ as a function of interlayer bias, see panel (b) of Fig. (4.6)

4.3 Mean-field Hubbard analysis

It is known that in the presence of sufficiently strong electronic interactions, a honeycomb tight-binding lattice may develop a variety of ground states with spontaneously broken symmetry [153, 199–202]. The simplest one is the lattice antiferromagnetic phase in the honeycomb Hubbard model. The Hubbard model is a simple description relevant to monolayer graphene with strongly screened interactions (the screening may arise intrinsically at high doping or e.g. due to a metallic environment). Above a critical value of the Hubbard coupling, $U > U_c^{(0)} \approx 5.7eV$ (value within mean field), the system favours a ground state in which the two sublattices are spin-polarized antiferromagnetically. This is known as lattice-AF order.

In the absence of adsorbates [91], edges [203], vacancies [204] or magnetic flux [205] isolated graphene monolayers, with their vanishing density of states at low energies, are known experimentally not to suffer any interaction-induced magnetic instability. In contrast, Bernal ($\theta = 0$) bilayer graphene and ABC trilayer graphene have been suggested [206–209] to develop magnetic order, due to their finite low-energy density of states, although some controversy remains [210–215].

Twisted graphene bilayers at small angles exhibit an even stronger enhancement of the low-energy density of states associated to AA-confinement and the formation of quasi-flat bands. It is thus natural to expect some form of interaction-induced instability in this system with realistic interactions, despite the lack of magnetism in the monolayer [216]. By analysing the Hubbard model in twisted bilayers we now explore this possibility, and describe the different magnetic orders that emerge in the U, V_b parameter space.

We consider the Hubbard model in a low angle $\theta \approx 1.5^\circ$ twisted bilayer for a moderate [217] value of $U = 3.7$eV, quite below the monolayer lattice-AF critical interaction $U_c^{(0)}$. The tight-binding Hamiltonian now includes de interaction terms:

$$H = \sum_{i,j} -t_{i,j}(\mathbf{r_{ij}}) {c_j}^\dagger c_i + \sum_i V_i c_i^\dagger c_i + U \sum_i n_{i\uparrow} n_{i\downarrow} \tag{4.21}$$

We use a self-consistent mean-field approximation to compute the system's ground state. Within the collinear mean-field approximation, the interacting

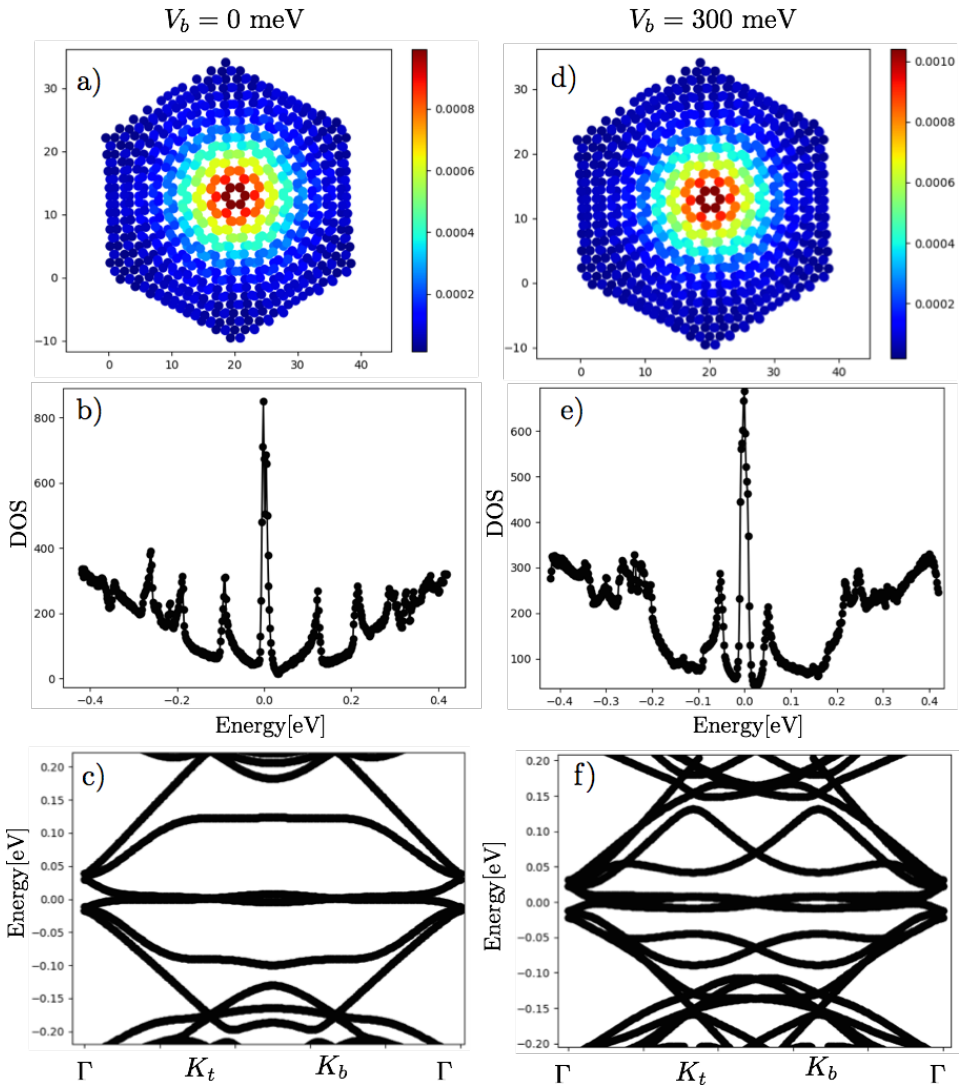

Figure 4.5: ($m_0 = 22$,$r = 1$) moiré reescaled into a ($m_0 = 8$,$r = 1$) with a unit cell of 868 atoms. Panels (a,b,c) show respectively, the lattice distribution of the peak at the Fermi level, the DOS, and the low-energy band structure for $V_b = 0$ meV. Panels (d,e,f) show the same for $V_b = 300$ meV. The bright-colored region in panels (a) and (d) corresponds to the regions of AA-stacking

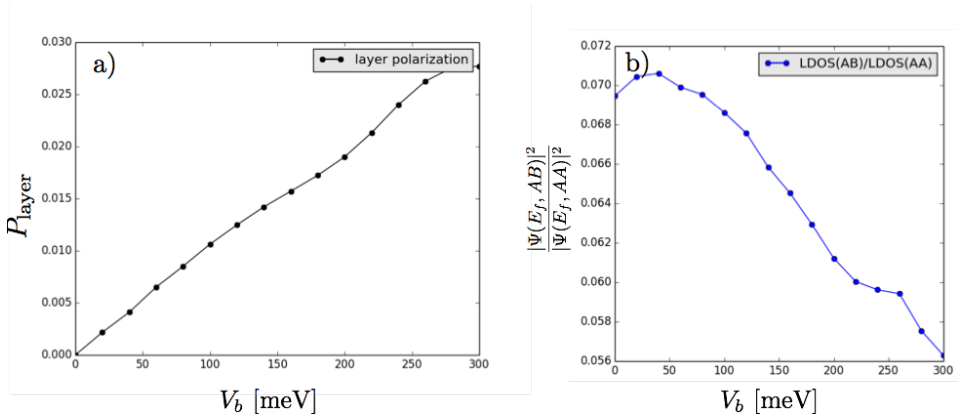

Figure 4.6: a) Layer polarization vs V_b b) Ratio of local density of states at an atom located in the AB-stacking region to an atom in the center of the AA-region vs V_b. The AB region becomes electronically depleted with increasing interlayer bias

part of the Hamiltonian reads:

$$H_{collinear} = U \sum_{i,s} n_{i,s} \langle n_{is'} \rangle - \langle n_{i\uparrow} \rangle \langle n_{i\downarrow} \rangle \tag{4.22}$$

Self-consistency involves the iterative computation of charge and spin density on the moiré supercell, integrated over Bloch momenta. Since U is repulsive we neglect superconducting symmetry breaking, and concentrate on arbitrary normal solutions instead [218]. In Fig. (4.7) we show the resulting real-space distribution of the ground-state spin polarization $M(\mathbf{r})$ of the converged solution.

We obtain two distinct solutions for the magnetization, depending on the interlayer bias V_b. At small interlayer bias and for the chosen $U = 3.7$ eV we see that the ferromagnetic polarization integrates to zero. Thus, the unbiased bilayer remains non-ferromagnetic in the small V_b case. However, the lattice-AF component of the polarization, panel (a), Fig. (4.7), is large and integrates to a non-zero value of around 0.5 electron spins per unit cell. This is the analogue of the monolayer lattice-AF phase, with two important differences. On the one hand, we find that the lattice-AF density is strongly concentrated at the AA regions instead of being spatially uniform like in the monolayer. On the other hand the lattice-AF ground state is found to arise already for $U \approx 2$eV, i.e. for much weaker interactions than in the monolayer. The reason for the reduction of U_c can be traced to the suppression of the Fermi velocity v_F at small twist angles [161, 162], which controls the critical U for the lattice-AF instability. The dependence of U_c

and v_F as a function of angle θ is shown in Fig (4.9) (a). This result already points to strong magnetic instabilities of twisted graphene bilayers as the angle falls below the $1-2^{\circ}$ threshold.

Under a large electric bias between layers, the ground state magnetization for the same U is dramatically different, see panels (c) of Fig (4.7). In this case, the lattice-AF polarization, is strongly suppressed and integrates to zero spatially, while the lattice-ferro component, becomes large around the AA regions, and integrates to a finite value of approximately 4 electron spins per moiré supercell. The AA regions are thus found to become ferromagnetic under sufficient interlayer bias. This type of magnetic order is the result of the increased confinement of AA states at high V_b, and can be interpreted as an instance of flat-band ferromagnetism driven by the Stoner mechanism. Importantly, the lattice-AF phase behaves like a Mott-insulator, see Fig. (4.7 b), whereas the lattice-ferromagnetic does not show a gap Fig. (4.7 d).

4.4 Non-collinear approach: Interaction between neighboring AA regions.

We want to explore the possibility of non-collinear alignments between the magnetic moments of adjacent AA-regions. The calculation of the total electronic energy as a function of the polarization angle α_M between magnetic moments of adjacent AA regions, requires diagonalization of a supercell containing three minimal unit cells, the lattice vectors of the triangular superlattice are:

$$\mathbf{T_1} = \mathbf{R_1} + \mathbf{R_2} = -r\mathbf{a_1} + (3m_0 + 2r)\mathbf{a_2} \tag{4.23}$$

$$\mathbf{T_2} = 2\mathbf{R_2} - \mathbf{R_1} = -(3m_o + 2r)\mathbf{a_1} + (3m_0 + r)\mathbf{a_2} \tag{4.24}$$

Since the diagonalization of the triangular superlattice is extremely time-consuming, our approach is to calculate self-consistently the magnetic moments contained within the minimal unit cell as explained above, and a non-collinear mean-field Hamiltonian is constructed for the triple supercell, by rotation of the spins in the neighboring minimal cells by an angle α_M. In the absence of magnetic anisotropy (such as the one caused by spin-orbit interactions), the Hubbard Hamiltonian must preserve spin-rotation symmetry (that is, the energy of an electron should be independent of the direction of magnetization). It's easy to check, in the one-electron case, that the collinear approximation (4.22) yields different energies for in-plane and off-plane spin-orientations, thus it breaks spin-rotation symmetry, and cannot be used for the exploration of non-collinear phases where both in-plane and

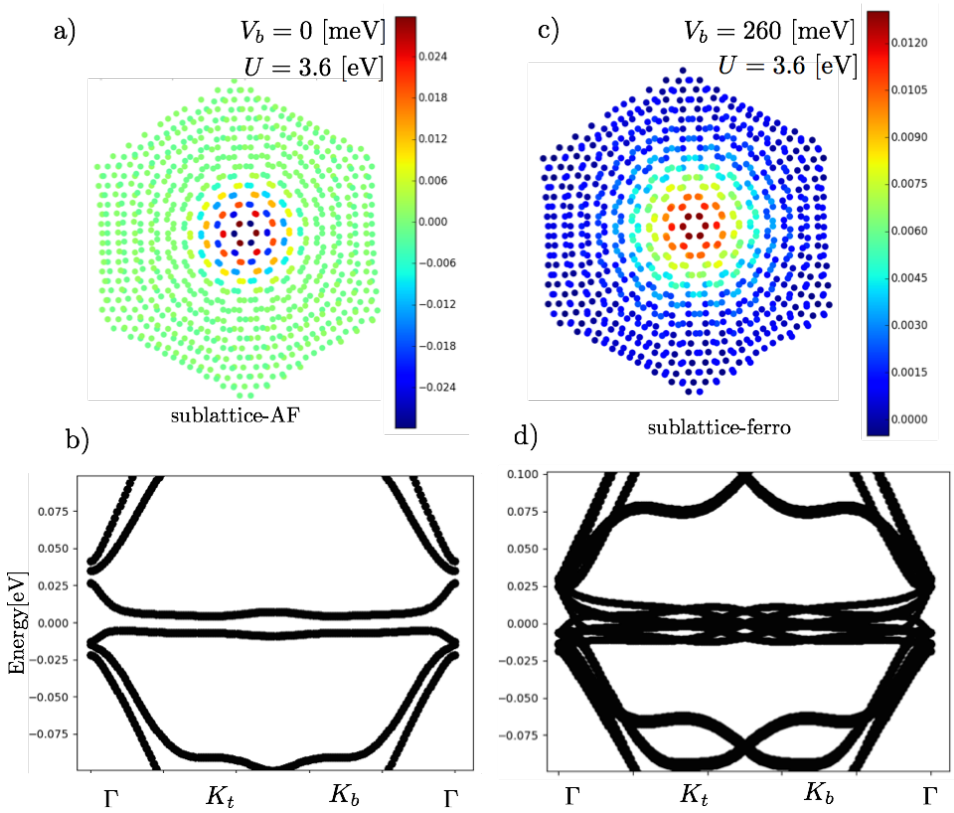

Figure 4.7: ($m_0 = 22$,$r = 1$) moiré reescaled into a ($m_0 = 8$,$r = 1$) with a unit cell of 868 atoms (a) Lattice distribution of the magnetic moments within the moiré minimal unit-cell in the sublattice-AF phase (a) and the corresponding band structure. Lattice distribution of the magnetic moments inside the minimal unit cell in the sublattice-ferromagnetic phase (c) and corresponding band structure (d). Notice that the sublattice-antiferromagnetic phase is gapped.

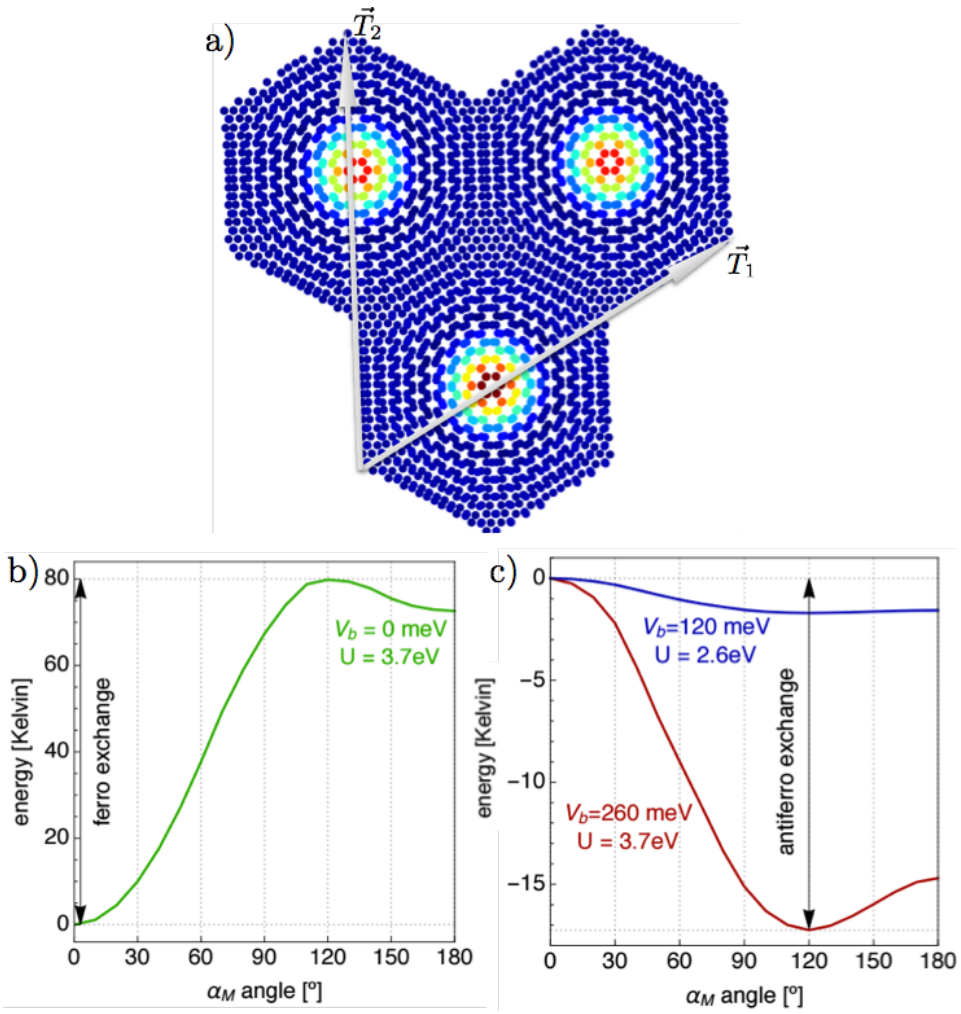

Figure 4.8: (a) Triple unit cell, containing three AA-regions used for calculations with non-collinear Hamiltonian (b) Total electronic energy in the triangular supercell as a function of the polarization angle α_M between the orientations of the spins in neighboring AA-regions. The sublattice-AF is collinear (i.e. the energy is minimized when $\alpha_M = 0°$). c) The ferromagnetic moments in neighboring AA-regions orient each other in a spiral configuration, typical of frustrated antiferromagnets in triangular lattices (i.e. energy is minimized for $\alpha_M = 120°$)

off-plane spin-components are expected. The full mean-field Hamiltonian that preserves spin-rotation symmetry [223]:

$$H_{non-col} = U \sum_{i,\sigma} \langle n_{i\sigma} \rangle n_{i\sigma'} - \langle c^{\dagger}_{i\sigma} c_{i\sigma'} \rangle c^{\dagger}_{i\sigma'} c_{i\sigma} - E_{DC} \tag{4.25}$$

where $E_{DC} = -U \left[\langle n_{i\uparrow} \rangle \langle n_{i\downarrow} \rangle - \langle c^{\dagger}_{i\downarrow} c_{i\uparrow} \rangle \langle c^{\dagger}_{i\uparrow} c_{i\downarrow} \rangle \right]$ is a constant term, it can be simply checked that the Hamiltonian (4.25) unlike (4.22) preserves spin-rotation symmetry, and thus we can use it for exploring the presence of spiral and non-collinear alignements. The new mean-values for the i-th site of this non-collinear Hamiltonian are calculated from the local magnetic moments from $\langle n_{i\uparrow} \rangle = \frac{1}{2}(M^i_0 + M^i_z)$, $\langle n_{i\downarrow} \rangle = \frac{1}{2}(M^i_0 - M^i_z)$,$\langle c^{\dagger}_{i\downarrow} c_{i\uparrow} \rangle = \frac{1}{2}(M^i_x - iM^i_y)$, $\langle c^{\dagger}_{i\uparrow} c_{i\downarrow} \rangle = \frac{1}{2}(M^i_x + iM^i_y)$.The minimal unit cell is chosen to be hexagonal and centered in the AA regions with vertices in the AB regions, since this geometry ensures that the rotations of the magnetic moments between adjacent minimall cells is carried out in an electronically depleted region, where the magnitude of the spins is negligible by comparison to the AA region. The non-collinear H_{MF} is constructed for each value of α_M and the total electronic energy is calculated by direct diagonalization of the new Hamiltonian.

The lattice-AF and lattice-F states are different when comparing the relative orientations of neighboring AA regions. By computing the total energy per supercell in each case as a function of the polarization angle α_M between adjacent regions (panels [b,d] of Fig. 4.8), we find that the energy is minimized for $\alpha_M = 0^{\circ}$ in the lattice-AF case (parallel alignment), but for $\alpha_M = 120^{\circ}$ in the lattice-F case (spiralling polarization). The depth of the energy minimum, ranging from $\sim 2 - 100$ Kelvin in our simulations, represents the effective exchange coupling of neighboring AA regions, which is ferromagnetic for lattice-AF states and antiferromagnetic for lattice-F states. In the latter, which from now on we denote spiral-F phase, the spiral order arises as a result of the triangular symmetry of AA regions that frustrates a globally antiferromagnetic AA-alignment. The same spiral order has been described in studies of the Hubbard model in the triangular lattice. It is a rather remarkable magnetic state, as the polarization at different points becomes non-collinear [165, 166, 172] despite the complete absence of spin-orbit coupling in the system. It moreover has zero mean spin polarization and therefore produces no stray magnetic fields. It is also electrically tuneable by V_b, and addressable without atomic-sized probes (the size of AA regions is in the tens of nanometers).

Our mean-field analysis neglects thermal and quantum spin fluctuations around the mean-field solution. Thermal spin excitations in the magnetically isotropic case under study (from gapless Goldstone modes) are expected to destroy long-range spiral order, which then survives only locally, in keeping

with the Mermin-Wagner theorem [167]. Breaking the magnetic isotropy (by allowing for a hard magnetic axis due to, e.g., spin-orbit coupling or coupling to a suitable magnetic substrate) gaps the Goldstone modes and stabilizes the mean-field solution. Otherwise, even at zero temperature, quantum spin fluctuations are known to produce spin-liquid-like ground states [171–173]. An efficient way to explore such nontrivial effects in this moiré system is to cast our mean-field results into an effective spin Hamiltonian on the triangular AA moiré pattern, which could be tackled using more sophisticated approaches (e.g., matrix-product states).

4.5 Summary and discussion

For a long time unmodified graphene was thought to be relatively uninteresting from the point of view of magnetism. Twisted graphene bilayers, however, could prove to be a surprisingly rich playground for non-trivial magnetic phases. We have shown that two different types of magnetic order arise spontaneously in twisted graphene bilayers at small angles. We identified two types of magnetic order, lattice-antiferromagnetism and spiral-ferromagnetism, both concentrated at AA-stacked regions. The spiral-F phase is favoured over the lattice-AF when applying a sufficient electric bias between layers. This phase constitutes a form of electrically-controllable, non-collinear and spatially non-uniform magnetism in a material with a negligible spin-orbit coupling.

This possibility is of fundamental interest, as it realizes electrically tunable 2D magnetism on a triangular superlattice, a suitable platform to explore spin-liquid phases. Indeed, it is known that next-nearest neighbour interactions in magnetic triangular lattice should transform spiral order into a spin-liquid phase [171–173], as long as the system remains magnetically isotropic. Moreover, in the spin-liquid state, electronic doping can give rise to high T_C superconductivity [219, 220]. The possibility of modifying the electronic filling of our emergent frustrated triangular lattice by means of an electric gate offers a unique platform to realize this possibility, avoiding the detrimental effects of chemical doping in conventional compounds [221]. While the above is highly speculative at this point and would require a careful nonperturbative analysis of our effective spin Hamiltonian, it highlights the interesting fundamental possibilities afforded by the rich magnetic phase diagram of twisted graphene bilayers.

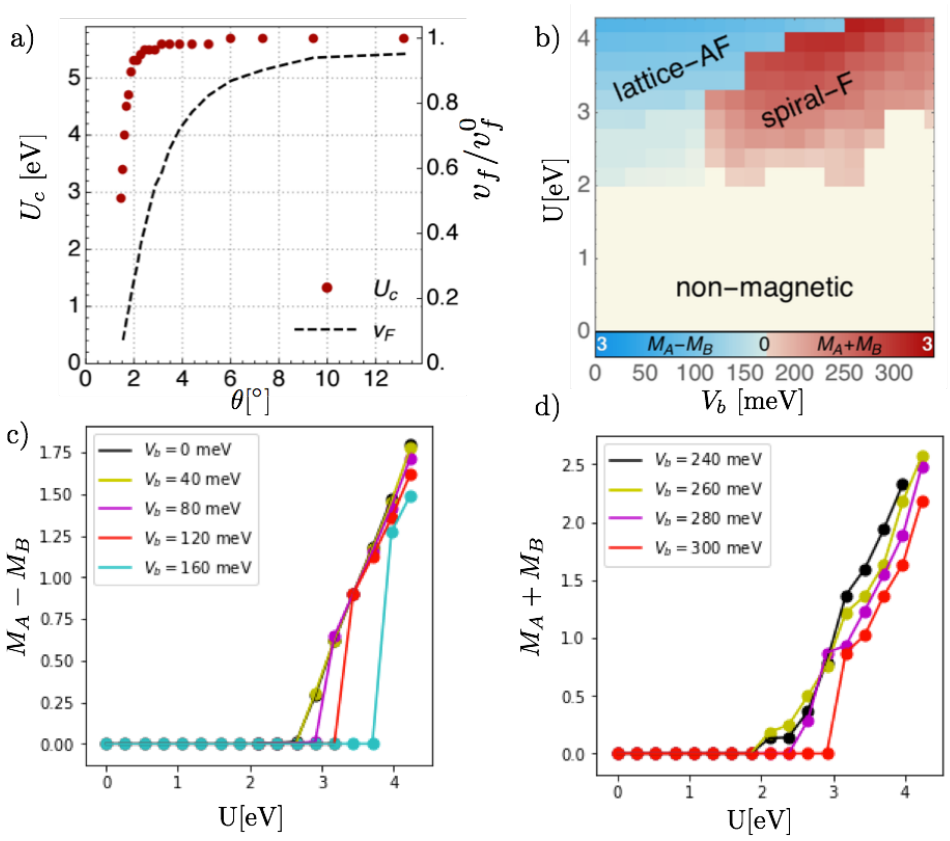

Figure 4.9: (a) Evolution of the critical U_c for antiferromagnetic transition of twisted bilayer graphene as a function of twisting angle (b) Phase diagram of twisted bilayer graphene in a (U, V_b) plane for $\theta = 1.47°$ (c) Vertical cuts of the phase-diagram showing the sublattice antiferromagnetic moment as a function of interaction strength U for several values of interlayer bias. (d) Magnitude of ferromagnetic moment accumulated in a unit cell in the spiral-magnetic phase as a function of interaction strength U

Concluding remarks

In chapter 1 we considered a simple analytical model of an electron tunneling through a confining helix potential under the influence of a Rashba-type SO-interaction (in the experiments with DNA, the SO interaction comes from the atomic cores of the carbons in the molecule). The resulting channels of the model helix are Kramers doublets involving opposite propagating and opposite spin projections at the same energy. An applied bias or otherwise preferred transport direction will then select a spin and effectively break time reversal symmetry (choosing one in a doublet pair) and transferring a particular spin. A calculation of the expectation value of the currents for eigenstates of different spins shows that electrons with different spins propagate at different velocities, thus yielding spin-selectivity.

In chapter 2, we considered a theoretical model for honeycomb crystals with top-adatoms arrayed in triangular superlattices, that takes into account the adatom-induced magnetization and spin-orbit couplings. This model differs from the Qian Niu proposal for QAH-effect in graphene, in a series of important aspects: not only is the distribution of magnetic moments non-uniform in this case, but in the absence of SO-couplings the system is gapped at the Fermi-level, thus the QAH-effect requires topological phase-transitions in which the trivial gap is closed and a non-trivial gap is opened. We found that the local adatom-induced SOC terms are incapable of inducing a phase transition to QAH-phase. We included in our model honeycomb crystals in which the uniform intrinsic and Rashba SO couplings cannot be neglected. Starting from a situation in which the intrinsic SOC is strong enough to mix the exchange-splitted impurity bands, a situation that can be realized for low-adatom concentrations, we have found that the Rashba parameter is capable of opening a gap with non-trivial topological properties, effectively turning the system into a QAH insulator with $\mathcal{C} = 1$. However the SO-induced magnetic anisotropy hinders the realization of the QAH-phase because it tends to favor an in-plane spin orientation; whereas the QAH-phase in graphene requires an off-plane spin-component.

In chapter 3, we investigated the interactions between pairs of top-adatoms in graphene, based on a tight-binding description and a two-impurity

Anderson model. First, we studied the case without any elastic strains. We found two regimes, one in which adatoms prefer to sit in AA configurations (for weak adatom-graphene coupling) and another in which their locations in opposite sublattices is favored (strong adatom-graphene coupling). We found that in the weak-coupling regime, the interaction between adatoms shows a $\cos^2\left(\frac{\Delta\mathbf{K}}{2}.\mathbf{r}\right)$ oscillation, preferring to sit in sites with the same Kekulé index ν_r, thus our result is consistent with experimental finds for ghost-adatoms [139]. We also studied the interaction in the case in which the adatoms are magnetized and found our results to be consistent with studies of the RKKY interaction of top-adatoms in graphene [149] .More importantly, we predict that uniform strains in graphene, that couple to the electronic momentum as a pseudogauge field, generate a spatial modulation of the Kekulé adatom ordering; we argue that these modulations can be used to deduce the magnitude and direction of the strains in graphene. Furthermore, our work can be the basis for a more statistical approach involving clusters of N interacting adatoms in strained graphene.

In chapter 4, we studied the flat-band magnetism that arises due to the supression of the Fermi velocity in small-angle twisted bilayer graphene. In absence of an interlayer potential bias, the system develops a sublattice-antiferromagnetic insulating state that differs from the one of the monolayer honeycomb in two important aspects: it is strongly localized in the region of AA-stacking in the moiré superlattice (unlike the uniformly distributed antiferromagnetism in the monolayer), and the semimetal-Mott insulator transition occurs for much smaller values of the electron-electron repulsion. We showed that the application of an interlayer bias enhances the confinement of electrons in AA-stacked regions, effectively creating a triangular lattice of AA-regions; in this regime, the magnetic moments inside each AA region couple ferromagnetically, but due to the geometric frustation of the triangular lattice, the coupling between neighboring AA regions becomes a 120° Neel state. The Mott-insulating sublattice-antiferromagnetic phase has been observed for small-angle in a recent experiment [222], although the authors only conjecture on type of magnetic ordering in the AA-regions.

Conclusiones

En el capítulo 1 hemos considerado un simple modelo analítico de un electrón que se propaga a lo largo de un potencial confinante en forma de hélice, bajo la influencia de un término de interacción espín-órbita de tipo Rashba (en los experimentos con ADN, la interacción EO deriva de los núcleos de los átomos de carbono de la molécula). Los canales resultantes de la hélice del modelo son dobletes de Kramers que incluyen proyecciones de espín opuestas que se propagan en direcciones opuestas a la misma energía. Una diferencia de potencial aplicada o alguna dirección de transporte preferida selecciona de esta manera una componente de espín y efectivamente rompe la simetría de reversión temporal y transfiriendo una componente de espín particular. Un cálculo de los valores esperados de las corrientes para autoestados de espines diferentes muestra que los electrones con diferentes espines se propagana a diferentes velocidades, de esta manera generando selectividad de espín

En el capítulo 2, consideramos un modelo teórico de cristales hexagonales con adátomos top en superreddes triangulares, este modelo toma en cuenta la magnetización y el acople espín-órbita (EO) inducidos por el adátomo. Este modelo difiere de la propuesta de Qian Niu para una fase de Efecto Hall Cuántico Anómalo (QAH sus siglas en inglés) en una serie de aspectos importantes: no solamente la distribución de momentos magnéticos en este caso es no-uniforme, sino que además en ausencia de acoples espín-órbita el sistema tiene una brecha aislante al nivel de Fermi, por lo tanto, la fase QAH requiere transiciones de fase topológicas en las cuales el gap trivial se cierra y se abre un gap no-trivial. Encontramos que el EO local inducido por el adátomo no puede inducir la transición a la fase QAH. Incluimos en nuestro modelo cristales hexagonales en los cuales el EO intrínseco y Rashba no pueden ser ignorados. Empezando en una situación en la cual el EO intrínseco es lo suficientemente fuerte para mezclar las bandas de impureza splitteadas por espín, lo cual puede lograrse para sistemas con baja concentración de adátomos, encontramos que el acople Rashba puede abrir un gap con propiedades topológicas no-triviales, convirtiendo al sistema en un aislante QAH con $\mathcal{C} = 1$. Sin embargo, la anisotropía magnética inducida por el acople EO obstaculiza la realización de la fase QAH, debido a que

tiende a favorecer una orientación de espín en el plano, mientras que el modelo de Qian Niu para la fase QAH en grafeno requiere una component de espín fuera del plano.

En el capítulo 3, investigamos las interacciones indirectas entre adátomos en la posición "top", basándonos en una descripción tight-binsing y en un modelo de Anderson para dos impurezas. Primero estudiamos el caso sin tensiones elásticas. Encontramos dos regímenes, uno en el cual los adátomos prefieren colocarse en configuraciones AA (para acoples grafeno-adátomo débiles). En este régimen, la interacción entre adátomos muestra una oscilación de tipo $\cos^2\left(\frac{\Delta\mathbf{K}}{2}.\mathbf{r}\right)$, prefiriendo arreglarse en sitios con el mismo índice de Kekulé ν_r; de esta manera, nuestro resultado es consistente con los resultados experimentales para adátomos "fantasma" en Ref. [139]. También, hemos estudiado la interacción en el caso en que los adátomos están magnetizados, y hemos visto que nuestros resultados son consistentes con los estudios de la interacción RKKY entre adátomos top en grafeno [149]. De más importancia, predecimos que las tensiones elásticas uniformes en grafeno, que se acoplan al momentum electrónico como un campo de pseudo-calibre, genera una modulación espacial del ordenamiento de Kekulé de los adátomos; argumentamos que estas modulaciones pueden ser usadas para deducir la magnitud y dirección de las tensiones elásticas en grafeno. Además, nuestro trabajo puede ser la base para una investigación de tipo estadístico de clusters de N adátomos interactuantes en grafeno con tensiones elásticas.

En el capítulo 4, estudiamos el magnetismo de bandas planas que surge debido a la supresión de la velocidad de Fermi en las bicapas de grafeno rotado en el límite de ángulos pequenos. En la ausencia de una diferencia de potencial entre las monocapas, el sistema desarrolla un estado de aislante antiferromagnético que difiere en dos aspectos importantes del estado análogo en la monocapa hexagonal: está fuertemente localizado en las zonas AA en la superred de moiré (a diferencia del antiferromagnetismo uniformemente distribuido en la monocapa), y la transición semimetal-aislante de Mott ocurre para valores mucho más pequenos de la repulsión electrón-electrón. Hemos demostrado que la aplicación de una diferencia de potencial entre las monocapas refuerza el confinamiento de electrones en las zonas AA, efectivamente creando una red triangular de zonas AA; en este régimen, los momentos magnéticos dentro de cada zona AA se acoplan de manera ferromagnética, pero debido a la frustración geométrica de la red triangular, el acople entre regiones AA colindantes es un estado de Neel de 120°. La fase de aislante de Mott antiferromagnética a medio llenado ha sido observada en un reciente experimento [222]; aunque los autores sólo ofrecen conjeturas respecto al tipo de orden magnético de zonas AA.

Appendix A

Hall conductivity and Berry curvature

In this appendix, we will derive an expression for the Hall conductivity σ_{xy} in terms of the Berry curvatures of the valence bands of a material. The Hall conductivity is calculated from the Kubo-formula:

$$\sigma_{xy} = \frac{ie^2}{\hbar} \sum_{\alpha} \int_{BZ} \frac{d^2k}{2\pi} \left[\langle \partial_y \Psi_k^\alpha | \partial_x \Psi_k^\alpha \rangle - \langle \partial_x \Psi_k^\alpha | \partial_y \Psi_k^\alpha \rangle \right] \tag{A.1}$$

where Ψ^α are eigenstates of the Hamiltonian, $\partial_{x,y}$ are derivatives with respect to k_x and k_y components of the reciprocal lattice vector, summation index α runs over all the valence bands of the material, and the integration is performed within the Brillouin zone and $i \left[\langle \partial_y \Psi_k^\alpha | \partial_x \Psi_k^\alpha \rangle - \langle \partial_x \Psi_k^\alpha | \partial_y \Psi_k^\alpha \rangle \right]$ is the Berry curvature of the Ψ^α band. (A.1) can be derived from the current response for particles in a lattice in the presence of a perturbing electric field, treating the field as a time-dependent perturbation [224].

Our approach will be somewhat different: in order to calculate σ_{xy}, we will use a method that is formally equivalent to the result obtained from linear response theory, but that is more computationally efficient [113]. We begin by defining the phase difference between the eigenfunctions at two different points in the Brillouin zone:

$$e^{-i\Delta\varphi_{12}} = \frac{\langle \Psi(\mathbf{k}_1) | \Psi(\mathbf{k}_2) \rangle}{|\langle \Psi(\mathbf{k}_1) | \Psi(\mathbf{k}_2) \rangle|} \tag{A.2}$$

$$\Delta\varphi_{12} = -\Im \log \left[\langle \Psi(\mathbf{k}_1) | \Psi(\mathbf{k}_2) \rangle \right] \tag{A.3}$$

This expression of course, depends on the arbitrary gauge choice for the wave-functions. However, if we now consider the total phase acquired along

a closed path in $\mathbf{k}$ space:

$$\begin{aligned}\gamma &= \Delta\varphi_{12} + \Delta\varphi_{23} + \Delta\varphi_{34} + \Delta\varphi_{41} \\ &= -\Im \log\left[\langle\Psi(\mathbf{k}_1)|\Psi(\mathbf{k}_2)\rangle\langle\Psi(\mathbf{k}_2)|\Psi(\mathbf{k}_3)\rangle\langle\Psi(\mathbf{k}_3)|\Psi(\mathbf{k}_4)\rangle\langle\Psi(\mathbf{k}_4)|\Psi(\mathbf{k}_1)\rangle\right]\end{aligned} \tag{A.4}$$

one can see that γ is a gauge-invariant quantity, given that all the gauge-dependent phases cancel each other along the closed path. Now, the Berry phase acquired along a continuum closed path would be:

$$\gamma = \sum_s \Delta\varphi_{s,s+1} \to \oint_C d\varphi \tag{A.5}$$

The linear differential $d\varphi$ is the phase difference between two contiguous points $\mathbf{k}$ and $\mathbf{k} + d\mathbf{k}$:

$$e^{-i\Delta\varphi} = \frac{\langle\Psi(\mathbf{k})|\Psi(\mathbf{k}+d\mathbf{k})\rangle}{|\langle\Psi(\mathbf{k})|\Psi(\mathbf{k}+d\mathbf{k})\rangle|} \tag{A.6}$$

if we assume that the phase varies in a differentiable way along the path, one obtains, to leading order in $\Delta\mathbf{k}$:

$$\Delta\varphi \approx i\langle\Psi(\mathbf{k})|\partial_k\Psi(\mathbf{k})\rangle\Delta\mathbf{k} \tag{A.7}$$

$$d\varphi \approx i\langle\Psi(\mathbf{k})|\partial_k\Psi(\mathbf{k})\rangle d\mathbf{k} \tag{A.8}$$

so the Berry phase can be written as:

$$\gamma = \oint_C i\langle\Psi(\mathbf{k})|\partial_k\Psi(\mathbf{k})\rangle d\mathbf{k} = \oint_C \mathbf{A}.d\mathbf{k} \tag{A.9}$$

where $\mathbf{A} = i\langle\Psi(\mathbf{k})|\partial_k\Psi(\mathbf{k})\rangle$ is called the Berry connection. The line integral over the closed path can be written in terms of a surface integral over the enclosed area, using Stoke's theorem:

$$\gamma = \oint_C \mathbf{A}.d\mathbf{k} = \int_S (\nabla_k \times \mathbf{A}).d^2\mathbf{k} \tag{A.10}$$

where $\mathbf{\Omega} = \nabla_k \times \mathbf{A} = -i\left[\langle\partial_y\Psi|\partial_x\Psi\rangle - \langle\partial_x\Psi|\partial_y\Psi\rangle\right]$ is the Berry curvature that appears in the integrand of eq. (A.1). Thus, the Berry phase can be understood as the "flux" of the Berry curvature through the area enclosed by path C. This is the basis of our numerical calculation of the Berry curvature, for a specific point in the Brillouin zone one can define a very short closed path around it, within the small enclosed surface (S) the Berry curvature is nearly constant, hence the Berry curvature can be calculated as:

$$\Omega = \frac{\gamma}{S} \tag{A.11}$$

with the Berry phase γ obtained from the product of the overlaps of the wave-functions at each step in the path:

$$\gamma = -\Im \log \prod_{s=1}^{M} \langle \Psi(\mathbf{k}_s) | \Psi(\mathbf{k}_{s+1}) \rangle \tag{A.12}$$

where the product index s runs over all the steps of the path. Finally, by summing the Berry curvature of each valence band over the Brillouin zone, one obtains the total Chern number, and thus the Hall conductivity.

Appendix B

Intervalley scattering and Friedel oscillations in graphene

In this appendix, we will discuss how a single impurity in a top position in graphene generates scattering terms that mix the **K** and **K′** valleys, and how this intervalley scattering produces oscillations in the density of states and particle density of graphene. These oscillations in DOS and particle density due to an impurity are the fundamental mechanism behind the Kekulé adatom ordering discussed in Chapter 3. We begin by considering an incoming wave in the **K** valley of graphene:

$$\Psi^{\mathbf{K}}_{inc}(\mathbf{r}) = \frac{1}{\sqrt{2}} e^{i\mathbf{k}.\mathbf{r}} \begin{pmatrix} 1 \\ s_E e^{i\theta} \\ 0 \\ 0 \end{pmatrix}$$

where θ is the angle between the propagating direction $\mathbf{r}$ and the x axis and free-particle eigenstate is written in the basis $|\mathbf{K}A\rangle$,$|\mathbf{K}B\rangle$, $|\mathbf{K}'B\rangle$, $|\mathbf{K}'A\rangle$ .The incoming wave is scattered by a sharp defect located in a single graphene atom at the origin of the coordinate system. In matrix form, the scattering potential is written:

$$V(\mathbf{r}) = u_0 \delta(\mathbf{r}) \begin{pmatrix} 1 & 0 & 0 & 1 \\ 0 & 0 & 0 & 0 \\ 0 & 0 & 0 & 0 \\ 1 & 0 & 0 & 1 \end{pmatrix}$$

The Lippman-Schwinger equation gives the outgoing wave as $\Psi_{out} = G_0^{gr}(r \to \infty, E)T(E)\Psi_{inc}^{\mathbf{K}}(\mathbf{r}=0)$ where

$$G_0^{gr}(r \to \infty, E) = \sqrt{\frac{is_E k}{8\pi r}} e^{ikr} e^{i\tau_z \mathbf{\Gamma K.r}}(1 + \tau_z \sigma_\theta) \tag{B.1}$$

is the asymptotic expansion of the Green's function of pristine graphene, $\sigma_\theta = \cos\theta\sigma_x + \sin\theta\sigma_y$ (in A,B sublattice pseudospin space) and τ_z acts in the valley subspace and $e^{i\tau_z \mathbf{\Gamma K.r}}$ encodes the phase-difference between waves in the $\mathbf{K}$ and $\mathbf{K'}$ valleys. $T(E) = V + G_0^{gr}VG_0^{gr} + G_0^{gr}VG_0^{gr}VG_0^{gr} + ...$ is the T matrix that yields the effect of the impurity in graphene. Within the First Born approximation, one can take only the first term of the expansion of the T matrix. Thus, the scattered wave can be calculated to first approximation as $\Psi_{out} = G_0^{gr}(r \to \infty, E)V(\mathbf{r})\Psi_{inc}^{\mathbf{K}}(\mathbf{r}=0)$:

$$\Psi_{out}(\mathbf{r}) = -\frac{u_0}{\sqrt{2}}\sqrt{\frac{is_E k}{8\pi r}} e^{ikr} \left[\begin{pmatrix} 1 \\ e^{i\theta} \\ 0 \\ 0 \end{pmatrix} + e^{-i(\mathbf{K}-\mathbf{K'}).\mathbf{r}} \begin{pmatrix} 0 \\ 0 \\ -e^{i\theta} \\ 1 \end{pmatrix} \right]$$

This means that a sharp defect is equally likely to produce intra-valley and inter-valley scattering.

Localized perturbations in a metal or semiconductor gives rise to an oscillating pattern in the local density of states (and of course, in the charge density) in the region around the disorder; these modulations are named Friedel oscillations . The exact origin of the perturbation can be manifold and may be caused by the presence of vacancies, ad-atoms, substitutional atoms and lattice deformations. Constructive interference between Friedel oscillations of two or more adsorbates yields energetically favored configurations, Fig. (3.1 d), thus, it is a fundamental mechanism to understanding long-range interactions between adsorbates. We now want to discuss the Friedel oscillations caused by inter-valley scattering at a top-defect in graphene localized in a single atomic site [152]. We now write the impurity potential $V(\mathbf{r}) = u\delta(\mathbf{r})$, in matrix form:

$$V(\mathbf{r}) = \begin{pmatrix} u\delta(\mathbf{r}) & 0 \\ 0 & 0 \end{pmatrix}$$

The perturbation of the Green's function of graphene due to the presence of the impurity potential is given by the Lippman-Schwinger equation, which can be expanded in the Born approximation as:

$$G_{gr}^0 = G_{gr}^0 + G_{gr}^0 V G_{gr}^0 + G_{gr}^0 V G_{gr}^0 V G_{gr}^0 + ... \tag{B.2}$$

keeping the first-order correction in the Green's function, the correction is $\Delta G(z,\mathbf{r},\mathbf{r}) = G^0_{gr}V(\mathbf{r})G^0_{gr} = uG^0_{gr}(z,\mathbf{r},0)G^0_{gr}(z,0,\mathbf{r})$

$$\Delta G^{gr}_A = u_0 G^0_{AA}(\mathbf{r},E)G^0_{AA}(-\mathbf{r},E) \tag{B.3}$$

$$\Delta G^{gr}_B = u_0 G^0_{BA}(\mathbf{r},E)G^0_{AB}(-\mathbf{r},E) \tag{B.4}$$

depending on whether $\mathbf{r}$ is in the vicinity of an A or B site, and $\varphi(\mathbf{r}-\mathbf{r}_B)$. The Green's functions around the $\mathbf{K}$ and $\mathbf{K'}$ valleys are:

$$G^0_K(\mathbf{r},E) = \frac{-ik}{4}e^{i\mathbf{K}.\mathbf{r}}\begin{pmatrix} H_0(kr) & -ie^{-i\theta}H_1(kr) \\ ie^{i\theta}H_1(kr) & H_0(kr)\end{pmatrix}$$

$$G^0_{K'}(\mathbf{r},E) = \frac{-ik}{4}e^{i\mathbf{K'}.\mathbf{r}}\begin{pmatrix} H_0(kr) & ie^{i\theta}H_1(kr) \\ -ie^{-i\theta}H_1(kr) & H_0(kr)\end{pmatrix}$$

and the total Green's function for low-energies is the sum of the contributions from the two valleys $G^0_{gr} = G^0_K + G^0_{K'}$. Using the asymptotic expansion of the Hankel functions,

$$H^1_0(kr) \to \sqrt{\frac{2}{i\pi kr}}e^{ikr} \tag{B.5}$$

$$H^1_1(kr) \to -i\sqrt{\frac{2}{i\pi kr}}e^{ikr} \tag{B.6}$$

one can obtain, after a little algebra, that the change in local density of states $\Delta\rho = -\frac{1}{\pi}Im\Delta G_g r(\mathbf{r},\mathbf{r})$ is:

$$\Delta\rho_A = -\frac{u_0k^2}{\pi^2}\frac{\cos 2kr}{2kr}\cos^2\left(\frac{\Delta\mathbf{K}}{2}.\mathbf{r}\right) \tag{B.7}$$

$$\Delta\rho_B = \frac{u_0k^2}{\pi^2}\frac{\cos 2kr}{2kr}\sin^2\left(\frac{\Delta\mathbf{K}}{2}.\mathbf{r}+\theta\right) \tag{B.8}$$

where $\Delta\mathbf{K} = \mathbf{K}-\mathbf{K'}$. The change in particle density (at zero temperature) is given by the integral of the change in LDOS over all energies below the Fermi level E_F:

$$\Delta n_A = -\frac{u_0\hbar v_F}{8\pi^2r^3}\left[\cos(2k_Fr)+2k_Fr\sin(2k_Fr)\right]\cos^2(\frac{\Delta\mathbf{K}}{2}.\mathbf{r}) \tag{B.9}$$

$$\Delta n_B = \frac{u_0\hbar v_F}{8\pi^2r^3}\left[\cos(2k_Fr)+2k_Fr\sin(2k_Fr)\right]\sin^2\left(\frac{\Delta\mathbf{K}}{2}.\mathbf{r}+\theta\right) \tag{B.10}$$

Although the calculation of the Friedel oscillations that we have described here is for the case of a substitutional impurity, it is also valid for the case of an ad-atom. The adatom Hamiltonian is $H_{ad} = \epsilon_d d^\dagger d$, where operators $d^\dagger$ and d create and annihilate electrons in the adatom orbital, respectively.

The effect of the adatom on the graphene lattice can be introduced by a self-energy term in the Hamiltonian of graphene $\Sigma_{ad} = t'^{\dagger} G_{ad} t'$, where the Green's function of the adatom is simply $G_{ad} = \frac{1}{\epsilon + i\delta - \epsilon_d}$, and t' is the coupling between graphene and the adatom. The self-energy term in graphene becomes $\Sigma_{ad} = \frac{(t')^2}{\epsilon + i\delta - \epsilon_d}$. Hence if we want to study the effects of the adatom on graphene, one can treat the adatom as a substitutional impurity that changes the onsite potential at the host carbon site to $\frac{(t')^2}{\epsilon + i\delta - \epsilon_d}$.

Bibliography

[1] S. Mayer, C. Nolting and J. Kessler. J. Phys. B: At. Mol. Opt. Phys. **29** 34973511 (1996)

[2] K. S. Novoselov, A. K. Geim1, S. V. Morozov, D. Jiang, Y. Zhang, S. V. Dubonos, I. V. Grigorieva, A. A. Firsov. Science **306**, 5696 (2004)

[3] B. Uchoa, V. N. Kotov, N. M. R. Peres and A. H. Castro Neto. Phys. Rev. Lett. **101**, 026805 , (2008)

[4] C. Weeks, J. Hu, J. Alicea, M. Franz, and Ruqian Wu. Phys. Rev. X **1**, 021001 (2011)

[5] Ugeda, M. M., Brihuega, I., Guinea, F. Guinea and J.M. Gómez-Rodríguez, . Phys. Rev. Lett. **104**, 096804 (2010).

[6] Yu Zhang, Si-Yu Li, Huaqing Huang, Wen-Tian Li, Jia-Bin Qiao, Wen-Xiao Wang, Long-Jing Yin, Ke-Ke Bai, Wenhui Duan, and Lin He. Phys. Rev. Lett. **117**, 166801 (2016)

[7] J. Koutecky, Trans. Faraday Soc. 54, 1038. (1958)

[8] T.B. Grimley, Adv. Catalysis **12**, 1 (1960)

[9] T.B. Grimley, Proc. Phys. Soc. **90**, 3 (1967)

[10] B. Huang, G. Clark, Dahlia R. Klein, D. MacNeill, E. Navarro-Moratalla , K. L. Seyler, N. Wilson, M. A. McGuire, D. H. Cobden, Di Xiao, W. Yao, P. Jarillo-Herrero, X. Xu. arXiv:1802.06979 (2018)

[11] A. N. Rudenko, F. J. Keil, M. I. Katsnelson, and A. I. Lichtenstein Phys. Rev. B **88**, 081405 (2013)

[12] W. Thomson, Baltimore lectures on molecular dynamics and the wave theory of light, London (1824).

[13] R. Naaman and D. Waldeck, Annu. Rev. Phys. Chem. **66**, 263 (2015).

[14] L. Barron Chirality, magnetism and light. Nature **405**, 895 (2000).

[15] S. Ravi, P. Sowmiya and A. Karthikeyan, Spin **3**, 13500031 (2013).

[16] Z. Xie, T. Z. Markus, S. R. Cohen, Z. Vager, R. Gutierrez, and R. Naaman, Nano Lett. **11**, 4652 (2011).

[17] K. Ray, S. P. Ananthavel, D. H. Waldeck, and R. Naaman, Science, **283**, 814 (1999).

[18] M. Kettner et al, J. Phys. Chem. C **119**, 14542 (2015).

[19] D. Cahen, R. Naaman and Z. Vager, Adv. Funct. Mater **15**, 1571 (2005).

[20] D. C. Ralph, Magn. Matter, **320**, 1190 (2008).

[21] C. Wang, Y. T. Cui, J. A. Katine, R. A. Buhrman, D. C. Ralph, Nat. Phys. **7**, 496 (2011).

[22] J. Sinova, I. Zutic, Nat. Mat. 11, 368 (2012).

[23] Guy, Contemp. Phys. **33**, 327 (1992).

[24] T. Ritz, S. Adem, K. Schulten, Biophys. J. **78**, 707 (2000).

[25] T. Ritz, P. Thalau, J. B. Phillips, R. Wiltschko, W. Wiltschko, Nature **429**, 177 (2004).

[26] E. M. Gauger, E. Rieper, J. J. L. Morton, S. C. Benjamin, V. Vedral, ar- Xiv:0906.3725v5 (2011).

[27] T. Aqua, R. Naaman, and S. S. Duabe, Langmuir **19**, 10573 (2003).

[28] R. Naaman, L. Sanche, Chem. Rev. **107**, 1553 (2007).

[29] S. Mayer, J. Kessler, Phys. Rev. Lett. 74 4803 (1995).

[30] S. Mayer, C. Nolting, J. Kessler, J. Phys. B 29 3497 (1996).

[31] E. Medina, F. Lopez, M. A. Ratner, and V. Mujica, Europhys. Lett. **99**, 17006 (2012).

[32] S. Yeganeh, M. A. Ratner, E. Medina, V. Mujica, V., J. Chem. Phys. **131**, 014707 (2009).

[33] R. Gutíerrez, E. Díaz, R. Naaman, and G. Cuniberti, Phys. Rev. B, **85**, 081404(R) (2012).

[34] R. Gutiérrez, E. Díaz, C. Gaul, T. Brumme, F. Domínguez-Adame and G. Cuniberti, J. Phys. Chem. C **117**, 22276 (2013).

[35] Ai-Min Guo and Qin-Feng Sung, Proc. Natl. Acad. Sci. USA, **111**, 11658 (2014).

[36] T. Ando, J. Phys. Soc. Jpn. **69**, 1757 (2000).

[37] F. Kuemmeth, S. Ilani, D. C. Ralph, P. L. McEuen, Nature, **452**, 448 (2008).

[38] I. Zutic, J. Fabian, and S. Das Sarma,. Rev. Mod. Phys. **76**, 323 (2004).

[39] I. Zutic, H. Dery, Nat. Mat. **10**, 647 (2011).

[40] M. J. Stevens, A. L. Smirl, R. D. R. Bhat, A. Najmaie, J.,E. Sipe, and H. M. van Driel Phys. Rev. Lett. **90**, 136603 (2003).

[41] M. Johnson, and R. H. Silsbee, Phys Rev. B **37**, 5312 (1988).

[42] B. Gohler, V. Hamelbeck, T. Z. Markus, M. Kettner, G.F. Hanne, Z. Vager, R. Naaman, H. Zacharias, Science , **33**1, 894 (2011);

[43] R. Naaman, David, H. Waldeck, J. Phys. Chem. Lett., **3**, 2178 (2012).

[44] S. Varela, E. Medina, F. López, and V. Mujica, J. Phys.: Cond. Matt. **26**, 015008 (2014).

[45] R. Rosenberg, J. Symonds, V. Kalyanaraman, T. Markus, N. Elyahu, T. M. Orlando, R. Naaman, E. Medina, F. López, V. Mujica , J. Phys. Chem. C, **117**, 22307 (2013).

[46] A. M. Guo, and A. F. Sun, Phys. Rev. Lett. **108** 1082012 (2012).

[47] A. A. Eremko, and V. M. Loktev, Phys. Rev. B **88**, 165409 (2013).

[48] D. Frustaglia and K. Richter Phys. Rev. B **69** 235310, (2004)

[49] I. Tinoco, R. W. Woody, J. Chem. Phys. **40**, 160 (1964).

[50] D. Huertas, F. Guinea, A. Brataas, Phys. Rev. B **74**, 155426 (2006)

[51] S. Konschuh, M. Gmitra, and J. Fabian, Phys. Rev. B **82**, 245412 (2010).

[52] F. E. Meijer, A. F. Morpurgo and T. M. Klapwijk, Phys. Rev. B **66** 033107 (2002).

[53] B. Berche, C. Chatelain, and E. Medina, Eur. J. Phys. **31**, 1267 (2010).

[54] C. L. Kane, and E. J. Mele, Phys. Rev. Lett. **95**, 226801 (2005).

[55] B. Berche, E. Medina, and A. López, Europhys. Lett. **97**, 67007 (2012).

[56] T. Ando, J. Phys. Soc. Jap. **69**, 1757 (2000).

[57] V. Mujica, and M. A. Ratner Chem. Phys. **264**, 365 (2001).

[58] Vitor M. Pereira, J. M. B. Lopes dos Santos, and A. H. Castro Neto. Phys. Rev. B **77**, 115109, (2008)

[59] M.M. Ugeda, I. Brihuega, F. Guinea, and J. M. Gómez-Rodríguez. Phys. Rev. Lett. **104**, 096804, (2010)

[60] D. W. Boukhvalov, M. I. Katsnelson, A. I. Lichtenstein. Phys. Rev. B **77**, 035427 (2008)

[61] A.H. Castro Neto, F. Guinea, Phys. Rev. Lett. **103** , 026804 (2009)

[62] M. Gmitra, D. Kochan, J. Fabian,. Phys. Rev. Lett. **110**, 246602 (2013)

[63] C.L. Kane and E.J. Mele. Phys. Rev. Lett. **95**, 226801 (2005)

[64] M. Gmitra, S. Konschuh, C. Ertler, C. Ambrosch-Draxl, and J. Fabian, Phys. Rev. B **80**, 235431 (2009).

[65] Z. Qiao, S. A. Yang, W. Feng, W. Tse, J. Ding, Y. Yao, J. Wang, Q. Niu. Phys. Rev. B. **82**, 161414(R) (2010)

[66] F.D.M Haldane, Phys. Rev. Lett **61**, 18 (1988)

[67] M. Ezawa. Phys. Rev. Lett. 109, 055502 (2012)

[68] F. Geissler, J. C. Budich, B. Trauzettel. New J. Phys. 15 085030 (2013)

[69] H. Pan, Z. Li, C.C. Liu, G. Zhu, Z. Qiao, Y. Yao,. Phys. Rev. Lett. **12**, 106802 (2014)

[70] C. Weeks, J. Hu, J. Alicea, M. Franz, and R. Wu. Phys. Rev. X. **1**, 021001 (2011)

[71] J. Hu, J. Alicea, R. Wu, and M. Franz. Phys. Rev. Lett. **109**, 266801 (2012)

[72] A. Cresti, D. Van Tuan, D. Soriano, A.W. Cummings, and S. Roche. Phys. Rev. Lett. **113**, 246603 (2014)

[73] V.N. Kotov, B. Uchoa, V.M. Pereira, F. Guinea, and A.H. Castro-Neto. Rev. Mod. Phys. **84**, 1067 (2012)

[74] Oleg V. Yazyev and Lothar Helm Phys. Rev. B **75**, 125408 , (2007)

[75] J.J. Palacios, J. Fernández-Rossier, L. Brey. Phys. Rev. B **77**, 195428, (2008)

[76] P. Haase, S. Fuchs, T. Pruschke, H. Ochoa, and F. Guinea. Phys. Rev. B. **83**, 241408 (2011)

[77] N.A. Pike, D. Stroud. Phys. Rev. B **89**, 115428 (2014)

[78] F. Gargiulo, G. Autes, N. Virk, S. Barthel, M. Rosner, L.R.M. Toller, T.O. Wehling, and O. Yazyev. Phys. Rev. Lett. **113**, 2476601, (2014)

[79] F. Calleja, H. Ochoa, M. Garnica, S. Barja, J. J. Navarro, A. Black, M. M. Otrokov, E. V. Chulkov, A. Arnau, A. L. Vázquez de Parga, F. Guinea, R. Miranda, Nature Phys. **11**, 43 (2015).

[80] J. Zhou, Q. Wang, Q. Sun, X.S. Chen, Y. Kawazoe and P. Jena. Nano Lett. **9**, 3867, (2009)

[81] M. Sepioni, R.R. Nair, S. Rablen, J. Narayanan, F. Tuna, R. Winpenny, A.K. Geim, and I. R. Grigorieva. Phys. Rev. Lett. **105**, 207205 (2010)

[82] A.R. Wright, T.E. O'Brien, D. Beaven, and C. Zhang. Applied Phys. Lett. **97**, 043104 (2010)

[83] R.R. Nair, M. Sepioni, I.L. Tsai, O. Lehtinen, J. Keinonen, A. V. Krasheninnikov, T. Thomson, A.K. Geim, and I.V. Grigorieva, Nature Phys. **8**, 199, (2012)

[84] K.M. McCreary, A.G. Swartz, W. Han, J. Fabian, and R.K. Kawakami. Phys. Rev. Lett. **109**, 186604 (2012)

[85] S. Barja, M. Garnica, J.J. Hinarejos, A.L Vázquez de Parga, N. Martin, and R. Miranda. Chem. Commun. **46**, 8198 (2010)

[86] J. M. MacLeod and F. Rosei, Small **10**, 1613 (2014)

[87] A.V. Shytov, D.A. Abanin,and L.S. Levitov. Phys. Rev. Lett. **103**, 016806 (2009)

[88] I. Brihuega, SPICE workshop, Magnetic adatoms as building blocks for quantum magnetism (2015)

[89] V.V. Cheianov, O. Syljuasen, B.L. Altshuler, and V.I. Fa'lko, Europhys. Lett. **89**, 56003 (2010)

[90] D.A. Abanin, A.V. Shytov, and L.S. Levitov, Phys. Rev. Lett. **105**, 086802 (2010)

[91] H. González-Herrero, J. Gómez-Rodríguez, P. Mallet, M. Moaied, J. J. Palacios, C. Salgado, M. M. Ugeda, J.-Y. Veuillen, F. Yndurain, and I. Brihuega, Science **352**, 437 (2016).

[92] D. Kochan, M. Gmitra and J. Fabian. Phys. Rev. Lett. **112**, 116602 (2014)

[93] Note, however, that spin-orbit coupling terms of order ~ 1 eV, although not of the Rashba type, have been reported for Pb intercalated CVD graphene [79].

[94] C.-C. Liu, H. Jiang and Y. Yao, Phys. Rev. B **84**, 195430 (2011)

[95] S. Rachel and M. Ezawa, ArXiv e-prints (2013), 1312.1848

[96] H. Min,J. E. Hill, N.A. Sinitsyn, B.R. Sahu, L. Kleinman and A.H. MacDonald, Phys. Rev. B **74** 165310 (2006)

[97] Y. Yao, F. Ye, X.-L. Qi, S.-C. Zhang, and Z. Fang, Phys. Rev. B **75**, 041401 (2007)

[98] S. Konschuh, M. Gmitra and J.Fabian, Phys. Rev. B **82**, 245412 (2010)

[99] C.-C. Liu, W. Feng and Y. Yao, Phys. Rev. Lett. **107**, 076802 (2011)

[100] Z.F. Wang, Z. Liu, and F. Liu, Nat. Commun **4**, 1471 (2013)

[101] J.L. Lado, N. A. García-Martinez, J. Fernández-Rossier, Synthetic Met., http://dx.doi.org/10.1016/j.synthmet.2015.06.026, (2015)

[102] Jun Ding, Zhenhua Qiao, Wanxiang Feng, Yugui Yao, and Qian Niu. Phys. Rev. B **84**, 195444 (2011)

[103] F. Gargiulo, G. Autes, N. Virk, S. Barthel, M. Rosner, L. R. M. Toller, T. O. Wehling, and O. V. Yazyev Phys. Rev. Lett. **113**, 246601 (2014)

[104] Y. Shimazaki, M. Yamamoto, I. V. Borzenets, K.Watanabe, T. Taniguchi, S.Tarucha, ArXiv e-prints (2015), 1501.04776

[105] D.Soriano, D. Van Tuan, S. M-M. Dubois, M. Gmitra, A.W. Cummings, D. Kochan, F. Ortmann, J.C. Charlier, J. Fabian, S. Roche. 2D Materials 2 (2), 022002 (2015)

[106] J. L. Lado and J. Fernández-Rossier, Phys. Rev. Lett. **113**, 027203 (2014)

[107] Stephan Rachel and Karyn Le Hur, Phys. Rev. B **82**, 075106 (2010)

[108] M. Hohenadler, T. C. Lang, and F. F. Assaad, Phys. Rev. Lett. **106**, 100403 (2011)

[109] Manuel Laubach, Johannes Reuther, Ronny Thomale, and Stephan Rachel, Phys. Rev. B **90**, 165136 (2014)

[110] P.W. Anderson. Phys. Rev. **124**, 41 (1961)

[111] R.R Nair, I-L Tsai, M. Sepioni, O. Lehtinen, J. Keinonen, A.V Krasheninnikov, A.H Castro Neto, M.I Katsnelson, A.K Geim and I.V Grigorieva. Nat. Commun. **4**, 2010 (2013)

[112] E.H. Lieb, Phys. Rev. Lett. **62**, 1201 (1989)

[113] Raffaele Resta. J. Phys.: Condens. Matter **12** R107 (2000).

[114] A. H. C. Neto, F. Guinea, N. M. R. Peres, K. S. Novoselov, and A. K. Geim, Rev. Mod. Phys. **81**, 109 (2009).

[115] S. Das Sarma, S. Adam, E. H. Hwang, and E. Rossi, Rev. Mod. Phys. **83**, 407 (2011).

[116] B. Amorim, A. Cortijo, F. de Juan, A. Grushin, F. Guinea, A.Gutiérrez-Rubio, H.Ochoa, V.Parente, R.Roldan, P. San-José, J. Schiefele, M. Sturla, and M. Vozmediano, Physics Reports **617**, 1 (2016), Novel effects of strains in graphene and other two dimensional materials.

[117] K. Bolotin, K. Sikes, Z. Jiang, M. Klima, G. Fudenberg, J. Hone, P. Kim, and H. Stormer, Solid State Commun. **146**, 351 (2008).

[118] C. Beenakker, Rev. Mod. Phys. **80**, 1337 (2008). 22

[119] R. V. Gorbachev, J. C. W. Song, G. L. Yu, A. V. Kretinin, F. Withers, Y. Cao, A. Mishchenko, I. V. Grigorieva, K. S. Novoselov, L. S. Levitov, and A. K. Geim, Science **346**, 448 (2014).

[120] I. Martin, Y. M. Blanter, and A. F. Morpurgo, Phys. Rev. Lett. **100**, 036804 (2008). 25

[121] J.-H. Chen, W. G. Cullen, C. Jang, M. S. Fuhrer, and E. D. Williams, Phys. Rev. Lett. **102**, 236805 (2009).

[122] A. Cresti and S. Roche, Phys. Rev. B **79**, 233404 (2009).

[123] F. Libisch, S. Rotter, and J. Burgdorfer, New J. Phys. **14**, 123006 (2012).

[124] J. A. Lawlor, S. R. Power, and M. S. Ferreira, Phys. Rev. B **88**, 205416 (2013).

[125] L. Zhao, R. He, K. T. Rim, T. Schiros, K. S. Kim, H. Zhou, C. Gutierrez, S. P. Chockalingam, C. J. Arguello, L. Palova, D. Nordlund, M. S. Hybertsen, D. R. Reichman, T. F. Heinz, P. Kim, A. Pinczuk, G. W. Flynn, and A. N. Pasupathy, Science **333**, 999 (2011)

[126] I. A. Pasti, A. Jovanovic, A. S. Dobrota, S. V. Mentus, B. Johansson, and N. V. Skorodumova, (2017), **30** 1710.10084.

[127] A. Pachoud, A. Ferreira, B. Ozyilmaz, and A. H. Castro Neto, Phys. Rev. B **90**, 035444 (2014).

[128] R. R. Nair, W. Ren, R. Jalil, I. Riaz, V. G. Kravets, L. Britnell, P. Blake, F. Schedin, A. S. Mayorov, S. Yuan, et al., Small **6**, 2877 (2010).

[129] A. F. Morpurgo and F. Guinea, Phys. Rev. Lett. **97**, 196804 (2006).

[130] V. V. Cheianov, O. Syljuasen, B. L. Altshuler, and V. Falko, Phys. Rev. B **80**, 233409 (2009). 38

[131] R. Balog, B. Jorgensen, L. Nilsson, M. Andersen, E. Rienks, M. Bianchi, M. Fanetti, E. Laegsgaard, A. Baraldi, S. Lizzit, Z. Sljivancanin, F. Besenbacher, B. Hammer, T. G. Pedersen, P. Hofmann, and L. Hornekaer, Nat Mater **9**, 315 (2010).

[132] V. V. Cheianov, O. Syljuasen, B. L. Altshuler, and V. I. Falko, EPL (Europhysics Letters) **89**, 56003 (2010).

[133] Y. Wang, S. Xiao, X. Cai, W. Bao, J. Reutt-Robey, and M. S. Fuhrer, Sci. Rep. **5**, 15764 EP (2015).

[134] J. R. Wallbank, M. Mucha-Kruczynski, and V. I. Falko, Phys. Rev. B **88**, 155415 (2013).

[135] J. Jung, A. M. DaSilva, A. H. MacDonald, and S. Adam, Nat. Commun. **6**, 6308 (2015).

[136] S. Y. Zhou, G. H. Gweon, A. V. Fedorov, P. N. First, W. A. de Heer, D. H. Lee, F. Guinea, A. H. Castro Neto, and A. Lanzara, Nat Mater **6**, 770 (2007).

[137] T. Iadecola, D. Campbell, C. Chamon, C.-Y. Hou, R. Jackiw, S.-Y. Pi, and S. V. Kusminskiy, Phys. Rev. Lett. **110**, 176603 (2013).

[138] R. Lv, Q. Li, A. R. Botello-Méndez, T. Hayashi, B. Wang, A. Berkdemir, Q. Hao, A. L. Elias, R. Cruz-Silva, H. R. Gutiérrez, Y. A. Kim, H. Muramatsu, J. Zhu, M. Endo, H. Terrones, J.-C. Charlier, M. Pan, and M. Terrones, Sci. Rep. **2**, 586 EP (2012).

[139] C. Gutiérrez, C.-J. Kim, L. Brown, T. Schiros, D. Nordlund, E. B. Lochocki, K. M. Shen, J. Park, and A. N. Pasupathy, Nat Phys **12**, 950 (2016).

[140] A. V. Shytov, D. A. Abanin, and L. S. Levitov, Phys. Rev. Lett. **103**, 016806 (2009).

[141] V. Cheianov, V. Falko, O. Syljuasen, and B. Altshuler, Solid State Commun. **149**, 1499 (2009).

[142] S. LeBohec, J. Talbot, and E. G. Mishchenko, Phys. Rev. B **89**, 045433 (2014).

[143] V. V. Cheianov and V. I. Falko, Phys. Rev. Lett. **97**, 226801 (2006).

[144] D. Solenov, C. Junkermeier, T. L. Reinecke, and K. A. Velizhanin, Phys. Rev. Lett. **111**, 115502 (2013).

[145] P. Hyldgaard and M. Persson, Journal of Physics: Condensed Matter **12**, L13 (2000).

[146] I. Dzyaloshinsky, J. Phys. Chem. Solids 4, 241 (1958). T. Moriya, Phys. Rev. **120**, 91 (1960).

[147] N. Nagaosa and Y. Tokura, Nat Nano **8**, 899 (2013).

[148] A. M. Black-Schaffer, Phys. Rev. B **81**, 205416 (2010).

[149] M. Sherafati and S. Satpathy, Phys. Rev. B **83**, 165425 (2011).

[150] E. Kogan, Phys. Rev. B **84**, 115119 (2011)

[151] D.Soriano, D. Van Tuan, S. M-M. Dubois, M. Gmitra, A.W. Cummings, D. Kochan, F. Ortmann, J.C. Charlier, J. Fabian, S. Roche. 2D Materials 2 (2), 022002 (2015)

[152] A. Bacsi and A. Virosztek. Phys. Rev. B **82**, 193405 (2010)

[153] S. Sorella, E. Tosatti. Europhys. Lett. **19**, 8, 699-704 (1992)

[154] T. Paiva, R.T. Scalettar, W. Zheng, R.R.P. Singh and J.Oitmaa. Phys. Rev. B **72**, 085123 (2005)

[155] L. M. Martelo, M. Dzierzawa, L. Siffert, D. Baeriswyl. Z. Phys. B **103**, 335338 (1997)

[156] Z. Y. Meng , T. C. Lang, S. Wessel, F. F. Assaad and A. Muramatsu. Nature **464**, 847851 (2010)

[157] J. M. B. Lopes dos Santos, N. M. R. Peres, and A. H. Castro Neto, Phys. Rev. Lett. **99**, 256802 (2007).

[158] E. Suárez Morell, J. D. Correa, P. Vargas, M. Pacheco, and Z. Barticevic, Phys. Rev. B **82**, 121407 (2010).

[159] J. M. B. Lopes dos Santos, N. M. R. Peres, and A. H. Castro Neto, Phys. Rev. B **86**, 155449 (2012).

[160] G. Trambly de Laissardiere, D. Mayou, and L. Magaud, Nano Lett. **10**, 804 (2010)

[161] G. Trambly de Laissardiere, D. Mayou, and L. Magaud, Phys. Rev. B **86**, 125413 (2012).

[162] R. Bistritzer and A. H. MacDonald, Proc. Natl. Acad. Sci. U.S.A. **108**, 12233 (2011).

[163] C. Jayaprakash, H.R. Krishnamurthy, S. Sarker and W. Wenzel. Europhys. Lett. **15**, 625 (1991)

[164] H.R. Krishnamurthy, C. Jayaprakash, S. Sarker and W. Wenzel. Phys. Rev. Lett. **64**, 8 (1990)

[165] B. Bernu, C. Lhuillier, and L. Pierre, Phys. Rev. Lett. **69**, 2590 (1992).

[166] L. Capriotti, A. E. Trumper, and S. Sorella Phys. Rev. Lett. **82**, 3899 (1999).

[167] N. D. Mermin and H. Wagner, Phys. Rev. Lett. **17**, 1133 (1966).

[168] D. R. Nelson and J. M. Kosterlitz, Phys. Rev. Lett. **39**, 1201 (1977).

[169] M. Fu, T. Imai, T.-H. Han, and Y. S. Lee, Science **350**, 655 (2015).

[170] S.-H. Lee, H. Kikuchi, Y. Qiu, B. Lake, Q. Huang, K. Habicht, and K. Kiefer, Nat. Mater. **6**, 853 (2007).

[171] L. Seabra, T. Momoi, P. Sindzingre, and N. Shannon, Phys. Rev. B **84**, 214418 (2011).

[172] W.-J. Hu, S.-S. Gong, W. Zhu, and D. N. Sheng, Phys. Rev. B **92**, 140403 (2015).

[173] Z. Zhu and S. R. White, Phys. Rev. B **92**, 041105 (2015).

[174] L. Savary and L. Balents, Rep. Prog. Phys. **80**, 016502 (2017).

[175] Y. Xu, J. Zhang, Y. S. Li, Y. J. Yu, X. C. Hong, Q. M. Zhang, and S. Y. Li, Phys. Rev. Lett. **117**, 267202 (2016).

[176] T.-H. Han, J. S. Helton, S. Chu, D. G. Nocera, J. A. Rodriguez-Rivera, C. Broholm, and Y.S. Lee, Nature (London) **492**, 406 (2012).

[177] T. Grover, Y. Zhang, and A. Vishwanath, New J. Phys. **15**, 025002 (2013).

[178] M. Pretko and T. Senthil, Phys. Rev. B **94**, 125112 (2016).

[179] N. Y. Yao, C. R. Laumann, A. V. Gorshkov, H. Weimer, L. Jiang, J. I. Cirac, P. Zoller, and M. D. Lukin, Nat. Commun. **4**, 1585 (2013).

[180] P. W. Anderson, Mater. Res. Bull. **8**, 153 (1973).

[181] X. Wang, K. Du, Y. Y. F. Liu, P. Hu, J. Zhang, Q. Zhang, M. H. S. Owen, X. Lu, C. K. Gan, P. Sengupta, C. Kloc, and Q. Xiong, 2D Mater. **3**, 031009 (2016).

[182] K. S. Novoselov, A. Mishchenko, A. Carvalho, and A. H. Castro Neto, Science **353**, aac9439 (2016).

[183] A. Castellanos-Gómez, Nat. Photonics **10**, 202 (2016).

[184] J. Quereda, P. San-Jose, V. Parente, L. Vaquero-Garzon, A. J. Molina-Mendoza, N. Agrat, G. Rubio-Bollinger, F. Guinea, R. Roldán, and A. Castellanos-Gómez, Nano Lett. **16**, 2931 (2016).

[185] B. Huang, G. Clark, E. Navarro-Moratalla, D. R. Klein, R. Cheng, K. L. Seyler, D. Zhong, E. Schmidgall, M. A. McGuire, D. H. Cobden, W. Yao, D. Xiao, P. Jarillo-Herrero, and X. Xu, Nature (London) **546**, 270 (2017).

[186] C. Gong, L. Li, Z. Li, H. Ji, A. Stern, Y. Xia, T. Cao, W. Bao, C. Wang, Y. Wang, Z. Q. Qiu, R. J. Cava, S. G. Louie, J. Xia, and X. Zhang, Nature (London) **546**, 265 (2017).

[187] J. S. Alden, A. W. Tsen, P. Y. Huang, R. Hovden, L. Brown, J. Park, D. A. Muller, and P. L. McEuen, Proc. Natl. Acad. Sci. U.S.A. **110**, 11256 (2013).

[188] G. Li, A. Luican, J. M. B. Lopes dos Santos, A. H. Castro Neto, A. Reina, J. Kong, and E. Y. Andrei, Nat. Phys. **6**, 109 (2010).

[189] A. Rozhkov, A. Sboychakov, A. Rakhmanov, and F. Nori, Phys. Rep. **648**, 1 (2016)

[190] A. Luican, G. Li, A. Reina, J. Kong, R. R. Nair, K. S. Novoselov, A. K. Geim, and E. Y. Andrei, Phys. Rev. Lett. **106**, 126802 (2011).

[191] P. San-José, J. González, and F. Guinea, Phys. Rev. Lett. **108**, 216802 (2012).

[192] A. O. Sboychakov, A. L. Rakhmanov, A. V. Rozhkov, and F.Nori, Phys. Rev. B **92**, 075402 (2015).

[193] K. F. Mak, C. H. Lui, J. Shan, and T. F. Heinz, Phys. Rev. Lett. **102**, 256405 (2009).

[194] Y. Zhang, T.-T. Tang, C. Girit, Z. Hao, M. C. Martin, A. Zettl, M. F. Crommie, Y. R. Shen, and F. Wang, Nature (London) **459**, 820 (2009).

[195] P. San-José and E. Prada, Phys. Rev. B **88**, 121408 (2013).

[196] P. Moon and M. Koshino, Phys. Rev. B **87** , 205404 (2013).

[197] P. Moon and M. Koshino, Phys. Rev. B **90**, 155406 (2014).

[198] R. Shankar, Rev. Mod. Phys. **66**, 129 (1994).

[199] I. F. Herbut, Phys. Rev. Lett. **97**, 146401 (2006).

[200] S. Sorella, Y. Otsuka, and S. Yunoki, Sci. Rep. **2**, 992 (2012).

[201] F. F. Assaad and I. F. Herbut, Phys. Rev. X **3**, 031010 (2013).

[202] N. A. García-Martínez, A. G. Grushin, T. Neupert, B. Valenzuela, and E.V. Castro, Phys. Rev. B **88**, 245123 (2013).

[203] G. Z. Magda, X. Jin, I. Hagymasi, P. Vancso, Z. Osvath, P. Nemes-Incze, C. Hwang, L. P. Biro, and L. Tapaszto, Nature (London) **514**, 608 (2014).

[204] J. J. Palacios, J. Fernández-Rossier, and L. Brey, Phys. Rev. B **77**, 195428 (2008).

[205] A. F. Young, C. R. Dean, L. Wang, H. Ren, P. Cadden- Zimansky, K. Watanabe, T. Taniguchi, J. Hone, K. L. Shepard, and P. Kim, Nat. Phys. **8**, 550 (2012).

[206] W. Bao, L. Jing, J. Velasco, Jr, Y. Lee, G. Liu, D. Tran, B. Standley, M. Aykol, S. Cronin, D. Smirnov et al., Nat. Phys. **7**, 948 (2011).

[207] Y. Lee, D. Tran, K. Myhro, J. Velasco, N. Gillgren, C. N. Lau, Y. Barlas, J. M. Poumirol, D. Smirnov, and F. Guinea, Nat. Commun. **5**, 5656 (2014).

[208] J. Velasco, L. Jing, W. Bao, Y. Lee, P. Kratz, V. Aji, M. Bockrath, C. N. Lau, C. Varma, R. Stillwell, D. Smirnov, F. Zhang, J. Jung, and A. H. MacDonald, Nat. Nanotechnol. **7**, 156 (2012).

[209] M. Kharitonov, Phys. Rev. B **86**, 195435 (2012).

[210] E. V. Castro, N. M. R. Peres, T. Stauber, and N. A. P. Silva, Phys. Rev. Lett. **100**, 186803 (2008).

[211] R. Nandkishore and L. Levitov, Phys. Rev. Lett. **104**, 156803 (2010).

[212] O. Vafek and K. Yang, Phys. Rev. B **81**, 041401 (2010).

[213] A. S. Mayorov, D. C. Elias, M. Mucha-Kruczynski, R. V. Gorbachev, T. Tudorovskiy, A. Zhukov, S.V. Morozov, M. I. Katsnelson, V. I. Falko, A. K. Geim, and K. S. Novoselov, Science **333**, 860 (2011).

[214] Y. Lemonik, I. Aleiner, and V. I. Falko, Phys. Rev. B **85**, 245451 (2012).

[215] R. E. Throckmorton and S. Das Sarma, Phys. Rev. B **90**, 205407 (2014).

[216] A. L. Rakhmanov, A. V. Rozhkov, A. O. Sboychakov, and F. Nori, Phys. Rev. Lett. **109**, 206801 (2012).

[217] M. Schuler, M. Rosner, T. O. Wehling, A. I. Lichtenstein, and M.I. Katsnelson, Phys. Rev. Lett. **111**, 036601 (2013).

[218] A. Auerbach, Interacting Electrons and Quantum Magnetism (Springer Science and Business Media, New York, 2012).

[219] P. W. Anderson, Mater. Res. Bull. **8**, 153 (1973).

[220] Z. Meng, T. Lang, S. Wessel, F. Assaad, and A. Muramatsu, Nature (London) **464**, 847 (2010).

[221] Z. A. Kelly, M. J. Gallagher, and T. M. McQueen, Phys. Rev. X **6**, 041007 (2016).

[222] Y. Cao, V. Fatemi, A. Demir, S. Fang, S. L. Tomarken, J. Y. Luo, J. D. Sánchez-Yamagishi, K. Watanabe, T. Taniguchi, E. Kaxiras, R. C. Ashoori, P. Jarillo-Herrero. arXiv:1802.00553 (2018)

[223] H. Bruus and K.. Flensberg, Many-Body Quantum Theory in Condensed Matter Physics (Oxford Graduate Texts, 2016).

[224] D. Tong. Lectures on the Quantum Hall Effect. arXiv:1606.06687